Parallel-line beamsteering for enhanced anomaly detection

By

2016

Amanda Jordan Livers

Submitted to the graduate degree program in Geology and the Graduate Faculty of the University of Kansas in partial fulfillment of the requirements for the degree of Master of Science.

_____

Chairperson Dr. Richard D. Miller

_____

Dr. Ross A. Black

_____

Dr. Jennifer A. Roberts

Date Defended: May 4, 2016

The Thesis Committee for Amanda Jordan Livers

certifies that this is the approved version of the following thesis:

Parallel-line beamsteering for enhanced anomaly detection

_____

Chairperson Dr. Richard D. Miller

Date approved: May 4, 2015

Abstract

Parallel-line beamsteering, a new seismic processing method, was developed to enhance signal from laterally continuous heterogeneities (e.g. tunnel, mine shaft, etc.) and attenuate scatter from localized non-laterally contiguous heterogeneities (e.g. clay lens, boulder, etc.). This method takes advantage of the linear cross line nature of potential targets. Parallel-line beamsteering applies spatial shifting and vertical stacking to parallel-line seismic data in combination with backscatter analysis of surface waves (BASW) and diffraction imaging processing. A processing flow that optimizes the stack and shift process was empirically determined using the standard BASW and diffraction imaging processing flows. This empirically established processing flow was evaluated on parallel-line data acquired at a tunnel test site at the Yuma Proving Grounds in southwestern Arizona. Results show that this method enhances signal from the tunnel by as much 2.8 dB and attenuates other scatter events by as much as 3.9 dB. Beamsteering analysis also reduced the number of possible tunnel locations interpreted from diffraction imaging results using standard interpretation based on spatial matching criteria by up to 66% and from the BASW imaging results by up to 50%. Interpreting results of parallel-line beamsteering requires a less skilled interpretation than conventional tunnel detection methods. This method can also be used to determine the orientation of a tunnel with respect to the two seismic lines. Additionally, this method maintains the small acquisition footprint of current 2D seismic methods required for tunnel detection applications.

Acknowledgements

I would like to thank Richard Miller for financially supporting my Masters degree. I will forever be grateful for the field work and research opportunities he provided me at the Kansas Geological Survey and the geophysics knowledge and skills that I acquired during my time there. I would like to thank the geology department faculty especially Diane Kamola and Ross Black for passionately engaging students in learning and providing hands on experience in the field/lab. Special thanks go to Shelby Peterie for sharing all her knowledge on tunnel detection with me and providing technical and emotional support throughout my research. I would like to thank Julian Ivanov for providing technical support with KGS software. I appreciate the time and effort the Kansas Geological Survey Exploration Division field crew put in to data collection. Lastly, I would like to thank my family and friends for all of their support over the last several years.

Table of Contents

Abstract iii

Acknowledgements iv

Table of Figures vii

1. Introduction 1

2. Joint Tunnel Test Range (JTTR) 4

2.1 Geologic Setting 6

3. Methodology 10

3.1 Diffraction Imaging 10

3.2 Backscatter Analysis of Surface Waves 16

3.3 Parallel-line Beamsteering 19

4. Data Sets 29

4.1 Field Data Acquisition 29

4.1 Field Data Processing Parameters 32

4.3 Synthetic Data Generation 32

5. Parallel-line Beamsteering Method Development 34

5.1 Stacking 34

5.2 Shifting 42

5.2.1 Range Analysis 42

5.2.2 Signal Similarity Analysis 47

5.5 Processing Flow 56

6. Feasibility Test Results and Discussion 58

6.1 Lines 3 and 4 58

6.1.1 Diffraction Imaging 58

6.1.2 Backscatter Analysis of Surface Waves 60

6.2 Lines 5 and 6 63

6.2.1 Diffraction Imaging 63

6.2.2 Backscatter Analysis of Surface Waves 65

6.3 Lines 7 and 8 68

6.3.1 Diffraction Imaging 68

6.3.2 Backscatter Analysis of Surface Waves 69

6.4 Lines 9 and 10 72

6.4.1 Diffraction Imaging 72
6.4.2 Backscatter Analysis of Surface Waves 73
7. Conclusion 77
8. References 79

Table of Figures

FIGURE 1: A) APPROXIMATE LOCATION OF YUMA PROVING GROUNDS (YPG) B) SATELLITE PHOTO OF THE JOINT TUNNEL TEST RANGE (JTTR) WHERE THE RED LINE INDICATES THE APPROXIMATE LATERAL LOCATION OF THE TUNNEL 5
FIGURE 2: PHOTOGRAPH INSIDE A TUNNEL THAT IS SIMILAR TO THE TUNNEL AT YPG SHOWING THE WOOD BRACES, TRACKS, VENTILATION PIPE AND ELECTRICAL LIGHTING (IMAGE FROM SLOAN ET AL. (2012)) 5
FIGURE 3: A) SURFACE VIEW OF THE VERTICAL SHAFT CONNECTED TO THE TUNNEL B) SURFACE VIEW OF VERTICAL SHAFT FROM A DIFFERENT PERSPECTIVE C) VIEW LOOKING DOWN INTO THE VERTICAL SHAFT (PHOTOS FROM THE KANSAS GEOLOGICAL SURVEY) 6
FIGURE 4: GEOLOGIC MAP OF THE SURFACE GEOLOGY OF YUMA PROVING GROUNDS WHERE THE APPROXIMATE LOCATION OF THE JTTR IS INDICATED BY THE RED STAR (IMAGE MODIFIED FROM MCDONALD ET AL. (2009)) 7
FIGURE 5: GEOLOGIC MAP OF THE TRIGO PEAKS AREA WHERE THE APPROXIMATE LOCATION OF THE JTTR IS INDICATED BY THE RED STAR (IMAGE MODIFIED FROM SHERROD AND TOSDAL (1991)) 8
FIGURE 6: CLAY CONTENT FOR BOREHOLE SAMPLES COLLECTED AT JRRT (IMAGE FROM RICKARDS (2011)) 9
FIGURE 7: A) RAYPATHS DEPICTING THE TRAVEL PATH OF A DIFFRACTED WAVE TRAVELING FROM AN ANOMALY IN THE SUBSURFACE TO REVIVERS ON THE SURFACE B) ILLUSTRATION OF THE RESULTING HYPERBOLIC DIFFRACTION-ARRIVAL PATTERN ON A SHOT RECORD (IMAGE AND CAPTION MODIFIED FROM SLOAN ET AL. (2010)) 12
FIGURE 8: WALTERS ET AL. (2007) DIFFRACTION IMAGING PROCESSING FLOW 13
FIGURE 9: SYNTHETIC DATA EXAMPLE (SYNTHETIC DATA PRODUCED USING THE MODEL IN FIGURE 11) SHOWING DIFFRACTION MOVEOUT IN THE COMMON SHOT DOMAIN A) UN-PROCESSED SHOT RECORD CONTAINING A BODY WAVE DIFFRACTION B) SHOT RECORD AFTER A MOVEOUT VELOCITY IS USED TO FLATTEN THE DIFFRACTION ASSUMING THE TUNNEL IS DIRECTLY BELOW RECEIVER STATION 1029 C) APEX ENHANCED SHOT RECORD (IMAGE MODIFIED FROM WALTERS (2009)) 14
FIGURE 10: SYNTHETIC DATA EXAMPLE SHOWING THE FINAL DIFFRACTION IMAGE PRODUCED AFTER DIFFRACTION IMAGING PROCESSING (SYNTHETIC DATA PRODUCED USING THE MODEL IN FIGURE 11) (IMAGE MODIFIED FROM WALTERS (2009)) 15
FIGURE 11: MODEL USED TO CREATE SYNTHETIC DATA IN FIGURE 10, THE SHEAR WAVE VELOCITY USED WAS APPROXIMATELY 300 M/S AND THE COMPRESSIONAL WAVE VELOCITY USED WAS APPROXIMATELY 1000 M/S (IMAGE MODIFIED FROM IMAGE BY JIANGHAI XIA) 15
FIGURE 12: STANDARD BASW PROCESSING FLOW DEVELOPED BY IVANOV ET AL. (2003) 18
FIGURE 13: SYNTHETIC DATA EXAMPLE PRODUCED USING THE MODEL SHIN IN FIGURE 14 SHOWING THE BASW PROCESSING FLOW, WHERE THE RED TRIANGLES INDICATE THE RECEIVER STATION LOCATED DIRECTLY ABOVE THE TUNNEL. THE DIFFERENT PANELS SHOW THE A) ONE OF THE ORIGINAL SHOT GATHERS USED B) THE SHOT GATHER AFTER APPLYING AN F-K FILTERING AND DYNAMIC LINEAR MOVEOUT CORRECTIONS C) THE FINAL BASW IMAGE (IMAGE MODIFIED FROM SLOAN ET AL. (2010)) 18
FIGURE 14: MODEL USED TO PRODUCE SYNTHETIC DATA SHOWN IN FIGURE 13 (IMAGE MODIFIED FROM SLOAN ET AL. (2010)) 19
FIGURE 15: A) SIGNAL RECORDED BY SEISMIC ARRAY STATIONS AT DIFFERENT OFFSET DISTANCES B) SIGNAL AFTER CORRECTING FOR TIME SHIFT (IMAGE MODIFIED FROM OGAH AND CHINEDU (2012)) 20
FIGURE 16: SIGNAL RECORDED BY SEISMIC ARRAY STATIONS DISPLAYED AFTER CORRECTING FOR TIME SHIFT. THE BOTTOM SIGNAL INDICATES THE BEAM PRODUCED AFTER STACKING THE SIGNAL FROM EACH ARRAY STATION. (IMAGE MODIFIED FROM OGAH AND CHINEDU (2012)) 20
FIGURE 17: SURVEY MAP SHOWING RECEIVER LINES, LINE 1 AND 2, COLLECTED PARALLEL TO EACH OTHER AND PERPENDICULAR TO A TUNNEL. BLUE ARROWS DEPICT RAYPATHS FOR A WAVE TRAVELING FROM SHOT LOCATIONS 22

FIGURE 18: SYNTHETIC SEISMIC SHOT RECORDS FOR LINE 1 SHOT 1 AND LINE 2 SHOT 1 GENERATED USING MODEL GEOMETRY SHOWN IN FIGURE 17 22
FIGURE 19: TOP VIEW OF THE MODEL USED TO CREATE SYNTHETIC DATA IN FIGURE 20 FOR RECEIVER LINES COLLECTED OVER A TUNNEL NEAR TWO BURIED OBJECTS, R1 AND R2 (IMAGE CREATED BY CHOON PARK) ... 23
FIGURE 20: A) BASW IMAGE CREATED USING DATA FROM ONE RECEIVER LINE B) BASW IMAGE CREATED AFTER STACKING DATA FROM THREE RECEIVER LINES (MODIFIED FROM IMAGE BY CHOON PARK) 24
FIGURE 21: SURVEY MAP SHOWING PARALLEL LINES, LINE 1 AND 2, COLLECTED PARALLEL TO EACH OTHER AND AT AN OBLIQUE ANGLE TO A TUNNEL. BLUE ARROWS DEPICT RAYPATHS FOR A WAVE TRAVELING FROM SHOT LOCATION 1 ON EACH LINE. THE SHIFT REFERS TO THE DIFFERENCE IN THE DISTANCE FROM SHOT 1 ON LINE 1 TO THE TUNNEL AND THE DISTANCE FROM SHOT 1 ON LINE 2 TO THE TUNNEL. 25
FIGURE 22: 1000 M/S COMPRESSIONAL WAVE VELOCITY MODEL WITH A 1.2 BY 1.2 M AIR FILLED TUNNEL USED TO CREATE SYNTHETIC DATA SHOWN IN FIGURE 23 AND 24 26
FIGURE 23: SYNTHETIC DATA PRODUCED USING A ONE LAYER VP MODEL CONTAINING AN AIR FILLED TUNNEL SHOWN IN FIGURE 22 A) LINE 1 SHOT RECORDS B) LINE 2 SHOT RECORDS 26
FIGURE 24: SURVEY MAP SHOWING HOW AN OFFSET SHIFT IS APPLIED TO PARALLEL LINES, LINE 1 AND 2, COLLECTED PARALLEL TO EACH OTHER AND PERPENDICULAR TO A TUNNEL. BLUE ARROWS DEPICT RAYPATHS FOR A WAVE TRAVELING FROM SHOT LOCATIONS THAT HAVE THE SAME SOURCE-TUNNEL OFFSET ON EACH LINE. 27
FIGURE 25: SYNTHETIC DATA PRODUCED USING A ONE LAYER VP MODEL CONTAINING AN AIR FILLED TUNNEL SHOWN IN FIGURE 20 A) LINE 1 SHOT RECORDS B) LINE 2 SHOT RECORDS SHIFTED BY ONE SHOT LOCATION STATION TO MATCH THE SHOT-TUNNEL OFFSET OF LINE 1 28
FIGURE 26: GEOMETRIC RELATIONSHIP BETWEEN THE SPECIAL SHIFT DISTANCE, THE LINE OFFSET, AND THE ANGLE OF THE TUNNEL WITH RESPECT TO PARALLEL SEISMIC LINES, LINE 1 AND 2 (MODIFIED FROM IMAGE BY SHELBY PETERIE) 29
FIGURE 27: BUNGEE ASSISTED ACCELERATED WEIGHT DROP (PHOTOS FROM THE KANSAS GEOLOGICAL SURVEY) 30
FIGURE 28: A) 24 STATION TOWED LANDSTREAMER B) LANDSTREAMER RECEIVER STATION CONFIGURATION (PHOTOS FROM THE KANSAS GEOLOGICAL SURVEY) 30
FIGURE 29: A) 2011 JTTR SURVEY PERPENDICULAR LINE FIELD LAYOUT B) YPG 2011 OBLIQUE LINE FIELD LAYOUT (IMAGE MODIFIED FROM IMAGE BY SHELBY PETERIE) 31
FIGURE 30: MODEL GEOMETRY OF MODELS USED TO CREATE SYNTHETIC DATA SHOWN IN FIGURE 29 33
FIGURE 31: SYNTHETIC SHOT RECORDS PRODUCED USING A ONE LAYER MODEL (FIGURE 28) 33
FIGURE 32: DIFFRACTION IMAGING PROCESSING FLOWS DEPICTING DIFFERENT PARALLEL-LINE STACKING OPERATIONS A) SHOT GATHERS ARE STACKED BEFORE PRE-PROCESSING B) SHOT GATHERS ARE STACKED AFTER PRE-PROCESSING C) RECEIVER GATHERS ARE STACK AFTER DIFFRACTION MOVEOUT CORRECTION IS PERFORMED IN THE COMMON SHOT DOMAIN AND RESORTING INTO THE COMMON RECEIVER DOMAIN D) FINAL DIFFRACTION IMAGES OR THE COMMON RECEIVER GATHERS ARE STACKED 37
FIGURE 33: DIFFRACTION IMAGE PRODUCED USING DATA COLLECTED ALONG LINE 5 AND 6 USING THE STACKING ROUTINE OUTLINED IN A) FIGURE 30A B) FIGURE 30B C) FIGURE 30C D) FIGURE 30D, BLACK ARROWS INDICATE SIGNAL ASSOCIATED WITH THE TUNNEL AND THE CALCULATED RELATIVE SEISMIC SIGNAL VALUE IS LISTED 38
FIGURE 34: BASW PROCESSING FLOWS DEPICTING DIFFERENT PARALLEL-LINE STACKING OPERATIONS A) SHOT GATHERS ARE STACKED BEFORE *FK*-FILTERING B) SHOT GATHERS ARE STACKED AFTER *FK*-FILTERING C) FINAL BASW IMAGES OR COMMON RECEIVER GATHERS ARE STACK 39
FIGURE 35: FINAL BASW IMAGE AFTER STACKING LINE 3 AND 4 A) UN-FILTERED SHOT RECORDS B) FILTERED SHOT RECORDS C) BASW IMAGES, BLACK ARROW INDICATES THE SIGNAL ASSOCIATED WITH THE TUNNEL AND THE

CALCULATED RELATIVE SEISMIC SIGNAL VALUE IS LISTED, THE DOTTED BLACK LINE INDICATES THE FIRST ARRIVAL TIME OF BACKSCATTERED ENERGY 41
FIGURE 36: DIFFRACTION IMAGES AFTER STACKING PRE-PROCESSED SHOT RECORDS FROM LINE 9 AND 10 AND APPLYING A SPATIAL SHIFT TO LINE 10 OF A) NO SHOT STATIONS (0 M) B) ONE SHOT STATION (2.4 M) C) TWO SHOT STATIONS (4.8 M) D) THREE SHOT STATIONS (7.2 M) E) FOUR SHOT STATIONS (9.6 M), THE LATERAL LOCATION OF THE TUNNEL CORRESPONDS TO RECEIVER STATION 3033 44
FIGURE 37: BASW IMAGES AFTER STACKING LINE 9 AND 10 COMMON RECEIVER GATHERS USING A SPATIAL SHIFT OF A) NO SHOT STATIONS (0 M) B) ONE RECEIVER STATION (1.2 M) C) TWO RECEIVER STATIONS (2.4 M) D) THREE RECEIVER STATIONS (3.6 M) E) FOUR RECEIVER STATIONS (4.8 M) F) FIVE RECEIVER STATIONS (6.0 M) G) SIX RECEIVER STATIONS (7.2 M) 46
FIGURE 38: A) DEPICTION OF CROSSCORRELATION BETWEEN TWO WAVELETS B) DEPICTION OF AUTOCORRELATION (YILMAZ, 2001) 48
FIGURE 39: THEORETICAL EXAMPLE OF CROSSCORRELATION RESULTS FOR SHOT RECORDS FROM TWO SEISMIC LINES. SYNTHETIC SHOT RECORDS WITH DIFFERENT OFFSETS TO THE TUNNEL PRODUCED USING A ONE LAYER SYNTHETIC MODEL. THE CHART ON THE BOTTOM REPRESENTS THE CORRELATION COEFFICIENT CALCULATED BY CORRELATING THE SELECTED SHOT RECORD FROM LINE 2 TO THE SHOT RECORDS FROM LINE 1. SHOT RECORDS WITH THE SAME OFFSET TO THE TUNNEL WILL PRODUCE LARGER CORRELATION COEFFICIENTS. 49
FIGURE 40: CALCULATED DISTANCE VALUES VS. RECORD NUMBER FOR SYNTHETIC SHOT RECORDS (FIGURE 29) ... 51
FIGURE 41: CALCULATED DISTANCE VALUES VS. RECORD NUMBER FOR SYNTHETIC SHOT RECORDS (FIGURE 29) WITH DIFFERENT APPLIED OFFSET SHIFTS 52
FIGURE 42: CALCULATED DISTANCE VALUES VS. RECORD NUMBER FOR LINE 9 AND 10 WITH DIFFERENT APPLIED OFFSET SHIFTS 53
FIGURE 43: DEPICTION OF 2D CORRELATION APPLIED TO TWO MATRICES. THE CENTER OF MATRIX 2 (M2) IS ALIGNED WITH MATRIX 1 (M1) AT DIFFERENT POSITIONS. ALIGNED ELEMENTS ARE CORRELATED AND THEIR COEFFICIENTS ARE SUMMED AND ASSIGNED TO THE ALIGNMENT OF THE CENTER OF M2. (IMAGE RETRIEVED FROM HTTP://WWW.MATHWORKS.COM/HELP/SIGNAL/REF/XCORR2.HTML 54
FIGURE 44: A SMALL SUBSECTION OF SAMPLES THAT COMPRISE THE FINAL DIFFRACTION IMAGE ARE EXTRACTED AS A 2D IMAGE TO USE FOR CORRELATION. 55
FIGURE 45: THE 2D IMAGE IS SHIFTED IN TIME AND SPACE WITH RESPECT TO A SECOND DIFFRACTION IMAGE. ALIGNED SAMPLES ARE CORRELATED AND THE VALUE OF THE SUMMED CORRELATION COEFFICIENTS ARE ASSIGNED TO THE CENTER LOCATION OF THE 2D IMAGE. 55
FIGURE 46: PARALLEL-LINE BEAMSTEERING BASW PROCESSING FLOW 56
FIGURE 47: PARALLEL-LINE BEAMSTEERING DIFFRACTION IMAGING PROCESSING FLOW 57
FIGURE 48: DIFFRACTION IMAGE A) LINE 3 B) LINE 4 C) AFTER STACKING LINE 3 AND 4 PRE-PROCESSED RAW DATA, BLACK ARROW INDICATES SIGNAL ASSOCIATED WITH THE TUNNEL, CIRCLES HIGHLIGHT AMPLITUDE ANOMALIES COMMON TO BOTH LINES 61
FIGURE 49: BASW IMAGE A) LINE 3 B) LINE 4 C) AFTER STACKING LINE 3 AND 4 BASW IMAGES , BLACK ARROW INDICATES THE SIGNAL ASSOCIATED WITH THE TUNNEL AND THE CALCULATED RELATIVE SEISMIC SIGNAL VALUE IS LISTED, THE DOTTED BLACK LINE INDICATES THE FIRST ARRIVAL TIME OF BACKSCATTERED ENERGY 62
FIGURE 50: DIFFRACTION IMAGE A) LINE 5 B) LINE 6 C) STACKING LINE 5 AND 6 PRE-PROCESSED RAW DATA, BLACK ARROW INDICATES SIGNAL ASSOCIATED WITH THE TUNNEL, CIRCLES HIGHLIGHT AMPLITUDE ANOMALIES COMMON TO BOTH LINES 66
FIGURE 51: BASW IMAGE A) LINE 5 B) LINE 6 C) AFTER STACKING LINE 5 AND 6 BASW IMAGES , BLACK ARROW INDICATES THE SIGNAL ASSOCIATED WITH THE TUNNEL AND THE CALCULATED RELATIVE SEISMIC SIGNAL

VALUE IS LISTED, THE DOTTED BLACK LINE INDICATES THE FIRST ARRIVAL TIME OF BACKSCATTERED ENERGY 67
FIGURE 52: DIFFRACTION IMAGE A) LINE 7 B) LINE8 C) AFTER STACKING LINE 7 AND 8 PRE-PROCESSED RAW DATA, BLACK ARROW INDICATES SIGNAL ASSOCIATED WITH THE TUNNEL, CIRCLES HIGHLIGHT AMPLITUDE ANOMALIES COMMON TO BOTH LINES.....70
FIGURE 53: BASW IMAGE A) LINE 7 B) LINE 8 C) AFTER STACKING LINE 7 AND 8 BASW IMAGES , BLACK ARROW INDICATES THE SIGNAL ASSOCIATED WITH THE TUNNEL AND THE CALCULATED RELATIVE SEISMIC SIGNAL VALUE IS LISTED, THE DOTTED BLACK LINE INDICATES THE FIRST ARRIVAL TIME OF BACKSCATTERED ENERGY 71
FIGURE 54: DIFFRACTION IMAGE A) LINE 9 B) LINE 10 C) AFTER SHIFTING LINE 10 BY SIX STATIONS (7.2 M) AND STACKING LINE 9 AND 10 PRE-PROCESSED RAW DATA, BLACK ARROW INDICATES SIGNAL ASSOCIATED WITH THE TUNNEL, CIRCLES HIGHLIGHT AMPLITUDE ANOMALIES COMMON TO BOTH LINES 75
FIGURE 55: BASW IMAGE A) LINE 9 B) LINE 10 C) AFTER SHIFTING LINE 10 BASW IMAGE BY 6.0 M (5 STATIONS) AND STACKING LINE 9 AND 10 BASW IMAGES , BLACK ARROW INDICATES THE SIGNAL ASSOCIATED WITH THE TUNNEL AND THE CALCULATED RELATIVE SEISMIC SIGNAL VALUE IS LISTED, THE DOTTED BLACK LINE INDICATES THE FIRST ARRIVAL TIME OF BACKSCATTERED ENERGY 76

1. Introduction

Clandestine tunnels have been used for centuries for military applications and continue to be a threat in war zones as well as sovereign country borders (Sloan et al., 2011; Sloan et al., 2013a). Clandestine tunnels used to smuggle goods or people across borders are a prevalent issue, along the U.S.-Mexico border where more than 75 tunnels have been discovered since 2007 and tunneling remains ongoing. (Sloan et al., 2012; (ONDCP), 2013; Schwenk et al., 2014). Seismic methods have been shown to poses great potential for tunnel detection because of inherent sensitivity of the methods to dramatic changes in acoustic impedance associated with voids in the subsurface (Miller, 2004). Seismic methods are less susceptible to energy attenuation than other geophysical methods and they have the ability to facilitate acquisition over a large area in a range of geologic environments with minimal ground preparation (Steeples, 2001). Additionally, current development of non-contact sensors for seismic data collection will allow seismic data to be collected as rapidly as other geophysics methods (Haupt and Rolt, 2005; Bjurström et al., 2014). Several studies have been undertaken to evaluate the feasibility of different seismic methods to detect known tunnels under near ideal conditions at sites various sites including Colorado, California, South Africa, Japan, Israel, Afghanistan, and along the US/Mexico border. The seismic methods tested for their applicability to tunnel detection include refraction tomography (Wright et al., 2000), reflection (Inazaki et al., 2005), diffraction (Steeples and Miller, 1988), borehole tomography (Shustak et al., 2015), surface wave attenuation (Sherman et al., 2014), backscatter analysis of surface waves (Schwenk, et al., 2014), and multi-channel analysis of surface waves (Sloan, et al., 2013a). However, very few methods have proven to be successful at detecting previously unknown tunnels.

Success of seismic methods has been variable and appears dependent on factors such as the size and depth of the tunnel, the host rock, and the survey environment (cultural and natural). Seismic

reflection techniques cannot image a tunnel whose diameter is smaller than a fourth of the dominant seismic wavelength, and multi-channel analysis of surface waves cannot image a tunnel whose diameter is smaller than a half of the dominant wavelength (McCann et al., 1987; Zeng et al., 2009). The tunnel diameter-to-depth ratio affects the amplitude of the seismic signal perturbations due to the tunnel (Zeng, et al., 2009). The host rock also affects the ability to properly identify the signal from a void because noise due to complex geology may obscure the signal from the void. Geologic structures may produce signal indistinguishable from that of a void (Moran and Greenfield, 1993; Grandjean and Leparoux, 2004). Additionally, void detection in urban settings or near infrastructure introduces several sources of noise (e.g. signal from traffic and scatters from infrastructure) that limit successful application of seismic methods (Dobecki and Upchurch, 2006). Clandestine tunnel detection using seismic methods is a complex problem to solve because of these factors.

Successful seismic tunnel detection methods need to fulfill a set of specific requirements. Sloan (2015) outlines the requirements of a perfect tunnel detection system, which include:

- the ability to efficiently detect tunnels in tunnel friendly geologic and cultural environments with a low false-positive rate,
- a small acquisition footprint to facilitate data collection in environments with surface constraints, such as like infrastructure,
- rapid acquisition rates of over a kilometer a day to avoid dwelling in hostile environment for extended periods of time,
- near real time data processing to address evolving threats.

Optimal 3D approaches would better delineate subsurface tunnels. However, the large receiver array footprint necessary for 3D seismic surveys are impractical and, in some cases, impossible to implement at many sites due to cultural constraints (Sloan, 2015). 3D methods also require unique expertise and equipment for acquisition and processing, and typically require significantly more computer power and time. These factors can hinder the rapid analysis and security resource deployment necessary when there are immediate security concerns. 2D seismic methods are more likely to fulfill the outlined requirements.

Two 2D seismic methods, diffraction imaging (Walters et al., 2007) and backscatter analysis of surface waves (BASW) (Ivanov et al., 2003), have had some success detecting previously unknown tunnels. Sloan et al. (2013b) used a combined interpretation technique of diffraction imaging and BASW to locate a previously unknown tunnel, which after excavation was identified as an abandoned irrigation tunnel. Despite the success of these methods several authors have noted the restrictions associated with these methods. Low signal-to-noise ratio for signal from the tunnel makes these signals susceptible to being falsely dismissed as noise (Sloan et al., 2010). BASW and diffraction imaging results may also contain coherent events from natural anomalies such as geological heterogeneities, such as clay lens, boulders, etc. (Sloan, et al., 2012; Shustak, et al., 2015). Additionally, these 2D seismic approaches are optimal for a perpendicular tunnel and cannot estimate tunnel azimuth without further analysis of at least two lines of data (Peterie and Miller, 2015).

In order to improve the performance of methods such as diffraction imaging and BASW, a new method to enhance the signal-to-noise ratio of the data, parallel-line beamsteering, was developed. Parallel-line beamsteering was evaluated at a real hand-dug tunnel test site, Joint Tunnel Test Range (JTTR) at Yuma Proving Grounds (YPG) in southwestern Arizona. Field data acquired in 2011 as part of a blind tunnel detection was used to develop the processing flow for parallel-line beamsteering.

This new method uses the unique geometric relationship between a laterally continuous void and two parallel seismic lines. It maintains the relatively small acquisition footprint of 2D methods, but allows interpretation of a 3D volume of the subsurface similar to exploration 3D methods. This method is a refined beamsteering (shift and stack) method (Rost and Thomas, 2002; Tanimoto and Prindle, 2007; Ogah and Chinedu, 2012). A spatial shift is used to stack shot records from parallel seismic lines with maximum correlation of scatter from a tunnel to allow coherent vertical stacking of signal. Shift ranging and signal similarity analysis were explored to determine the appropriate offset shift and then compared for accuracy and efficiency. These approaches were used to condition data in advance of processing with

BASW and diffraction imaging. These methods provide a direct means of calculating not only tunnel depth and spatial location, but also tunnel orientation relative to the survey lines.

Results of this research advanced the science of tunnel detection, making it more automated, moving closer to real-time processing by nontechnical personnel (Sloan et al., 2015). This thesis demonstrates how with appropriate line-to-line correlation results, stacking parallel-line data, in conjuncture with established tunnel detection methods can increase signal-to-noise by as much as 3 dB. The accuracy and confidence in delineating crossline anomalies like tunnels are thus improved. Parallel-line beamsteering is applicable for tunnel detection and reduces/minimizes the level of skilled interpretation needed to detect a tunnel using diffraction imaging and BASW. Future development of a 2D crosscorrelation algorithm will further automate this process.

2. Joint Tunnel Test Range (JTTR)

The Joint Tunnel Test Range (JTTR) was created through a joint effort of the US Department of Defense and Homeland Security to simulate a real clandestine tunnel in a setting well suited for research, development and testing of a wide range of detection methods ((ONDCP), 2009). The JTTR is located at Yuma Proving Grounds (YPG) in southwest Arizona (Figure 1A). A 90 m long tunnel was hand-dug on this site 9.1 m below the surface to simulate as close as possible a clandestine tunnel like many in current conflict areas (Figure 1B). The tunnel is 1.2 m wide and 1.5 m tall and uses wood shoring similar to a number of previously discovered clandestine tunnels. The tunnel at YPG contains other items that are common to clandestine tunnels such as a rail track, a ventilation pipe, and electrical lighting (Figure 2). The tunnel at YPG is connected to the surface by a vertical shaft (Figure 3).

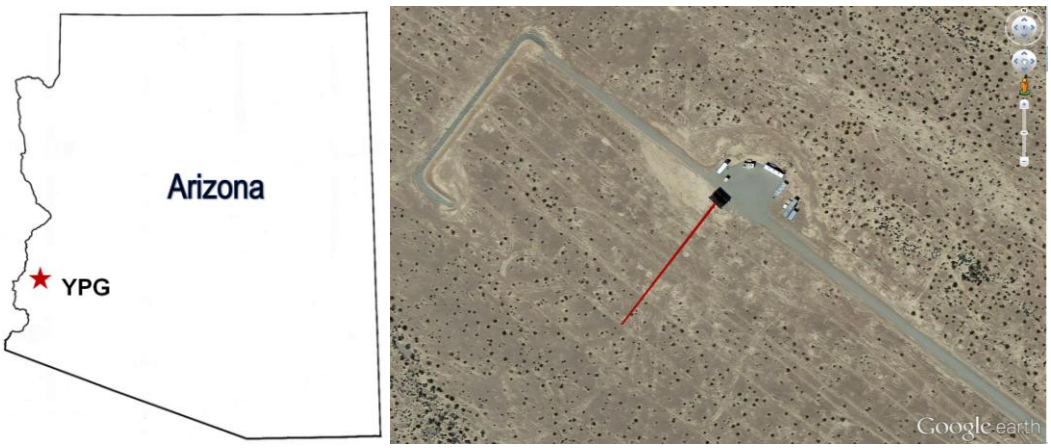

Figure 1: A) approximate location of Yuma Proving Grounds (YPG) **B)** satellite photo of the Joint Tunnel Test Range (JTTR) where the red line indicates the approximate lateral location of the tunnel

Figure 2: Photograph inside a tunnel that is similar to the tunnel at YPG showing the wood braces, tracks, ventilation pipe and electrical lighting (Image from Sloan et al. (2012))

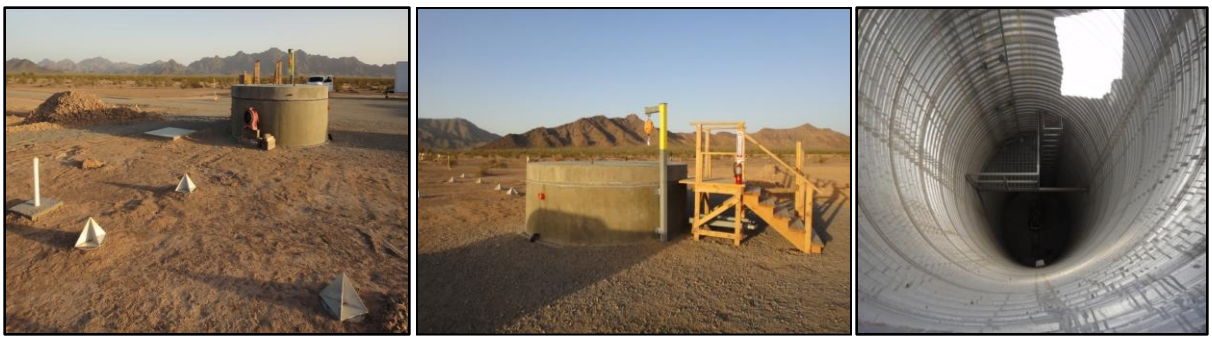

(A) **(B)** **(C)**

Figure 3: A) surface view of the vertical shaft connected to the tunnel **B)** surface view of vertical shaft from a different perspective **C)** view looking down into the vertical shaft (Photos from the Kansas Geological Survey)

2.1 Geologic Setting

YPG lies within the Basin and Range Province and is regionally characterized by large north-south trending normal faulting associated with Cenozoic extension (Zoback et al., 1981; Wernicke, 1992). Movement of fault blocks in response to this extension formed numerous mountain ranges and range bound basins (Stewart, 1980). The JTTR lies on an alluvial plain east of South Trigo Peaks near the transition zone between a modern alluvial fan and the alluvial plain (Figure 4) (Sherrod and Tosdal, 1991). The site is surrounded by several ranges including the Dome Rock Mountains to the north, North and South Trigo Peak to the west, and South Trigo Peak to the south (Figure 5) (Schwenk, 2013). The Trigo Peaks consist of Jurassic granitic rocks unconformably overlain by arkosic sandstone and Miocene volcanic rocks (Tosdal and Sherrod, 1985; Sherrod and Tosdal, 1991). The Dome Rock Mountains consists of Proterozoic gneiss unconformably overlain by Paleozoic and lower Mesozoic cratonal metasedimentary rocks (Boettcher and Mosher, 1998; Boettcher et al., 2002). These metasedimentary rocks are overlain by the Jurassic and Cretaceous McCoy Mountain Formation in the southern portion of the Dome Rock Mountains (Boettcher, et al., 2002).

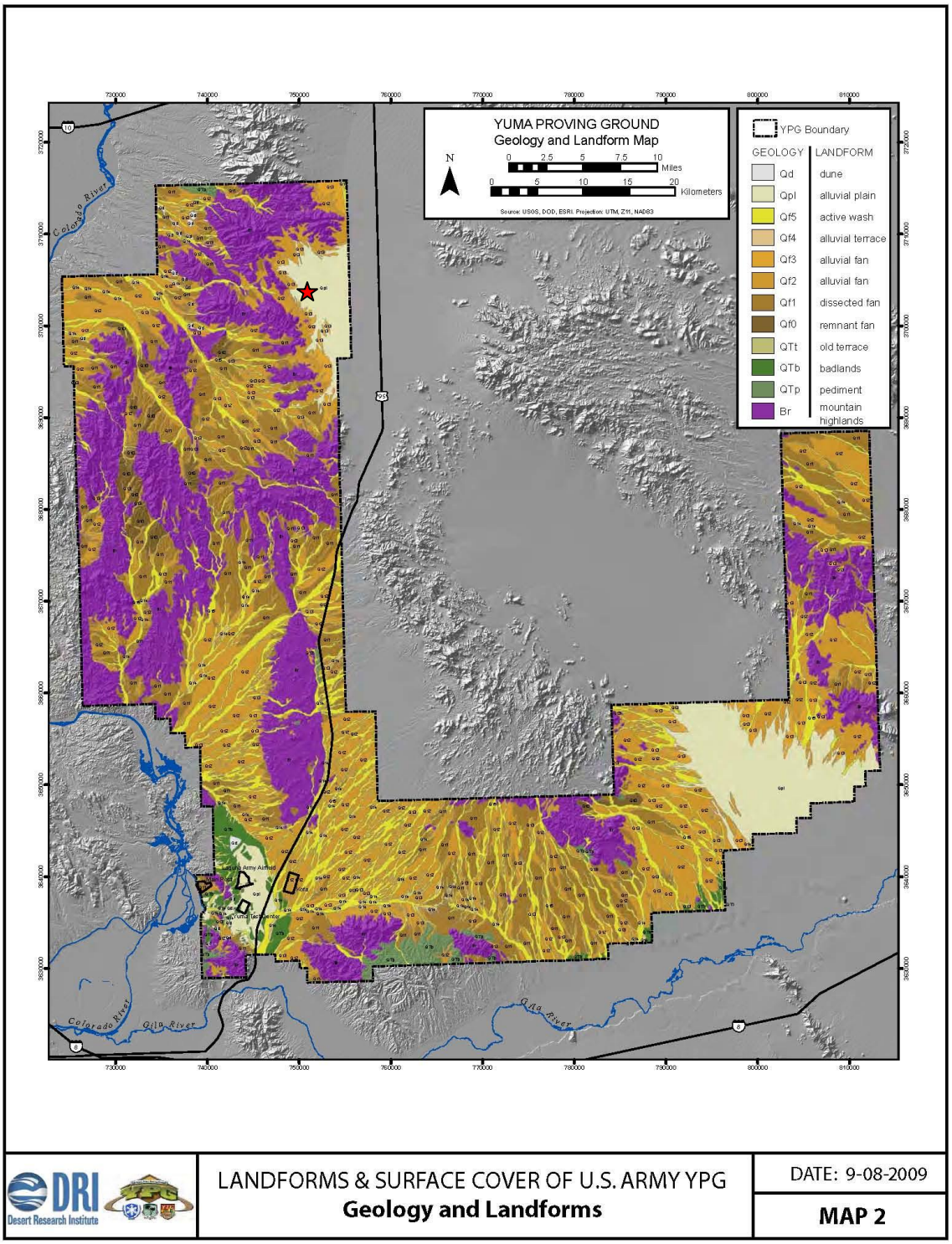

Figure 4: geologic map of the surface geology of Yuma Proving Grounds where the approximate location of the JTTR is indicated by the red star (Image modified from McDonald et al. (2009))

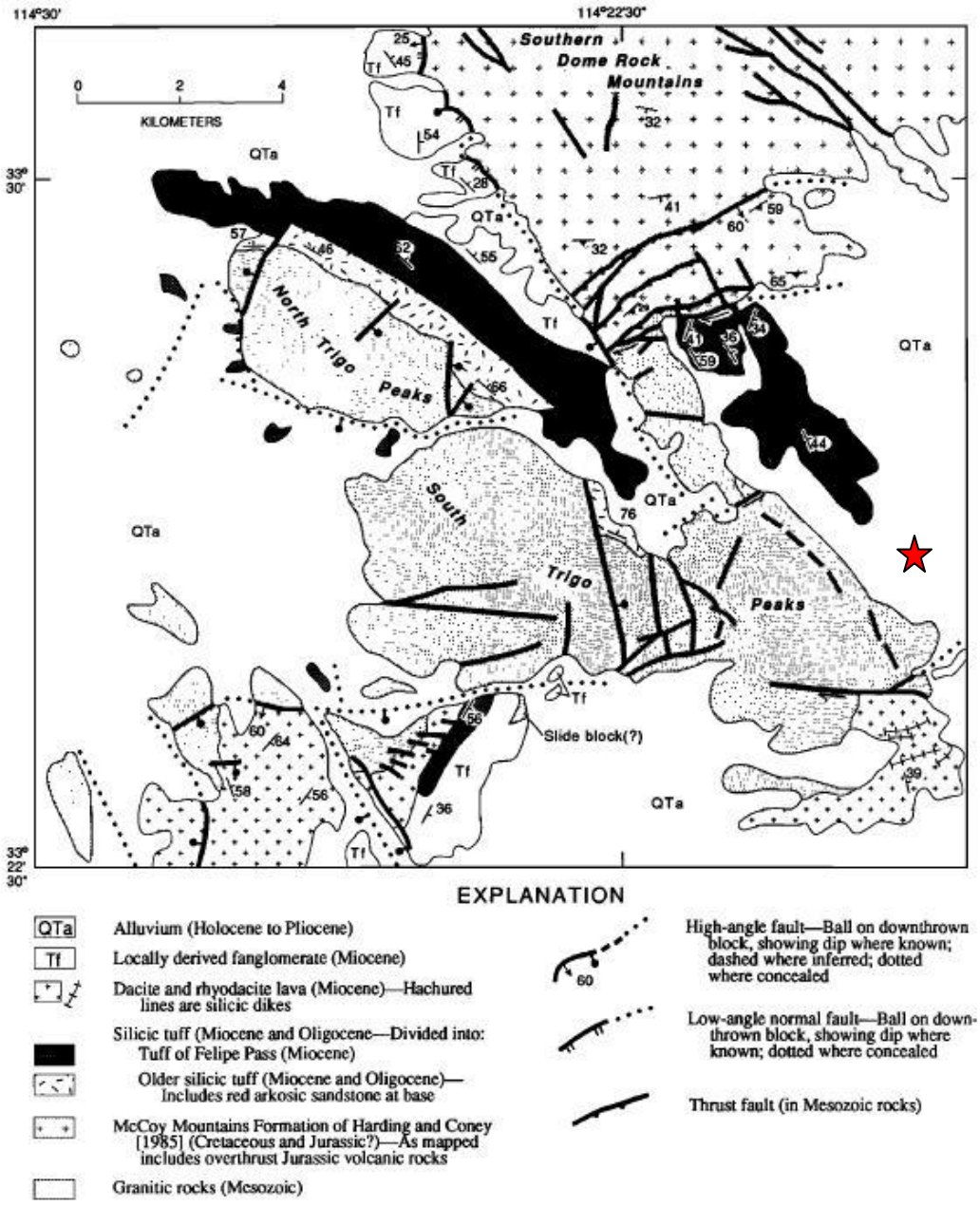

Figure 5: geologic map of the Trigo Peaks area where the approximate location of the JTTR is indicated by the red star (Image modified from Sherrod and Tosdal (1991))

The site consists of semi-consolidated sediments likely sourced by the surrounding ranges. Miller et al. (2010) collected and analyzed sonic-boring samples from six boreholes during a site characterization study at the JTTR. Samples collected were wackes to mudstones with poorly sorted subrounded to subangular clasts and variable clay content with depth and (Figure 6) (Sherrod and Tosdal, 1991). Preliminary field notes identify the clasts as quartz, potassium feldspar, sodium feldspar, chlorite, biotite, white evaporate crystals and unknown white, brown and grey minerals (Miller et al., 2010). Clasts were mostly granule size (2 - 4 mm), but ranged from fine (0.125 – 0.250 mm) to pebble size (4 - 64 mm) (Ivanov et al., 2005).

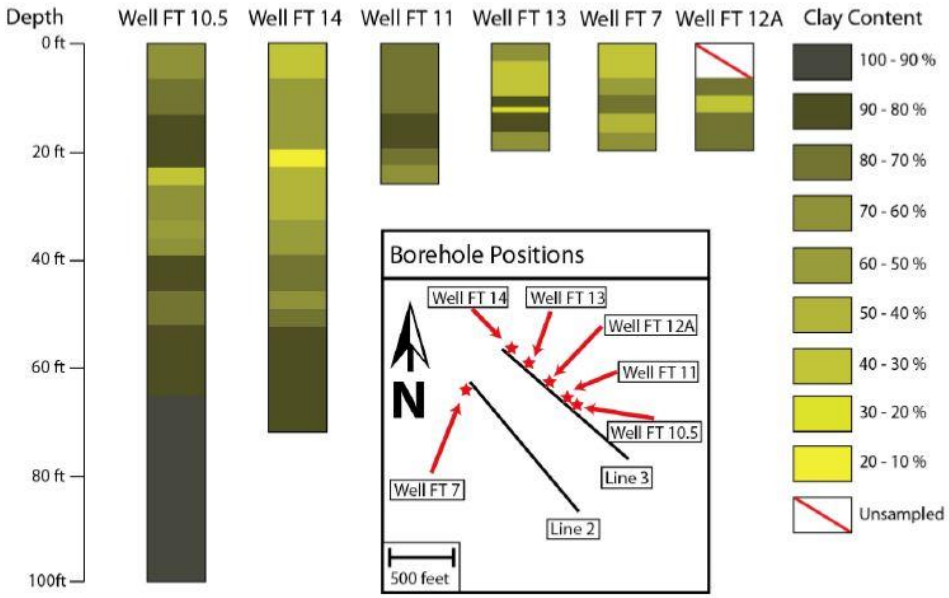

Figure 6: clay content for borehole samples collected at JRRT (Image from Rickards (2011))

3. Methodology

Parallel-line beamsteering is a signal enhancement method designed to be used to pre-condition data by laterally shifting and coherently stacking the data before use they are input into the tunnel detection algorithms. In this research, the tunnel detection methods utilized were diffraction imaging and BASW. This chapter discusses the theory behind diffraction imaging, BASW, and parallel-line beamsteering and outlines the previously established processing steps used for diffraction imaging and BASW.

3.1 Diffraction Imaging

Diffractions are the seismic response to small subsurface heterogeneities whose diameter is less than the Fresnel diameter associated with the dominant wavelength (Moser and Howard, 2008; Keydar et al., 2012). When a wavefront encounters such a heterogeneity it acts as a point source according to Huygens' principle, which states that every point on a wavefront can act as a source to a secondary wavefront (Knight, 2013). Energy is redistributed and radiates from the heterogeneity, returning to receivers at the surface (Figure 7A) (Sheriff, 2002). The resulting shot record will contain diffracted body wave energy with a hyperbolic arrival pattern as a function of offset (Figure 7B). The wavefield arrival geometry of the diffraction can be described by the following two-way traveltime (Walters, et al., 2007):

$$t_d = \left({}^{1}/_{V}\right)\left((x_s^2 + z^2)^{1/2} + (x_r^2 + z^2)^{1/2}\right) \quad (1)$$

where

$t_d =$ arrival time, $V =$ seismic velocity (shear or compressional) of the layer containing the diffractor, $x_s =$ distance between the source and the receiver directly above the tunnel, $x_r =$ distance between the receiver directly above the tunnel and the active receiver, and $z =$ depth of the tunnel.

The peak or the apex of the diffraction corresponds to the direct first arrival time of the diffracted energy and is recorded on the receiver directly above the tunnel for a site without surface elevation change and lateral homogeneity of rock units (Landa and Keydar, 1998). In this case, $x_r = 0$ and Equation 1 can be solved for the depth of the heterogeneity causing the scattering as shown below in Equation 2.

$$z = \frac{t_0^2 V^2 - x_s^2}{2t_0 V} \qquad (2)$$

Where the arrival time (t_d) was replaced with the two-way travel-time (t_0) associated with the apex (Figure 7B). Identifying the apex of the diffraction determines the lateral location of the heterogeneity and Equation 2 can be used to calculate the depth of a subsurface heterogeneity.

Body wave diffractions are low amplitude events compared to high energy surface waves recorded in near-surface surveys (Xia et al., 2007). Zeng et al. (2009) calculated that the amplitude of direct compressional waves is 10% of the amplitude of the direct surface waves. The amplitudes of the compressional wave diffractions from tunnels in their synthetic models were as little as 1% of the direct surface wave amplitudes. Additionally, body wave diffractions from heterogeneities in the near sub-surface have arrival times that coincide with the direct surface wave arrivals. The low amplitude nature of body wave diffractions and the difficulty attenuating the direct surface waves without attenuating the body wave diffractions makes identifying diffractions on shot gathers very difficult. A processing method, such as diffraction imaging, is needed to help enhance diffractions.

Steeples and Miller (1984) recognized the possibility of developing a diffraction imaging technique for tunnel detection after observing body wave diffractions from a tunnel during a seismic reflection survey, but lacked the computational power to do so. Landa et al. (1987) developed one of the first diffraction imaging methods using a phase correlation procedure to enhance the amplitude of the signal associated with the apex of a diffraction (Landa and Keydar, 1998). The diffraction imaging

algorithm used in this research is a modified version of the Landa et al. (1987) diffraction imaging method developed specifically for tunnel detection by Walters et al. (2007).

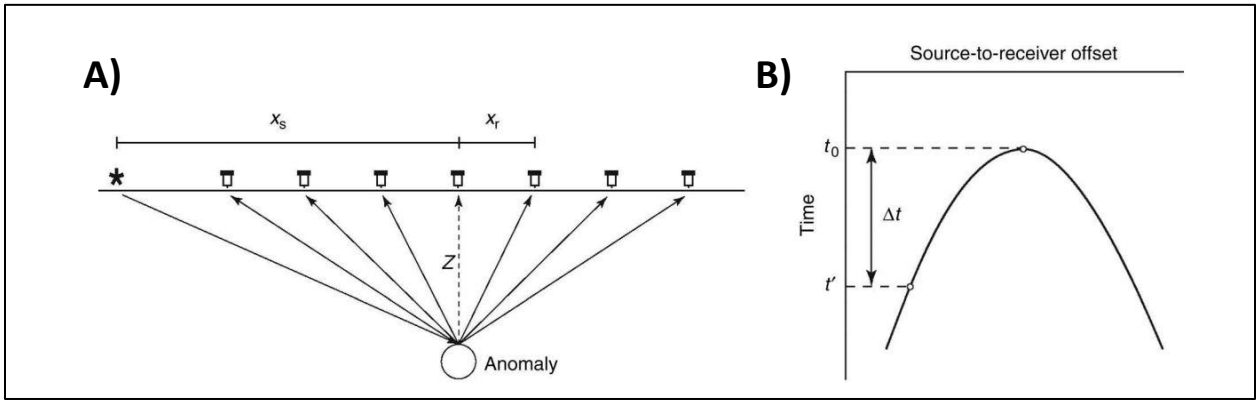

Figure 7: A) Raypaths depicting the travel path of a diffracted wave traveling from an anomaly in the subsurface to revivers on the surface **B)** illustration of the resulting hyperbolic diffraction-arrival pattern on a shot record (Image and caption modified from Sloan et al. (2010))

The Walters et al. (2007) algorithm was designed to enhance the apex of a body wave diffraction. The algorithm assumes a possible diffraction at every point in the subsurface, which is well suited for tunnel searches and detection (Walters et al., 2009). Additionally, no a priori knowledge about the tunnel is necessary for this method to be successful.

The Walters et al. (2007) algorithm consists of five main steps (Figure 8). The first step of diffraction imaging is pre-processing of the seismic data. Pre-processing for this method includes f-k filtering, low cut filtering and application of automatic gain control. Pre-processing is applied to shot gathers to attenuate ground roll and guided wave amplitudes and enhance the signal-to-noise ratio of the body diffractions (Peterie and Miller, 2015). After pre-processing, the second step involves diffraction moveout corrections to flatten the diffraction and enhance the diffraction apex (Figure 8). This process assumes every receiver station is potentially located directly above the tunnel. Assuming the first trace corresponds to the receiver station located directly above the tunnel, a moveout velocity

is used to calculate the correction applied to flatten the hyperbolic shape of arriving diffracted energy with an apex at the receiver station corresponding to the first trace (Figure 9B). After the diffraction is flattened the apex of the diffraction is enhanced by vertically stacking all the traces in the shot record into a single trace. The resulting trace is then assigned to the first trace in the apex enhanced shot gather (Figure 9C). This step is repeated for every trace in the shot record. This focuses diffraction energy to the apex and will coherently stack the signal if the receiver station is located directly above the tunnel (Walters, et al., 2009). This step enhances the apex of the diffraction and attenuates other wavefield components (Figure 9C). The third and fourth steps correct for the source-receiver offset (Figure 8). Apex enhanced shot records are arranged into common receiver gathers and diffraction moveout corrections are applied using the method described previously. In the last step all traces from all shot gathers from a specific receiver location are stacked resulting in a final common receiver stack (Figure 10C).

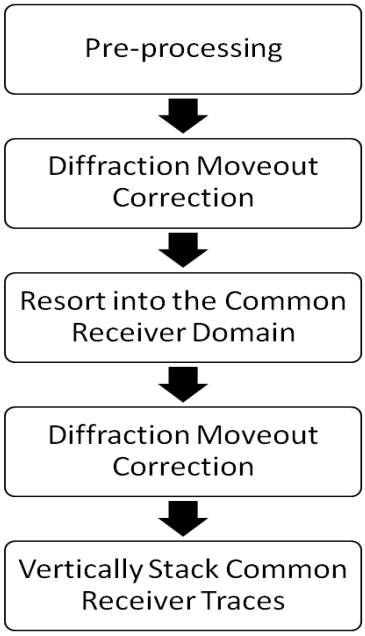

Figure 8: Walters et al. (2007) diffraction imaging processing flow

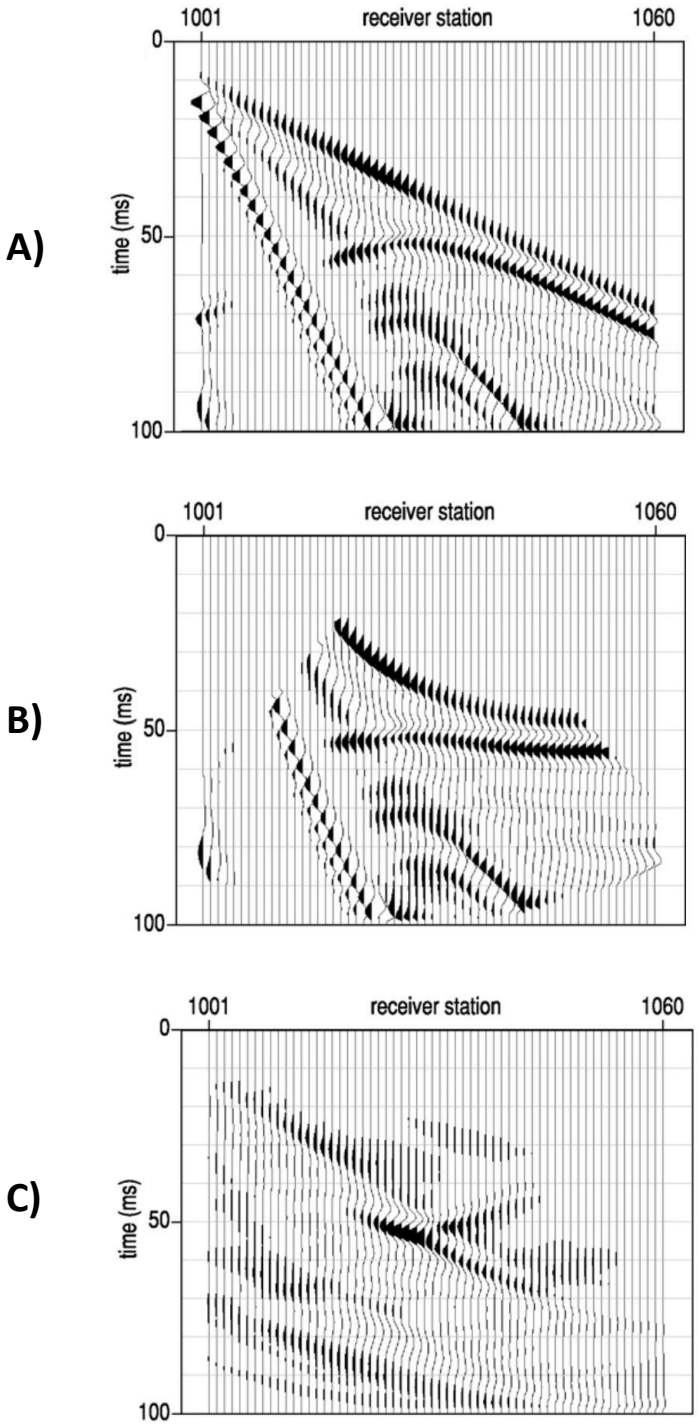

Figure 9: synthetic data example showing diffraction moveout in the common shot domain (synthetic data produced using the model in Figure 11) **A)** un-processed shot record containing a body wave diffraction **B)** shot record after a moveout velocity is used to flatten the diffraction assuming the tunnel is directly below receiver station 1029 **C)** apex enhanced shot record (Image modified from Walters (2009))

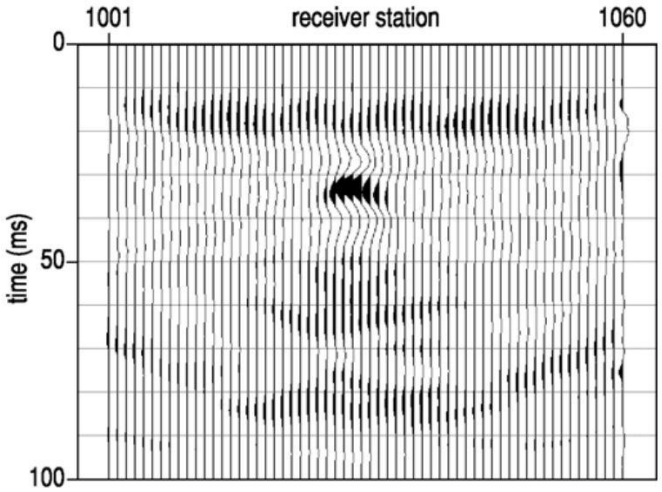

Figure 10: synthetic data example showing the final diffraction image produced after diffraction imaging processing (synthetic data produced using the model in Figure 11) (Image modified from Walters (2009))

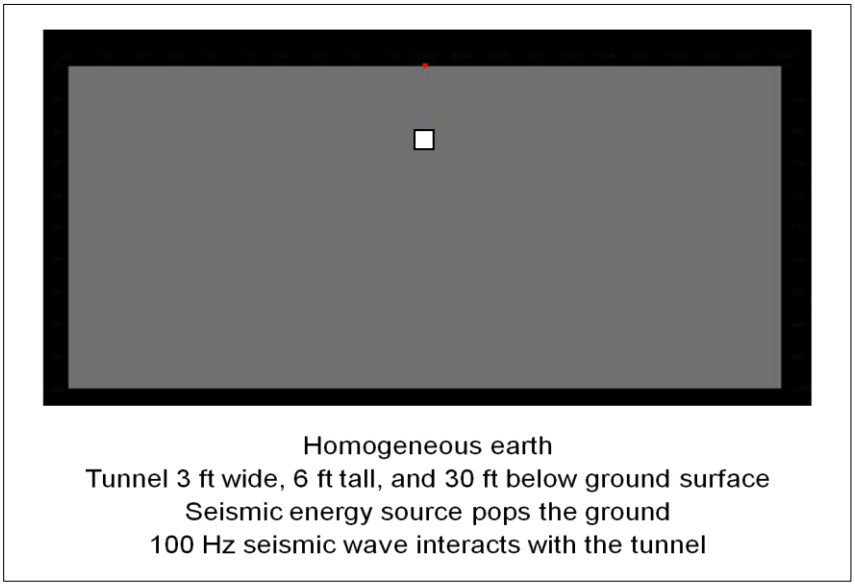

Figure 11: model used to create synthetic data in Figure 10, the shear wave velocity used was approximately 300 m/s and the compressional wave velocity used was approximately 1000 m/s (Image modified from image by Jianghai Xia)

High amplitude bulls-eye events indicate apex locations on the final common-receiver stack (from here referred to as the diffraction image) (Figure 10C). These high amplitude features are diagnostic of the approximate lateral location of sub-surface heterogeneities producing wavefield scattering. The receiver location that corresponds to the center of the amplitude anomaly represents its spatial location. The approximate depth of the tunnel (z) can be calculated from the two way arrival time (t_0) and the velocity (V) used for the diffraction moveout corrections. After processing, $x_s = 0$ and Equation 2 can be simplified and rewritten as:

$$z = \frac{t_0 V}{2} \tag{3}$$

3.2 Backscatter Analysis of Surface Waves

Sub-surface heterogeneities like tunnels cause perturbations in surface wave propagation including phase and amplitude distortion (Gelis et al., 2005). The mechanics of these surface wave perturbations have yet to be fully explained. Some literature suggests surface waves are reflected and diffracted when they encounter sub-surface heterogeneities (Park et al., 1999a; Xia et al., 2006). However, they fail to explain how surface wave energy can be redistributed or scattered while obeying the surface wave mechanic of being bound to a free surface. Korneev (2009) uses synthetic models to show that surface wave perturbations are more complex and may involve resonant emission and oscillations of seismic energy that become trapped in air filled voids.

Although the mechanics of surface wave perturbations due to sub-surface heterogeneities are not fully understood, several authors attempt to use what they interpret as scattered surface wave energy to detect heterogeneities. Herman et al. (1998) first recognized the potential of using 'scattered surface waves' to image small, near-surface heterogeneities. Several authors have gone on to develop

methods to locate near-surface heterogeneities using these scatters (Grandjean and Leparoux, 2004; Riyanti et al., 2005; Yu et al., 2014). These scattered Rayleigh waves have higher amplitudes than body wave diffractions and are less susceptible to attenuation making them a good candidate for void detection as long as the desired penetration depth can be achieved (Xia, et al., 2006).

BASW is a method that enhances the part of a Rayleigh wave energy that propagates backwards towards the source referred to as backscatter. Ivanov et al. (2003) established a standard BASW processing flow to enhance this backscattered energy. The BASW processing flow consists of three main steps, filtering, applying a moveout correction and stacking common receiver gathers (Figure 12).

A broad f-k filter can be applied to vertically stacked data to attenuate high amplitude surface wave direct arrivals and other forward propagating energy (Zeng et al., 2009). Dynamic linear moveout (DLMO) corrections are applied to each shot record to flatten any remaining forward propagating energy. The DLMO corrections shift the backscatter energy so the earliest arriving backscatter energy is at time zero on the shot record (Figure 13B) (Sloan, et al., 2010; Schwenk, et al., 2014). The DLMO is described by the following equation (Park, et al., 1999a):

$$W_{DLMO}(f,x) = e^{j\emptyset_j} W(f,x) \tag{4}$$

where

$W_{DLMO}(f,x) =$ Fourier transform of the DLMO-corrected shot gather, $w_{DLMO}(t,x)$,

$W(f,x) =$ Fourier transform applied to the time axis of a shot gather, $w(t,x)$,

$\emptyset_j = \frac{2\pi f x}{C_f}$ and C_f= phase velocity for frequency f.

The phase velocities used for the DLMO corrections are from a 1-D velocity profile created using the multichannel analysis of surface waves method (Park et al., 1999b). The shot records are then resorted into the common receiver domain. Traces with the same receiver location are then stacked to produce a final common receiver stack referred to as the BASW image (Figure 13C). Surface wave backscatter

events caused by subsurface heterogeneities appear as linear high amplitude anomalies on the BASW image (Figure 13C).

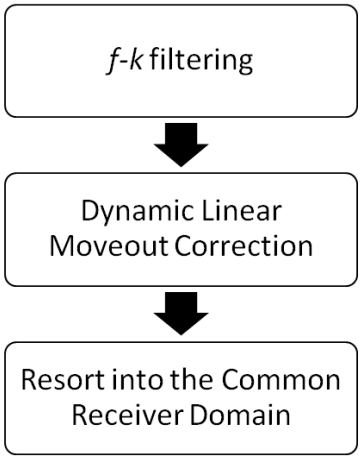

Figure 12: Standard BASW processing flow developed by Ivanov et al. (2003)

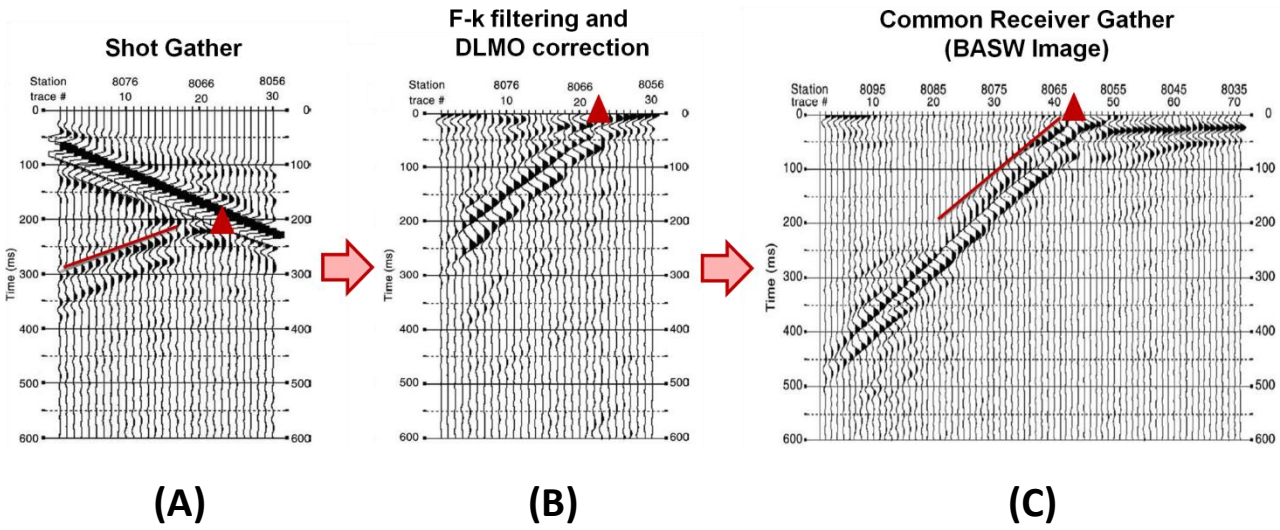

Figure 13: synthetic data example produced using the model shin in Figure 14 showing the BASW processing flow, where the red triangles indicate the receiver station located directly above the tunnel. The different panels show the **A)** one of the original shot gathers used **B)** the shot gather after applying an f-k filtering and dynamic linear moveout corrections **C)** the final BASW image (Image modified from Sloan et al. (2010))

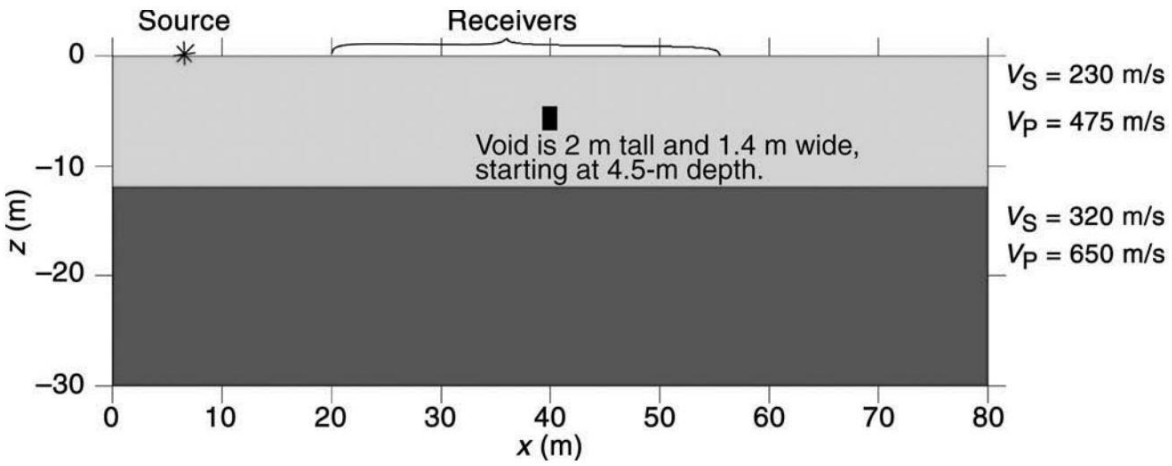

Figure 14: model used to produce synthetic data shown in Figure 13 (Image modified from Sloan et al. (2010))

3.3 Parallel-line Beamsteering

Beamsteering is an interferometric signal processing technique that applies a time shift to a signal to produce the greatest coherent stack relative to another signal (Gibbons et al., 2008). Historically, beamsteering has been applied to radar and seismic array processing. (Rost and Thomas, 2002; Meschino et al., 2009) . The theory behind this method is that an identical signal from a laterally homogeneous earth is recorded at different array stations only shifted in time as a result of different travel paths from the source to the receiver stations (Figure 15) (Gibbons, et al., 2008; Piper, 2011). By correcting for this time shift and stacking time series from each station the signal will coherently add and random and coherent noise will be destructively added (Figure 16) (Peter, 1968; Evernden, 1969; McCowan, 2001). As a result, this will enhance the signal and thereby increase the signal-to-noise ratio (McCowan, 2001; Ogah and Chinedu, 2012).

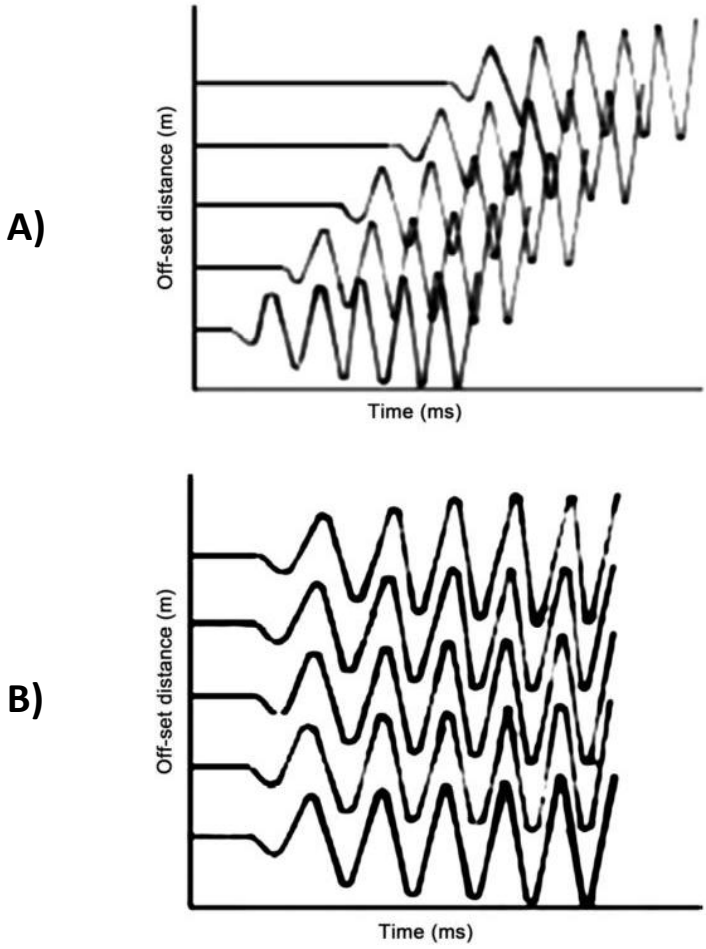

Figure 15: A) signal recorded by seismic array stations at different offset distances **B)** Signal after correcting for time shift (Image modified from Ogah and Chinedu (2012))

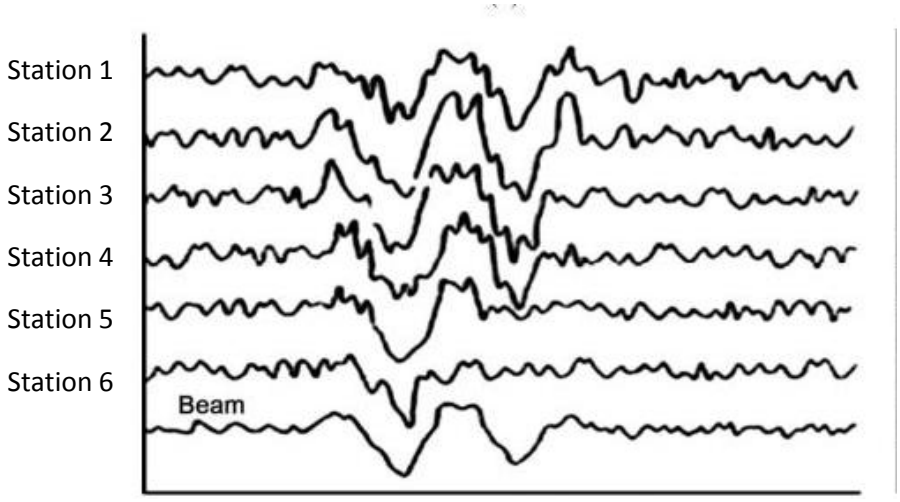

Figure 16: Signal recorded by seismic array stations displayed after correcting for time shift. The bottom signal indicates the beam produced after stacking the signal from each array station. (Image modified from Ogah and Chinedu (2012))

Parallel seismic lines can be used as sub-arrays and the same shift and stack concepts of beamsteering applied to enhance signal. This idea of stacking parallel seismic lines to enhance scatter from localized horizontal anomalies (e.g. a tunnel) and attenuate scatter from other laterally discontinuous heterogeneities has been conceptualized but lacked the computational mechanisms to implement (Rick Miller personal communication). This thesis expands this concept and establishes a method called parallel-line beamsteering to make the concepts practical.

Parallel-line beamsteering utilizes the geometric relationship between parallel receiver lines and a laterally continuous void such as a tunnel. When seismic data are acquired along two parallel receiver lines that are collected perpendicular to the long axis of the tunnel, equivalent shot locations along each line at identical relative spatial locations have the same source receiver configuration with respect to the tunnel. The raypaths of scattered waves from the tunnel should be identical (Figure 17) resulting in similar shot records (Figure 18). These shot gathers with equivalent scattered energy from the tunnel can be stacked, enhancing the signal of the tunnel and attenuating coherent wavefield components with raypaths that are not identical on both lines. Using this approach, scattered waves (e.g. diffractions and surface wave backscatter) from laterally continuous features like a tunnel or other uniformly elongated voids will coherently stack. Noise from localized non-laterally continuous features (e.g. clay lens, boulder) will destructively interfere during vertical receiver stack.

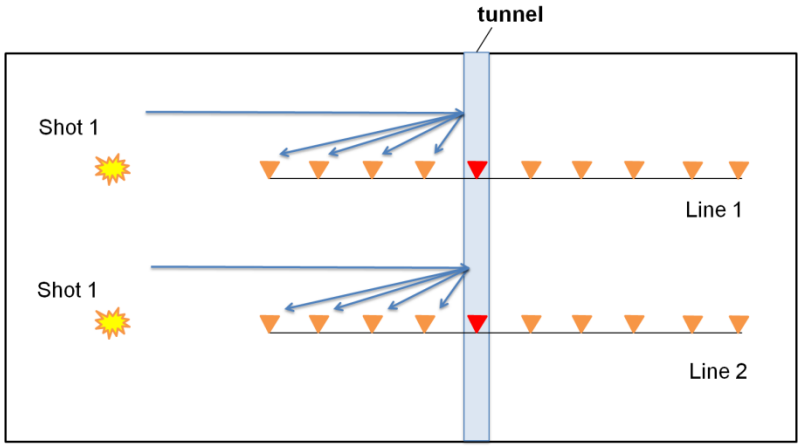

Figure 17: survey map showing receiver lines, Line 1 and 2, collected parallel to each other and perpendicular to a tunnel. Blue arrows depict raypaths for a wave traveling from shot locations.

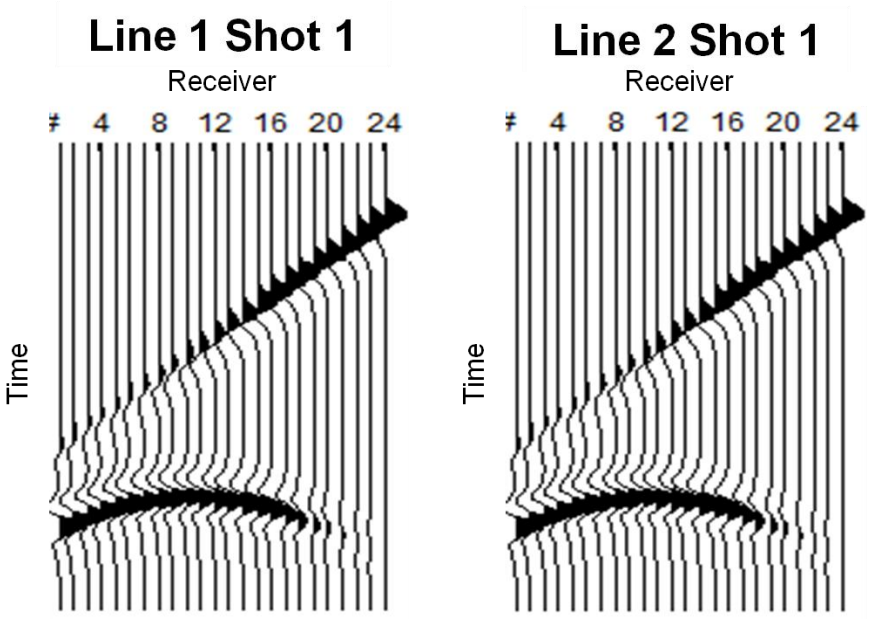

Figure 18: synthetic seismic shot records for Line 1 Shot 1 and Line 2 Shot 1 generated using model geometry shown in Figure 17

The BASW results for data from one receiver line collected over the model tunnel (Figure 19) has three high amplitude backscatter events associated with the tunnel and two buried objects (Figure 20A). Stacking data from three parallel receiver lines collected over the same tunnel and near the two objects results in one high amplitude backscatter event associated with the tunnel and two lower amplitude

events associated with the objects (Figure 20B). The backscatter events associated with the two buried objects are destructively stacked because they have different offline offset distances from the three parallel lines, resulting in different arrival times for the surface wave backscatter. The coherently scattered energy associated with the tunnel adds constructively due to the linear geometry of the tunnel. This results in similar arrival times of surface wave backscatter from the tunnel on each line. This model demonstrates the simplest case for lines collected perpendicular to a tunnel where no offset shift is needed to optimize stacking.

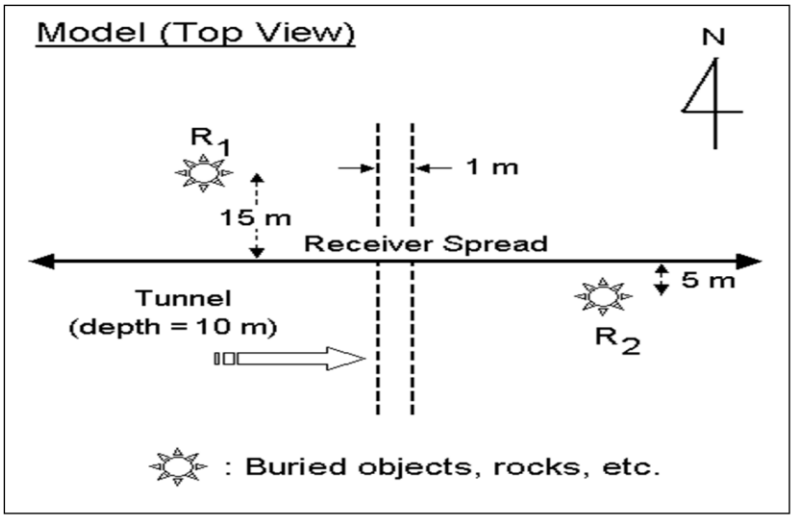

Figure 19: top view of the model used to create synthetic data in Figure 20 for receiver lines collected over a tunnel near two buried objects, R1 and R2 (Image created by Choon Park)

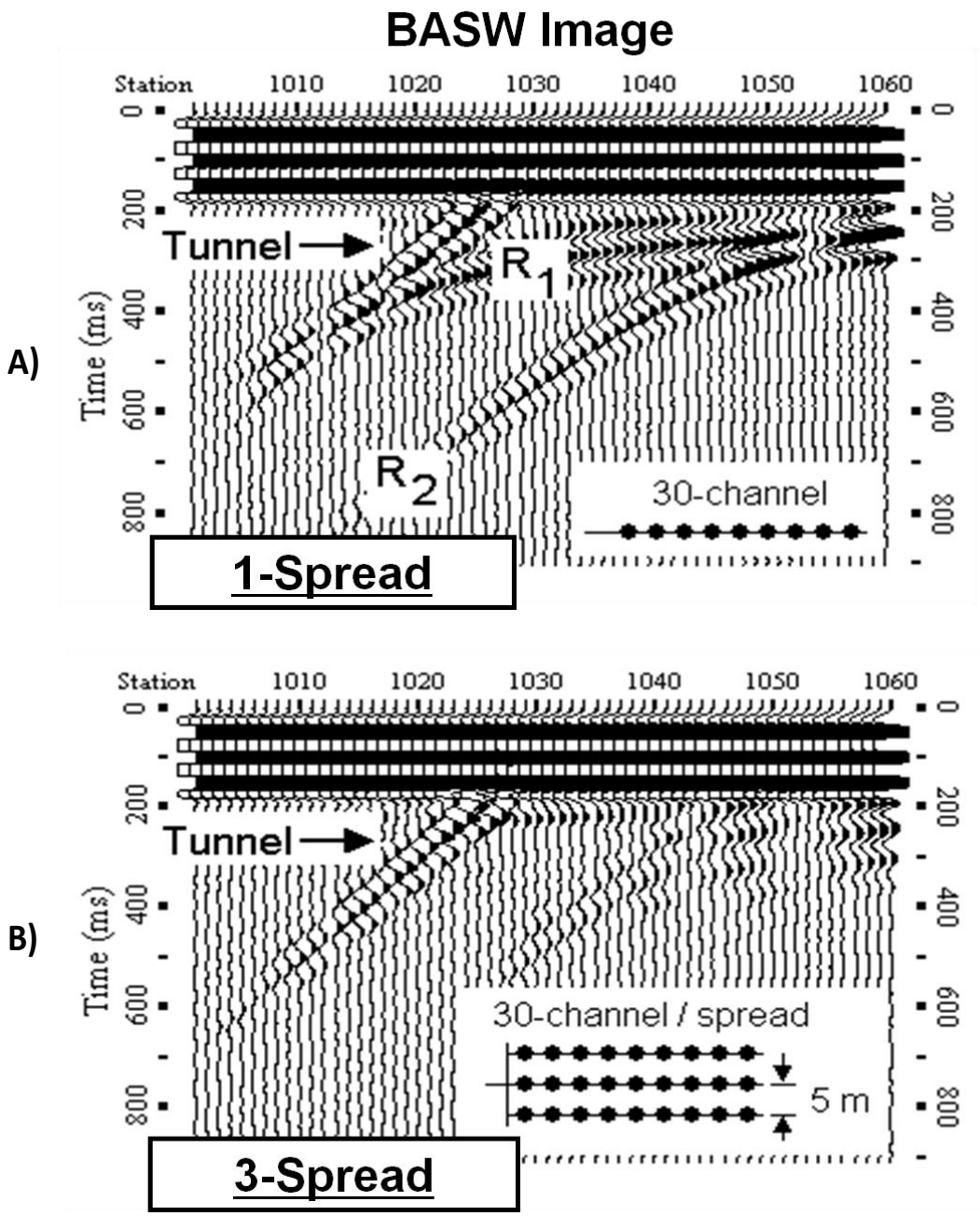

Figure 20: A) BASW image created using data from one receiver line **B)** BASW image created after stacking data from three receiver lines (Modified from image by Choon Park)

The spatial shift aspect of parallel-line beamsteering is necessary for real world tunnel detection. Surveys done without exact knowledge of the tunnel configuration may result in receiver lines being acquired at an oblique angle to the tunnel. This is, more times than not, the real-world situation in searches for clandestine tunnel locations. In the case of an oblique tunnel, equivalent shot locations on different lines do not have the same offset to the tunnel (Figure 21). Synthetic data created using a standard acquisition configuration (Figure 21) and generalized model parameters (Figure 22) demonstrate these similar shot locations do not have the same arrival time for equivalent scattered energy (Figure 23). Stacking shot records from equivalent shot locations on each line without spatial adjustment for oblique orientation attenuates signal from the tunnel because the arrival time of scatter events is different for different source offsets.

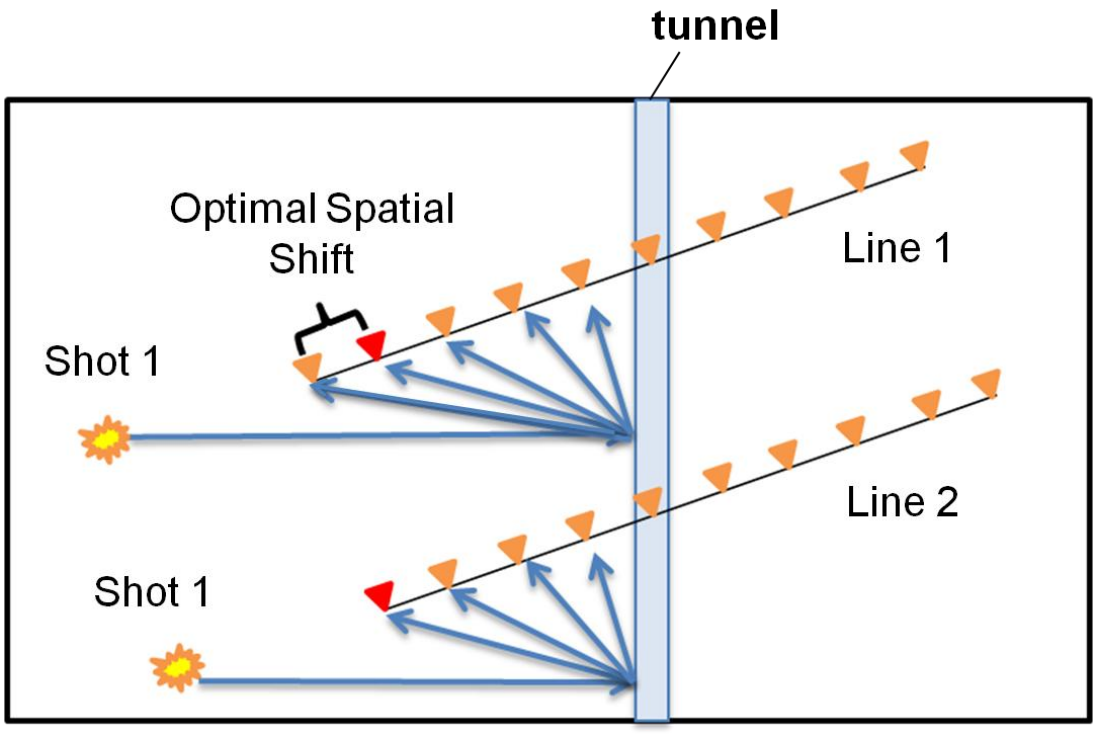

Figure 21: survey map showing parallel lines, Line 1 and 2, collected parallel to each other and at an oblique angle to a tunnel. Blue arrows depict raypaths for a wave traveling from shot location 1 on each line. The shift refers to the difference in the distance from Shot 1 on Line 1 to the tunnel and the distance from Shot 1 on Line 2 to the tunnel.

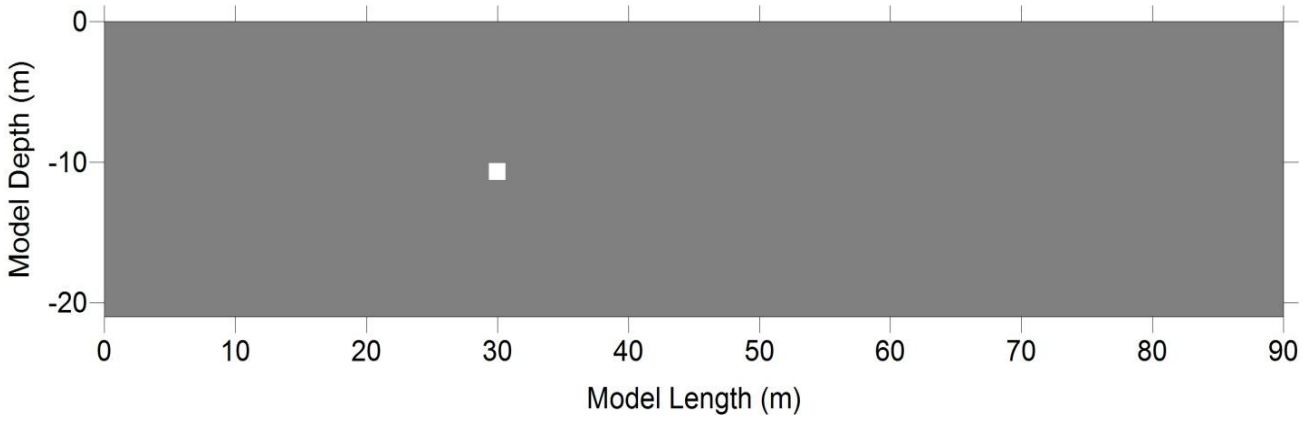

Figure 22: 1000 m/s compressional wave velocity model with a 1.2 by 1.2 m air filled tunnel used to create synthetic data shown in Figure 23 and 24

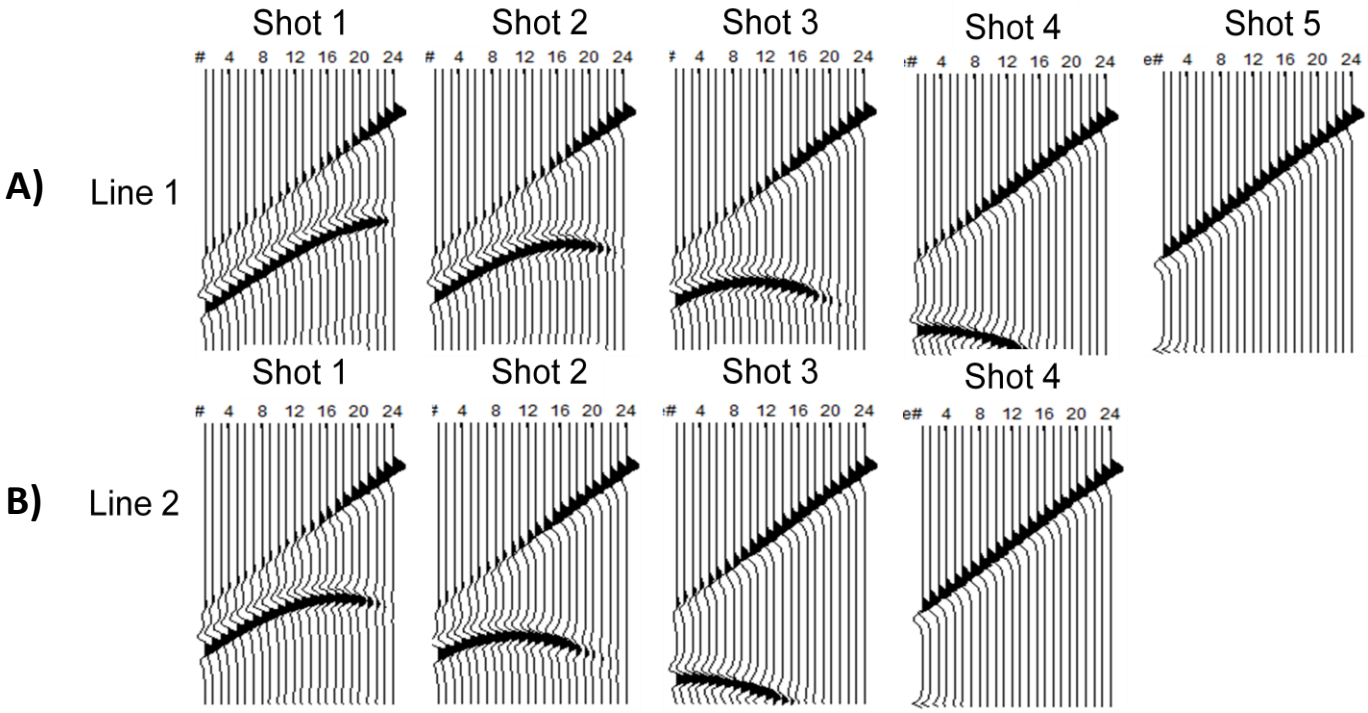

Figure 23: synthetic data produced using a one layer Vp model containing an air filled tunnel shown in Figure 22 **A)** Line 1 shot records **B)** Line 2 shot records

Therefore, a method is needed to determine which shot locations have the same source-tunnel offset, allowing application of the appropriate spatial shift before stacking data to enhance signal from the tunnel. The distance between the equivalent shot locations and the shot location with the same source-tunnel offset is referred to as the optimal spatial shift (Figure 21). Correctly accounting for this oblique tunnel angle with the optimal spatial shift (Figure 24 and 25) allows stacking of shot records containing the same scattered energy arrival time at the same relative trace location.

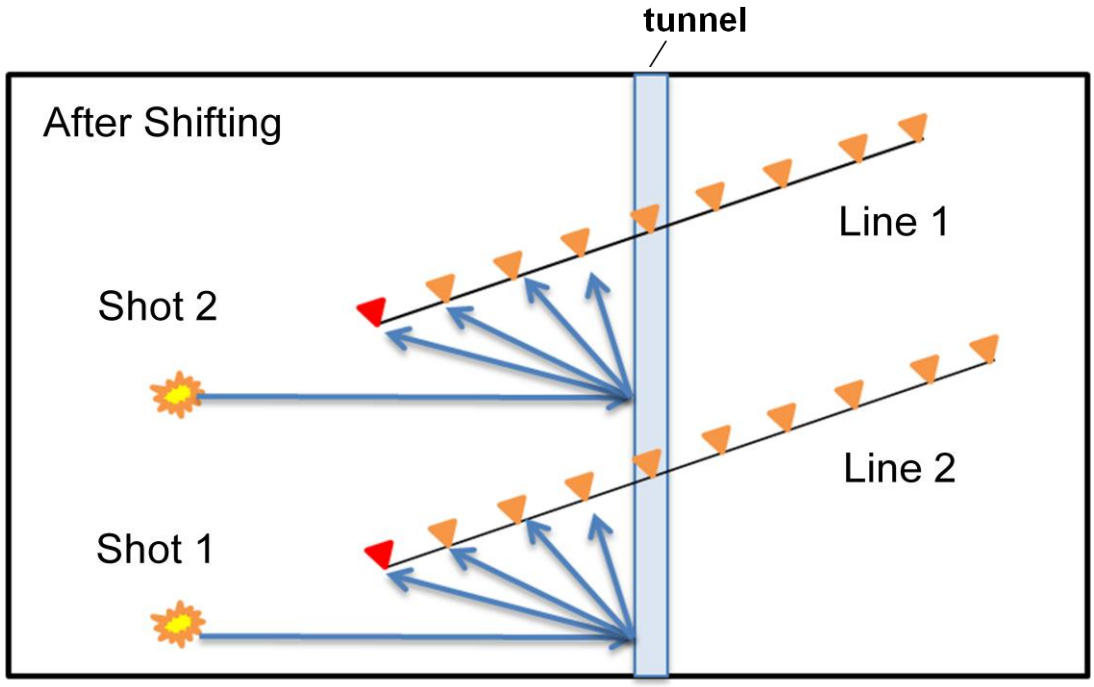

Figure 24: survey map showing how an offset shift is applied to parallel lines, Line 1 and 2, collected parallel to each other and perpendicular to a tunnel. Blue arrows depict raypaths for a wave traveling from shot locations that have the same source-tunnel offset on each line.

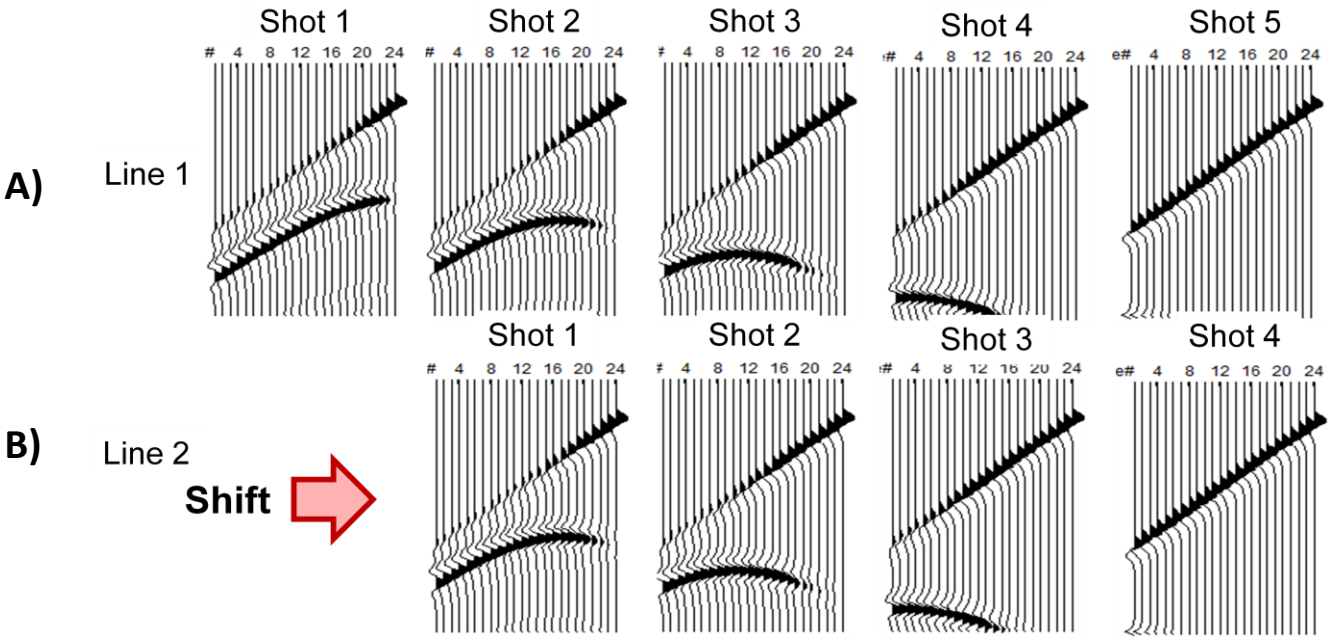

Figure 25: synthetic data produced using a one layer Vp model containing an air filled tunnel shown in Figure 20 **A)** Line 1 shot records **B)** Line 2 shot records shifted by one shot location station to match the shot-tunnel offset of Line 1

Information about the tunnel orientation can also be determined using this optimal spatial shift. The shift distance and the offset distance between the lines have a unique geometric relationship (Figure 26). Knowledge of these distances allows calculation of the angle of the tunnel (θ) relative to the survey trajectory using the cotangent function where:

$$\theta = \cot^{-1}\left(\frac{Line\ Offset}{Shift}\right) \quad (5)$$

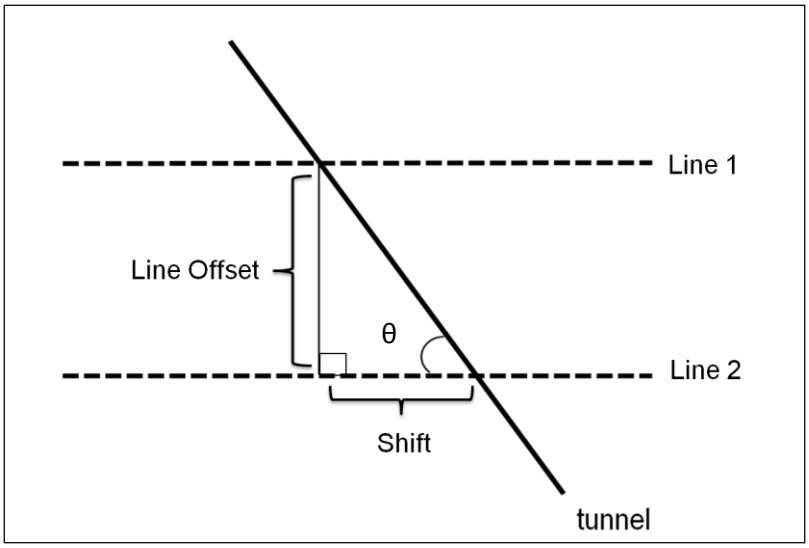

Figure 26: geometric relationship between the special shift distance, the line offset, and the angle of the tunnel with respect to parallel seismic lines, Line 1 and 2 (Modified from image by Shelby Peterie)

4. Data Sets

4.1 Field Data Acquisition

Field data used for method development and verification were collected at the JTTR in December of 2011. The seismic source was an accelerated weight drop (Figure 27) with a source to nearest receiver offset of 36.6 m. Receiver lines consisted of 4.5 Hz and 40 Hz vertical geophones co-located in a 24-station 48 channel towed landstreamer at intervals of 1.2 m (Figure 28).

Figure 27: bungee assisted accelerated weight drop (Photos from the Kansas Geological Survey)

(A) **(B)**

Figure 28: A) 24 station towed landstreamer **B)** landstreamer receiver station configuration (Photos from the Kansas Geological Survey)

Three sets of parallel seismic lines were collected perpendicular to the tunnel. These lines were acquired along two unique line locations with line separation of 14 m and offset to the vertical shaft allowing access to the tunnel of 26 m and 40 m (Figure 29A). Data were collected along these line locations three unique times resulting in data sets referenced to as Line 3-8. Odd numbered lines correspond to the profiles nearest the vertical shaft (Figure 29A). One set of parallel lines was collected (Line 9 and 10) at an oblique angle to the tunnel with a line offset of 12 m (Figure 29B).

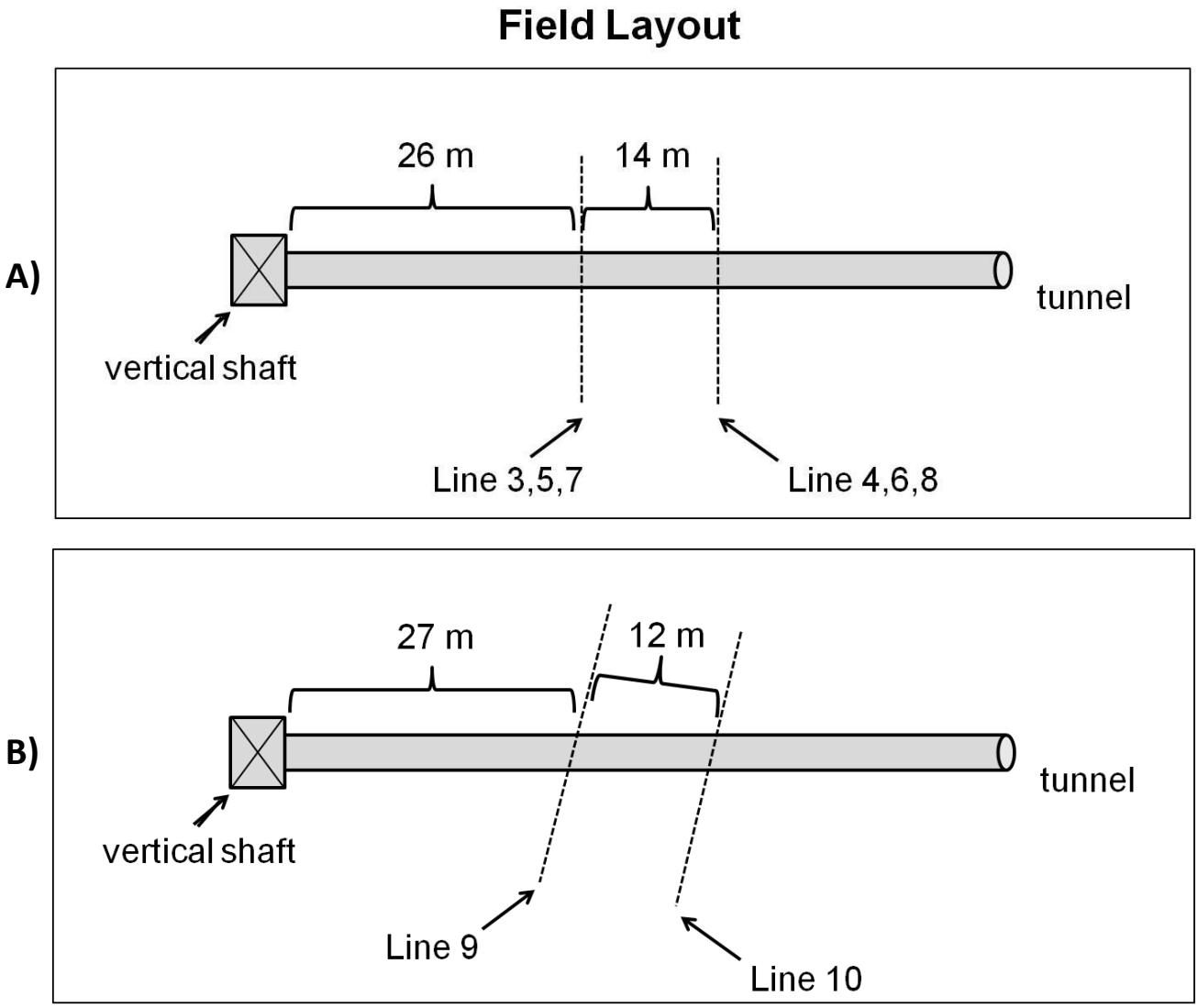

Figure 29: A) 2011 JTTR survey perpendicular line field layout **B)** YPG 2011 oblique line field layout (Image modified from image by Shelby Peterie)

4.1 Field Data Processing Parameters

Diffraction imaging was applied to data recorded using 40 Hz natural frequency geophones after applying a trapezoidal low cut filter with corner frequencies of 0 Hz, 0 Hz, 35 Hz, and 70 Hz, a 198-975.6 m/s *f-k* filter, and a 100 ms window AGC. The 670 m/s velocity used to correct the hyperbolic moveout was determined by measuring the direct compressional wave velocities from the data set (Shelby Peterie personal communication). BASW was applied to data recorded using 4.5 Hz natural frequency geophones data after application of a 91.5 - 1219.5 m/s *f-k* filter. Dispersion curves used for BASW were picked for initial processing of these data as part of standard analysis in 2011 by KGS staff. The picked dispersion curves contain a mix of fundamental and higher mode energy.

4.3 Synthetic Data Generation

Finite-difference elastic wave modeling software developed at the Kansas Geological Survey (Zeng, 2011) was used to produce shear wave, compressional wave, and density models. An eight node 32 CPU cluster was used to compute the wavefield and generate shot gathers.

Models consisted of one layer with a 1.2 by 1.2 m air filled tunnel buried at 10 m (Figure 30). The key model properties used were a 1000 m/s compressional wave velocity, a 600 m/s shear wave velocity, and a 1.7 g/cm^3 density. The source wavelet was a 200 Hz first derivative Gaussian. A classic 2D style roll along survey was simulated using 48 receivers with a receiver spacing of 1.2 m, shot offset of 1.2 m, and a roll increment of 1.2 m (Figure 31)

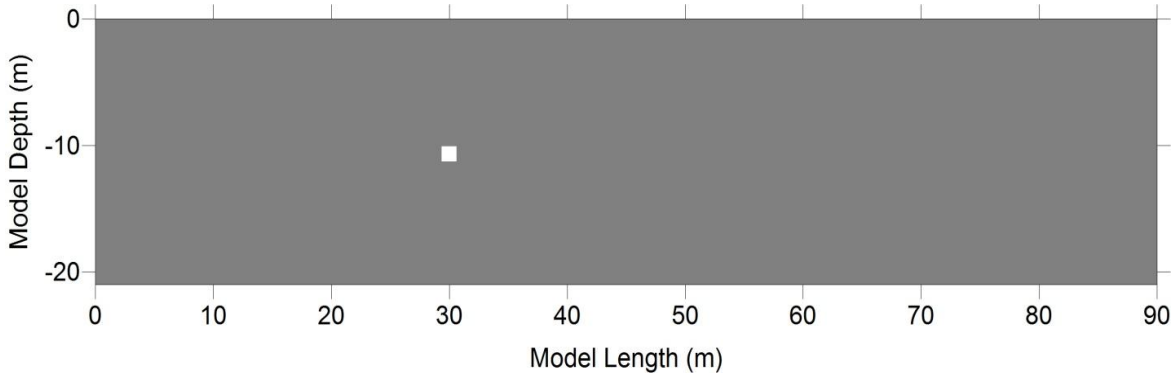

Figure 30: Model geometry of models used to create synthetic data shown in Figure 29

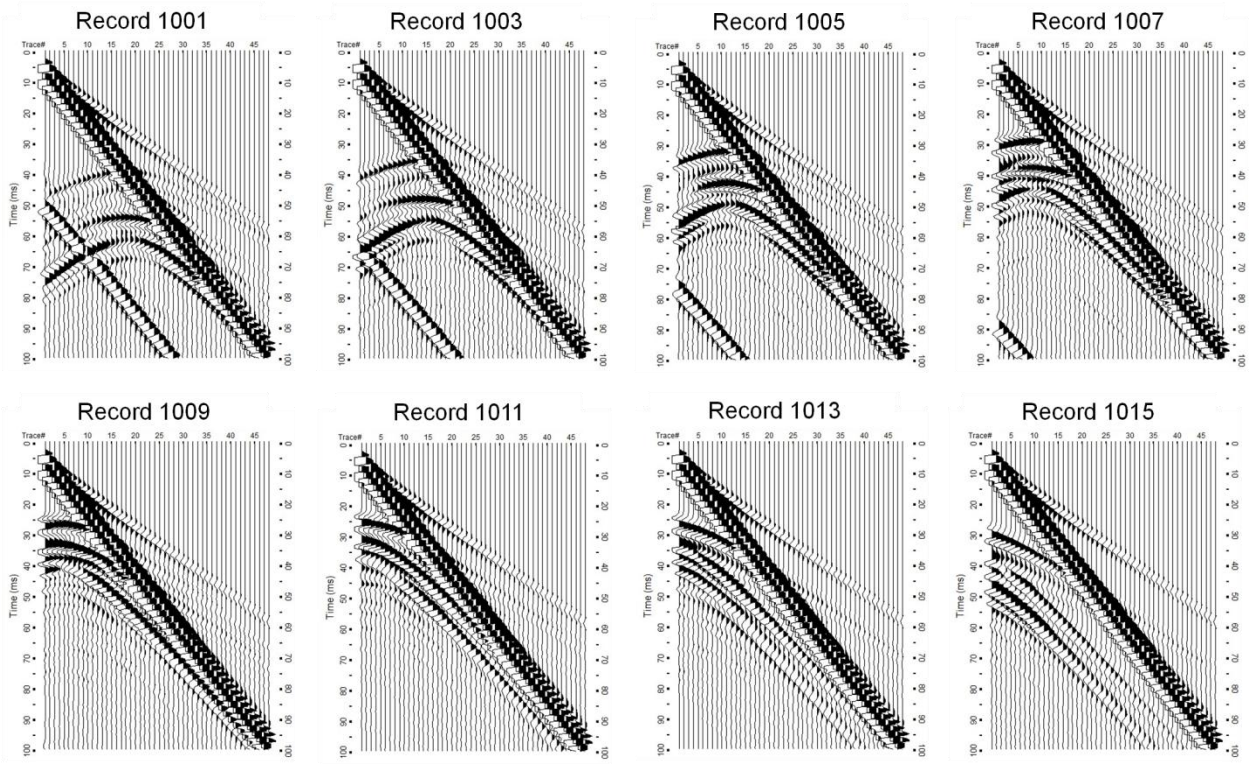

Figure 31: Synthetic shot records produced using a one layer model (Figure 28)

5. Parallel-line Beamsteering Method Development

The basic concept of stacking parallel receiver lines to coherently enhance scatter from a tunnel and attenuate scatter from other, less regular, heterogeneities was conceived by researchers at the Kansas Geological Survey. Development and implementation of the method had never been pursued. Taking parallel-line beamsteering from a concept and making it into a robust processing method was a main focus of this thesis research. This section details the development of the processing flow for applying parallel-line beamsteering diffraction imaging and BASW.

5.1 Stacking

The two main processing steps used for parallel-line beamsteering are shifting and stacking. The simplest case of applying parallel-line beamsteering is when parallel lines are collected perpendicular to a horizontal tunnel and no relative spatial shift is required. This simplest case was the starting point for method development and allowed for rapid testing of stacking methods independent of the shift operation. Optimized stacking required evaluation of implementing the stacking operation at different steps in the diffraction imaging (Figure 32) and BASW (Figure 34) processing flow. This evaluation was undertaken using three sets of parallel-line data.

Data were extracted after four different logical steps in the diffraction imaging processing flow and underwent parallel-line stacking to determine the best point in the data processing flow to apply stacking for optimum enhancement of the tunnel. Shot gathers were stacked before pre-processing, which includes applying a low cut filter, *fk*- filtering data, and applying gain (Figure 32A). Shot gathers were stacked after pre-processing (Figure 32 B). Shot gathers were stacked after the diffraction moveout correction in the common shot domain (Figure 32 C). The final receiver gathers produced from diffraction imaging were stacked (Figure 32 D).

For the example discussed in this section, data collected along lines 5 and 6 (Figure 33) were utilized. These four stacking routines were assessed by comparing the relative seismic signal corresponding to the tunnel with respect to the average background noise. Calculating the relative seismic signal with respect to the average background noise quantifies the signal-to-noise ratio of the data. The relative seismic signal value which is measured in decibels (dB) was calculated using Equation 6 where a_1 is the amplitude of the signal corresponding to the tunnel and a_2 is the amplitude of the average background signal (Bormann, 2013).

$$deciBels = \ dB = log_{10}\left(\left(\frac{a_1}{a_2}\right)^2\right) \quad (6)$$

The amplitude of the signal corresponding to the tunnel (a_1) was determined by choosing the largest amplitude value for the amplitude anomaly on the diffraction images whose arrival time corresponds to signal from the tunnel. The amplitude anomaly corresponding to the tunnel is located at receiver station 3027. The amplitude of the average background signal (a_2) was calculated by averaging all the amplitude values extracted from the diffraction image from 0-250 ms.

Stacking shot gathers after pre-processing resulted in the highest relative seismic signal (7.2 dB) of all four stacking routines (Figure 33 B). The relative seismic signal calculated from the diffraction image produced by stacking before pre-processing was 5.7 dB (Figure 33A). The difference in these two values implies that stacking after pre-processing is more effective at enhancing the signal from the tunnel relative to background signal. Upon visual inspection of the diffraction images (Figure 33A and 33B) there are fewer high amplitude events in the diffraction image produced when applying stacking after pre-processing. This suggests that noise from the unfiltered data may have been coherently stacked.

Stacking shot gathers after the diffraction moveout correction in the common receiver gather resulted in a diffraction image that appears to be nearly identical to the diffraction image produced after

stacking final diffraction images (Figure 33C and 33D). This was also reflected in their relative seismic signal values, which were 4.5 dB and 4.7 db. These values are low in comparison to the 7.2 dB calculated from the diffraction image produced after stacking shot gather after pre-processing, implying that these stacking routines are less efficient at enhancing signal from the tunnel (Figure 33B). Visually ,this appears to be the case based on the amplitude of the anomaly corresponding to the tunnel location at receiver location 3027(Figure 33B, 33C and 33D). These results were verified for two other data sets, Lines 3 and 4 and Lines 7 and 8.

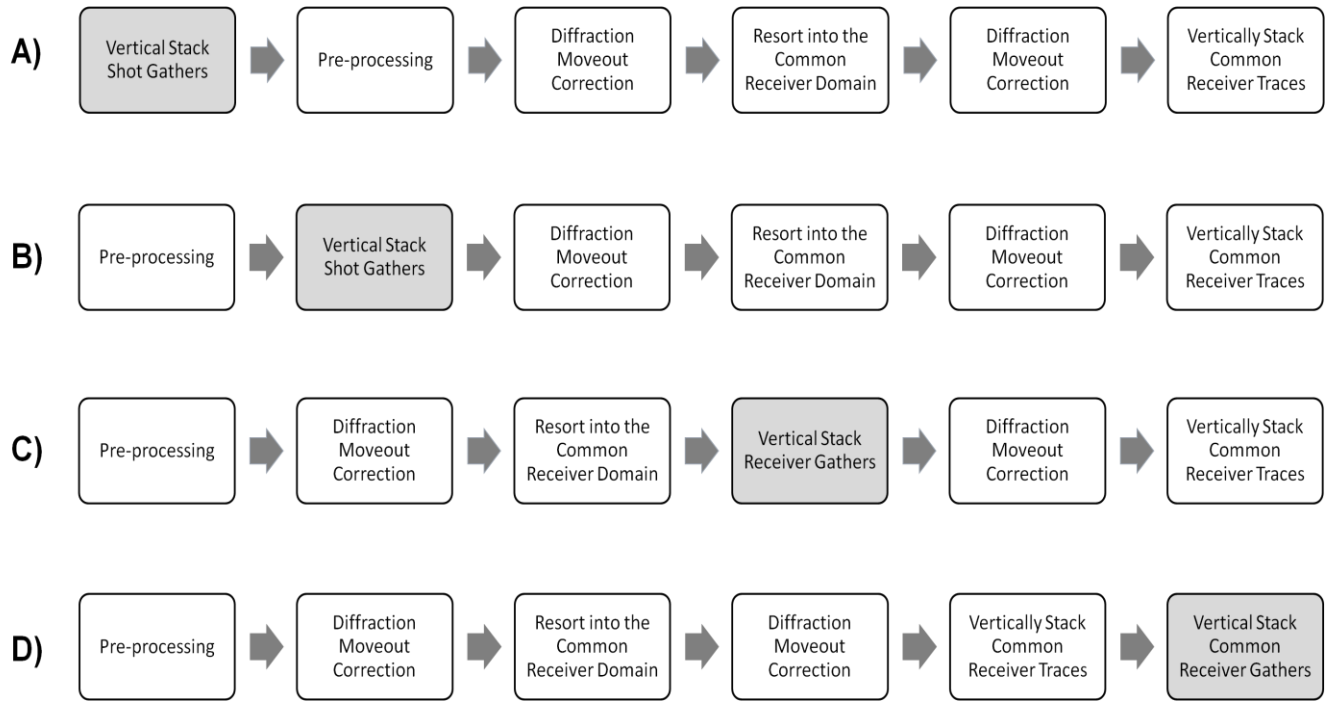

Figure 32: Diffraction imaging processing flows depicting different parallel-line stacking operations A) shot gathers are stacked before pre-processing B) shot gathers are stacked after pre-processing C) receiver gathers are stack after diffraction moveout correction is performed in the common shot domain and resorting into the common receiver domain D) final diffraction images or the common receiver gathers are stacked

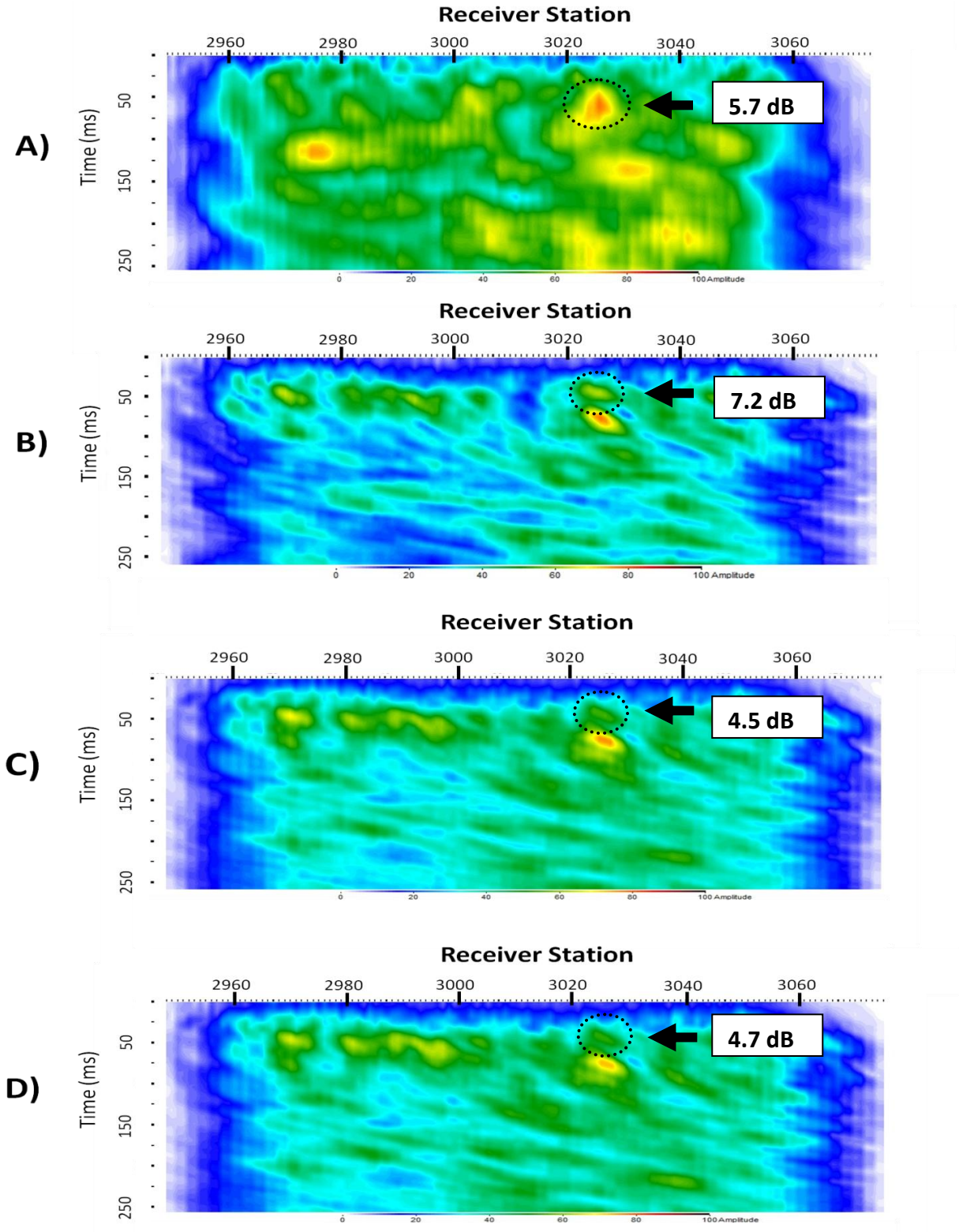

Figure 33: diffraction image produced using data collected along Line 5 and 6 using the stacking routine outlined in **A)** Figure 30A **B)** Figure 30B **C)** Figure 30C **D)** Figure 30D, black arrows indicate signal associated with the tunnel and the calculated relative seismic signal value is listed

Three options in the processing flow for BASW were tested to determine optimum parallel-line stacking. Shot gathers were stacked before *fk*-filtering and after *fk*-filtering (Figure 34A and 34B). Also, final common receiver gathers produced from BASW processing were stacked (Figure 34C). Three sets of lines collected perpendicular to the tunnel were used to evaluate these processing flows. The efficiency of the different stacking routines was assessed by calculating the relative seismic signal of the backscattered signal with respect to the average background signal using Equation 6. The amplitude of the backscattered signal (a_1) was determined by picking the highest amplitude sample associated with the backscattered signal. The amplitude of the average background signal (a_2) was calculated by averaging all of the amplitude values extracted from the BASW image from 0-250 ms.

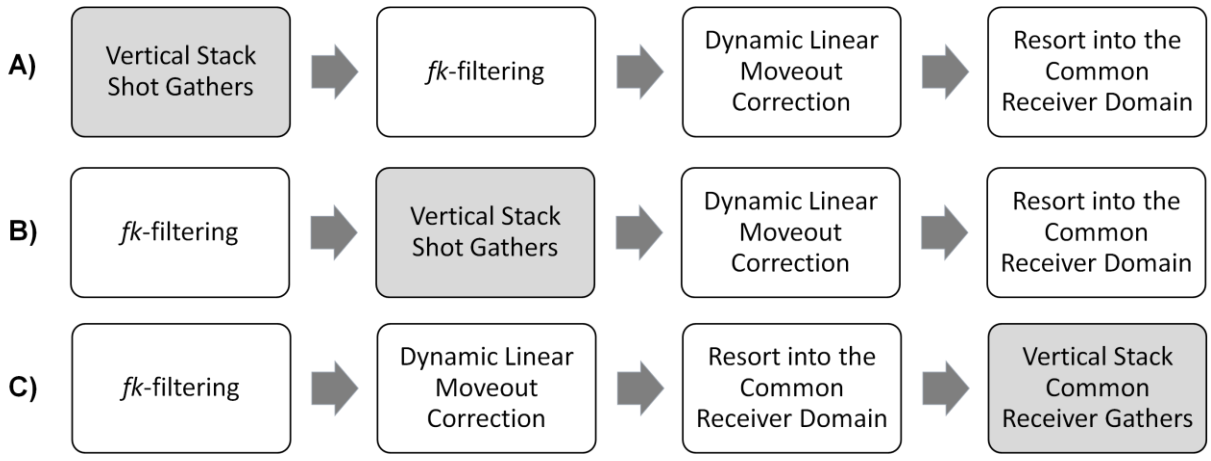

Figure 34: BASW processing flows depicting different parallel-line stacking operations A) shot gathers are stacked before *fk*-filtering B) shot gathers are stacked after *fk*-filtering C) final BASW images or common receiver gathers are stack

Stacking shot gathers before and after filtering produced very similar looking BASW images (Figure 34A and 34B) and relative seismic signal values of 12.0 dB and 11.9 dB respectively. The final BASW image obtained after stacking BASW images (Figure 34C) appears to have less high amplitude

background signal than the images produced from stacking shot gathers. Stacking the final receiver gathers resulted in the highest value for the relative seismic signal (14.2 dB) suggesting that this is the most efficient stacking operation. These results have also been confirmed using two other line pairs, of Lines 5 and 6 and Lines 7 and 8.

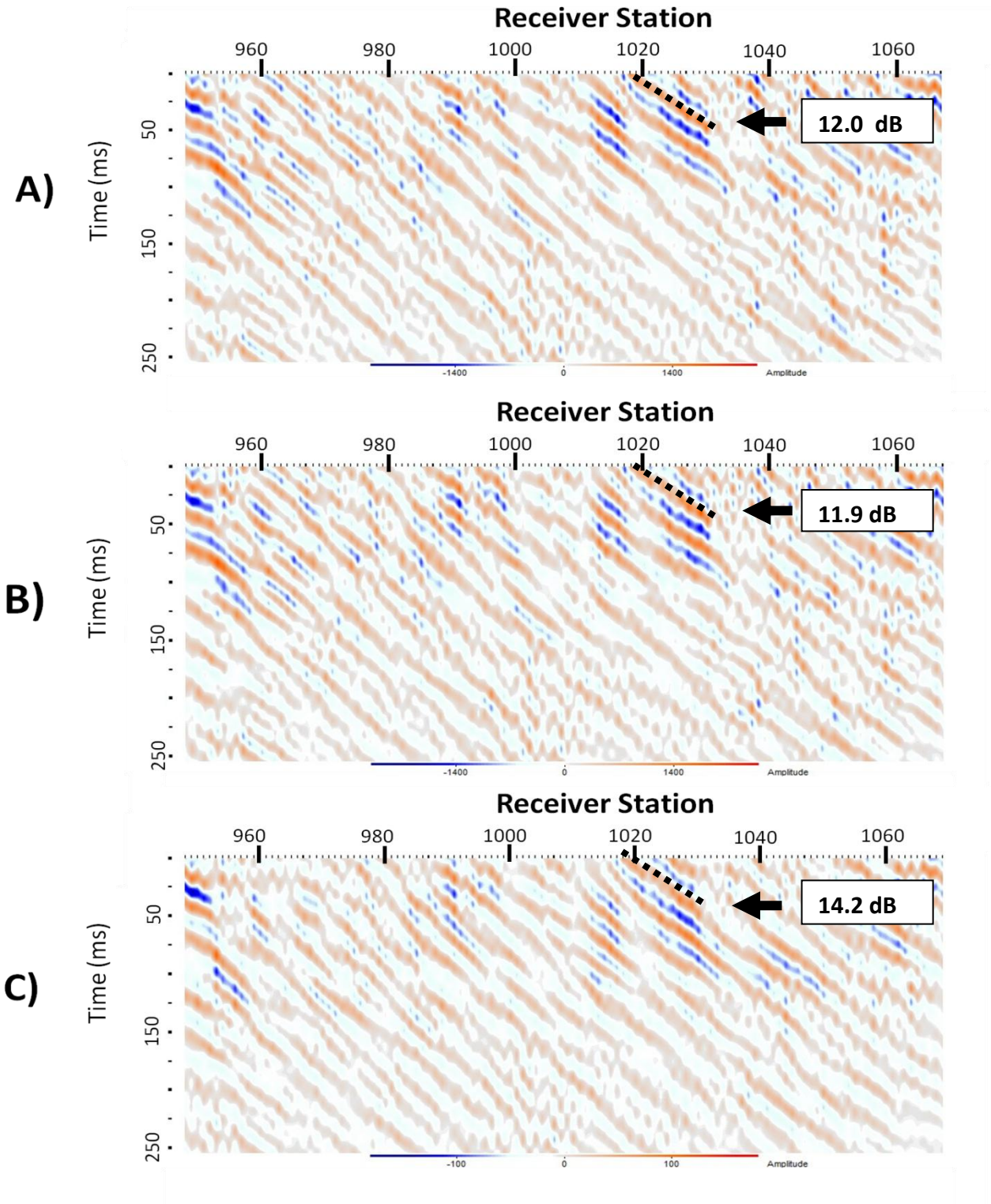

Figure 35: Final BASW image after stacking Line 3 and 4 **A)** un-filtered shot records **B)** filtered shot records **C)** BASW images, black arrow indicates the signal associated with the tunnel and the calculated relative seismic signal value is listed, the dotted black line indicates the first arrival time of backscattered energy

5.2 Shifting

After determining how best to stack parallel-line data, methods needed to be refined for determining the optimal spatial shift for oblique tunnel crossings. Two methods were evaluated for determining the optimum spatial shift for BASW and diffraction imaging results across a range of tunnel angles. One method, range analysis, uses interpretation of the final BASW and diffraction images produced using several spatial shifts assuming a range of possible tunnel angles to determine the optimal shift. A more quantitative approach to determining the optimal spatial shift, signal similarity analysis, applies 2D correlation principles to decrease need of skilled interpretation. The goal of any alignment method is to establish the optimal spatial shift without knowledge of the orientation or location of the tunnel.

5.2.1 Range Analysis

Data from two parallel lines at the JTTR in YPG (Line 9 and 10) were collected at an oblique angle to the tunnel allowing evaluation of the feasibility of enhanced diffraction imaging through parallel-line stacking for a range of spatial shifts. A simple quantitative test of the method was run for a range of spatial shifts of Line 10 relative to Line 9 prior to stacking. Five different spatial shifts were applied to produce beamsteered enhanced diffraction images (Figure 36).

After stacking, a high amplitude anomaly corresponding to receiver station 3030 suggests the correct shift is 7.2 m (Figure 36D). All of the shifts applied produce high amplitude anomalies that could be interpreted as signal from a possible tunnel (Figure 36). For this example, without the knowledge that the lateral location of the tunnel corresponds to receiver station 3030, the optimal spatial shift would not be able to be determined. Therefore, analysis of diffraction imaging results using a general range of values of spatial shifts may not be feasible for optimizing the spatial shift necessary to improve the signal-to-noise ratio of the signal from a tunnel. Additionally, the applied spatial shifts were

increments of the 2.4 m source spacing. For this case if the correct spatial shift for optimal stacking was not a multiple of 2.4 m the tunnel signal may not coherently stack.

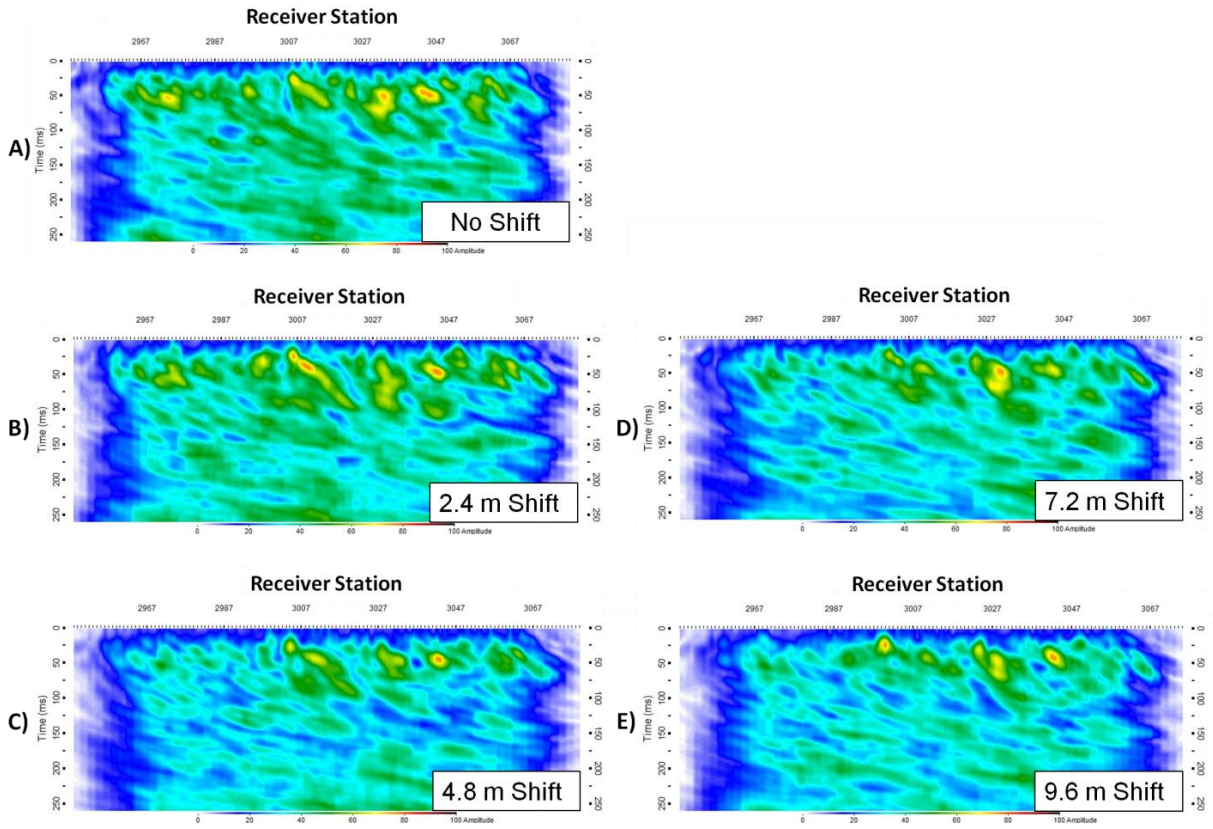

Figure 36: diffraction images after stacking pre-processed shot records from Line 9 and 10 and applying a spatial shift to Line 10 of **A)** no shot stations (0 m) **B)** one shot station (2.4 m) **C)** two shot stations (4.8 m) **D)** three shot stations (7.2 m) **E)** four shot stations (9.6 m), the lateral location of the tunnel corresponds to receiver station 3033

Data from Lines 9 and 10 were used to evaluate the feasibility of enhanced BASW through parallel-line stacking for a range of seven spatial shift values. A spatial shift was applied to the final BASW image produced using Line 10 data before stacking with the final BASW image produced using Line 9 data. . These spatial shift values applied to final BASW images are limited to receiver spacing. For this BASW test case a shift of five receiver stations (6.0 m) has lower signal-to-noise ratio than the other beamsteered enhanced BASW images (Figure 37). The backscattered energy associated with the tunnel is more concentrated at receiver station 3030 after applying the 6.0 m spatial shift before stacking (Figure 37F).

These tests suggest beamsteered enhanced BASW images can benefit from testing parallel-line stacking across a range of spatial shifts. However, this shifting method relies heavily on skilled interpretation to determine the optimal spatial shift. One limitation is the dependency on the proper spatial shift being a multiple of the receiver spacing. An additional limitation for this method is the possibility of coherently stacking scatter events from unrelated heterogeneities and misinterpreting these as coherently stacking scatter from a linear heterogeneity that intersect both lines such as a tunnel. This method also requires a great deal of time and therefore may not be applicable to real time processing and interpretation.

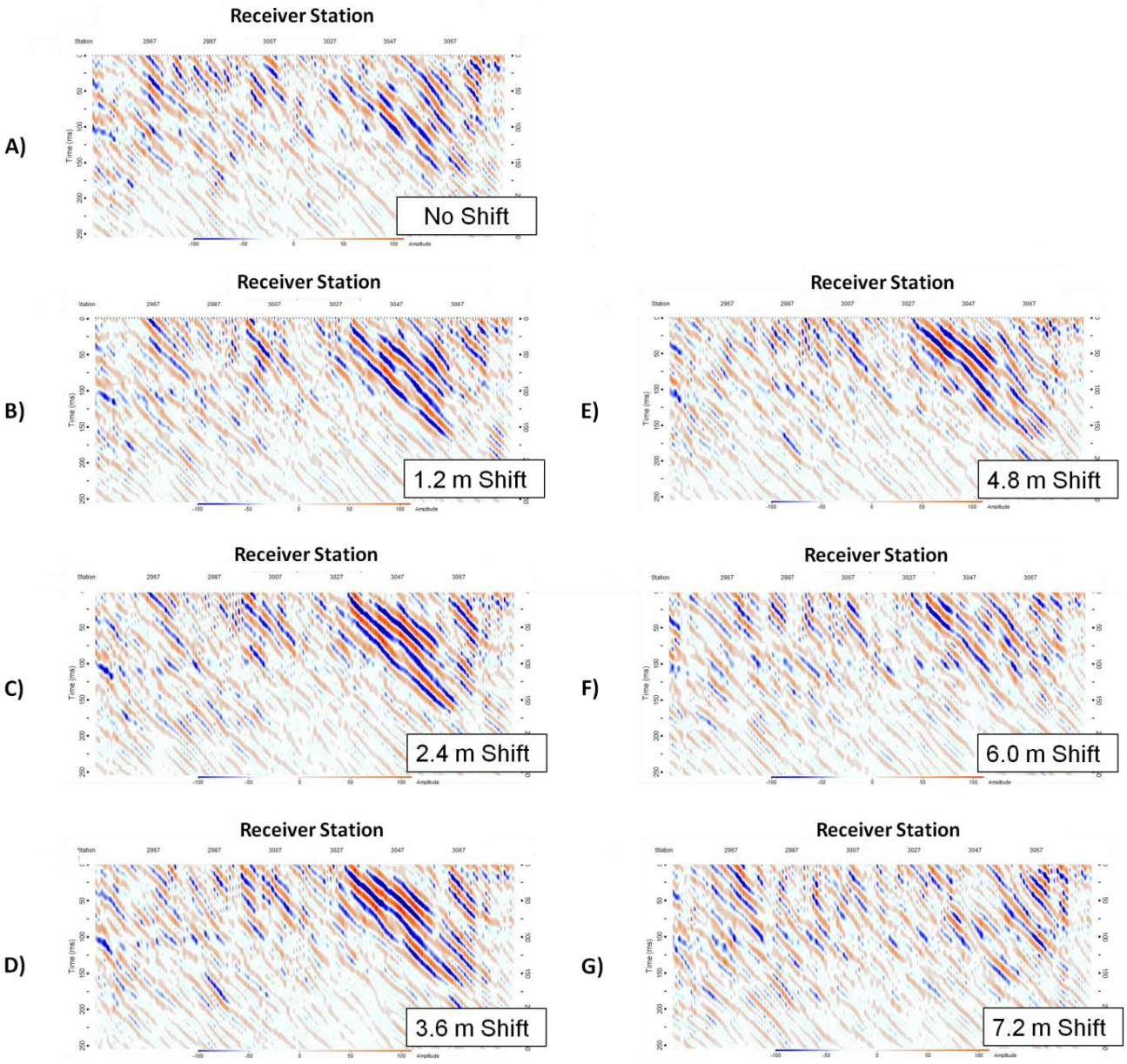

Figure 37: BASW images after stacking Line 9 and 10 common receiver gathers using a spatial shift of **A)** no shot stations (0 m) **B)** one receiver station (1.2 m) **C)** two receiver stations (2.4 m) **D)** three receiver stations (3.6 m) **E)** four receiver stations (4.8 m) **F)** five receiver stations (6.0 m) **G)** six receiver stations (7.2 m)

5.2.2 Signal Similarity Analysis

A more quantitative approach to determining the optimal spatial shift to maximize the signal-to-noise ratio of a crossline anomaly that would lessen the need for skilled interpretation is a method using signal similarity analysis. Several mathematical approaches can be used to determine signal similarities including correlation and image similarity calculations. This section discusses algorithms that have the potential to mathematically determine signal similarities. Currently no signal similarity analysis methods are fully developed and operational for methods discussed in this document.

Correlation is a mathematical operation that can be used to quantify the degree of similarity between two signals (Rex and Roberts, 1969). Equation 7 is the mathematical definition of correlation of two continuous signals f(t) and g(t). Where the star, ☆, is the symbol for correlation and the variable τ on the right side of the equation represents lag time. For a sampled signal Equation 7 can be rewritten as shown below in Equation 8.

$$f(t)\text{☆}g(t) = \int_{-\infty}^{\infty} f(t)g(\tau + t)dt \tag{7}$$

$$f(t)\text{☆}g(t) = \sum_{-\infty}^{\infty} f(t)g(\tau + t) \tag{8}$$

At a specific lag time, τ, the result of correlation is referred to as the correlation coefficient. Shifting g(t) by differing lag times results in a series of correlation coefficients (Figure 38A). When correlating a signal with itself (autocorrelation) the largest magnitude correlation coefficient will occur when the lag time is equal to zero (Figure 38B). The largest magnitude correlation coefficient calculated when correlating two different signals (crosscorrelation) corresponds to the lag time when the signals are most similar (Figure 38A).

Table 1-8. Crosscorrelation of wavelet 2 with wavelet 1.

wavelet 2: 0 0 2 1 −1	Output	Lag
2 1 −1 0 0	−0	−4
2 1 −1 0 0	0	−3
2 1 −1 0 0	0	−2
2 1 −1 0 0	0	−1
2 1 −1 0 0	−2	0
2 1 −1 0 0	1	1
2 1 −1 0 0	6	2
2 1 −1 0 0	1	3
2 1 −1 0 0	−2	4

Table 1-10. Autocorrelation of wavelet 1.

wavelet 1: 2 1 −1 0 0	Output	Lag
2 1 −1 0 0	−0	−4
2 1 −1 0 0	0	−3
2 1 −1 0 0	−2	−2
2 1 −1 0 0	1	−1
2 1 −1 0 0	6	0
2 1 −1 0 0	1	1
2 1 −1 0 0	−2	2
2 1 −1 0 0	0	3
2 1 −1 0 0	0	4

A) **B)**

Figure 38: A) depiction of crosscorrelation between two wavelets **B)** depiction of autocorrelation (Yilmaz, 2001)

One routine to determine the optimal spatial shift applies crosscorrelation to determine which shot gathers on each line are the most similar. This method is based on the phenomena that the shape of a scattering event such as a diffraction changes as the offset between the origin source and scatter point changes (Figure 30) (Ivanov, et al., 2003). Diffractions with similar shapes on shot gathers should result in higher correlation coefficients (Figure 39). Determining which shot record pairs result in high correlation coefficients would provide enough information to determine the optimal spatial shift.

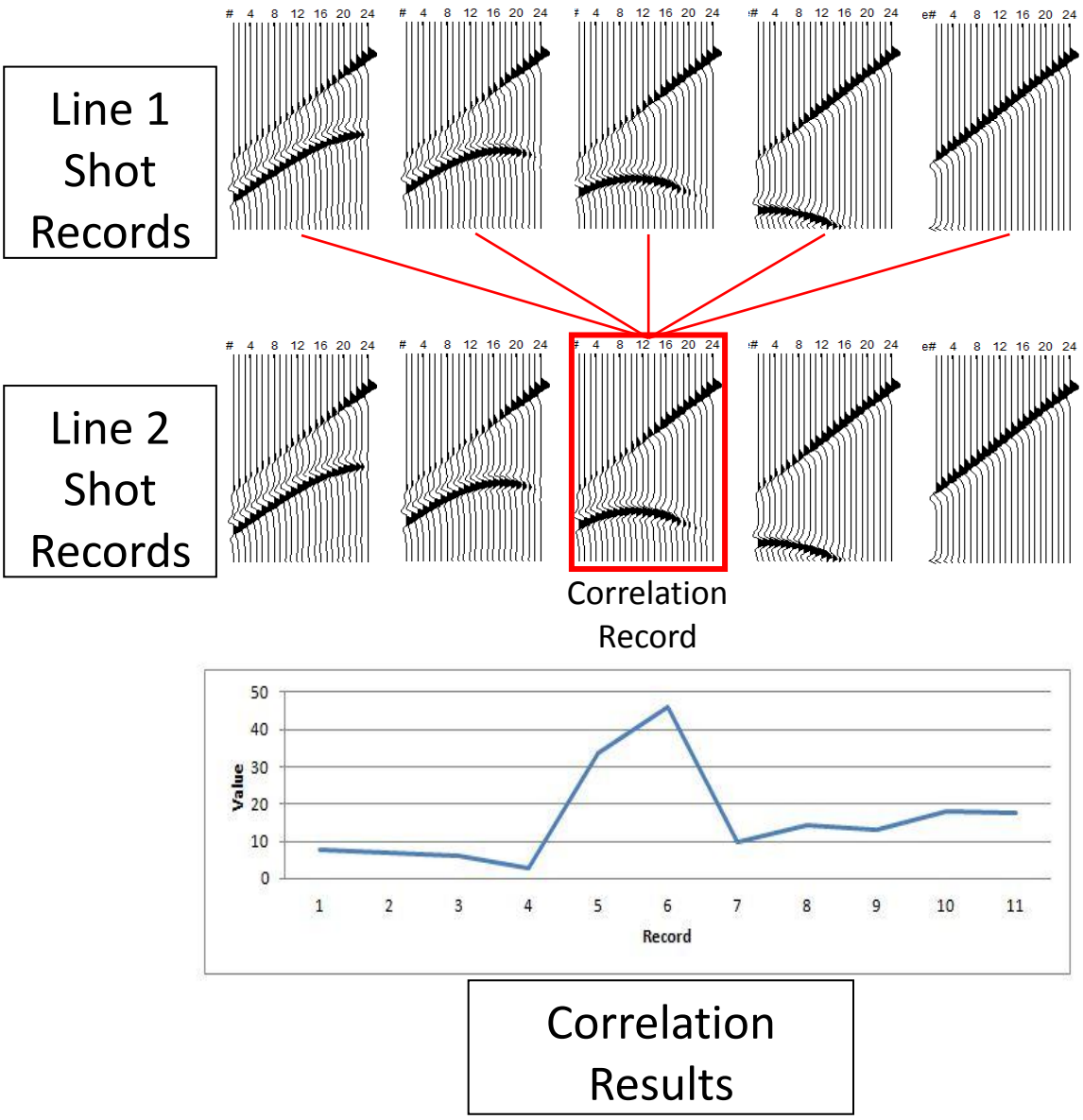

Figure 39: Theoretical example of crosscorrelation results for shot records from two seismic lines. Synthetic shot records with different offsets to the tunnel produced using a one layer synthetic model. The chart on the bottom represents the correlation coefficient calculated by correlating the selected shot record from Line 2 to the shot records from Line 1. Shot records with the same offset to the tunnel will produce larger correlation coefficients.

This idea of quantifying the similarities and differences between shot gather pairs was tested using an image similarity calculation instead of applying correlation. The samples (x,t) that make up a shot gather were treated as a matrix and the distance between the matrices were calculated. The equation used, Equation 9, is called the Manhattan Distance Equation where smaller distances (***d***) indicate more similar matrices (Sammut and Webb, 2011). This equation sums the absolute differences between samples in the two shot gathers that have the same receiver location and time assuming the source offset is the same and all receivers are recording. For this application, the matrices ***A*** and ***B*** are shot records where ***a*** and **b** are sample values at sample number (***i***) and trace number (***j***)(Equation 7).

$$d(A,B) = \sum_{i=1}^{n}\sum_{j=1}^{n}\left|a_{ij} - b_{ij}\right| \tag{9}$$

$$A = (a_{ij}) \qquad B = (b_{ij}) \tag{10}$$

Shot gathers with the smallest calculated differences should theoretically have the same source-scatter offset. Synthetic data (Figure 31) were used confirm this and to develop and test an algorithm for determining the proper shift using 'image' similarities. Because of the simplicity of the model only shot gathers with diffractions corresponding to the tunnel were used to perform a quick assessment of the potential feasibility of this method. The Manhattan Distance was calculated using shot record 1007 as matrix ***A*** and substituting shot records 1000-1015 as matrix ***B.*** The distance value for the shot record with the same tunnel offset, shot record 1007, should have the smallest value (Figure 40). In this case, the value is zero because the shot records are identical due to the nature of the model (Figure 30). Also, shots that have shot-tunnel offsets closest to, but not identical to matrix ***A***, shot record 1006 and 1008, should have the next smallest distance value. This is confirmed by the calculated distance values (Figure 40).

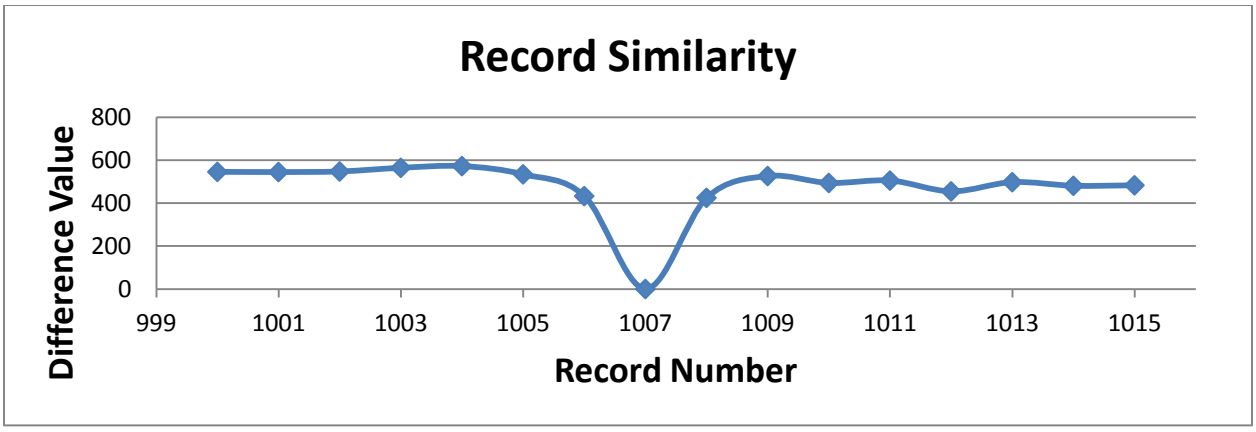

Figure 40: calculated distance values vs. record number for synthetic shot records (Figure 29)

These calculations were done to determine differences between just one selected shot record (Shot Record 1007) and fifteen other shot records. For this method to be operational, calculations would need to be done using each shot record collected at a unique shot-tunnel offset as matrix A. Computationally this method may not be feasible in the real world data case when hundreds of shot records are recorded at unique shot-tunnel offsets. Instead of determining distance values for one shot record at a time, determining distance values for each shot record from an entire line was tested several times using different offset shifts. The idea behind this is that distance values for shot records that have the appropriate offset shift applied will be lower than distance values for shot records that have the wrong shift applied. The potential of this method is demonstrated using synthetic shot records 1000-1015 on Line 1 and shifted shot records 1001-1015 on Line 2 (Figure 41). In this case, the appropriate shift of zero stations would result in distance values of 0. The distance values for the line with the shift that is closest to the appropriate shift are generally smaller than lines with other shifts applied. This signifies that this may be a feasible method that requires less computational time.

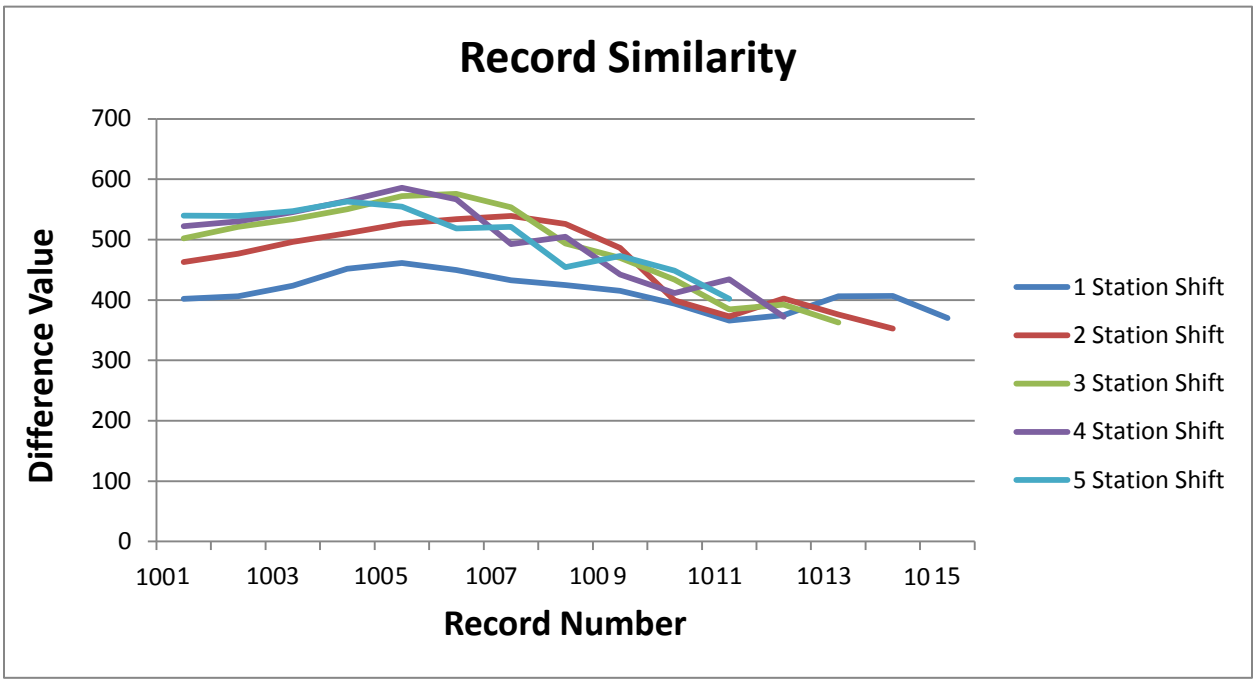

Figure 41: calculated distance values vs. record number for synthetic shot records (Figure 29) with different applied offset shifts

This image similarity algorithm was applied to Line 9 and Line 10 from the JTTR 2011 dataset (see chapter 4). No pre-processing was done to the data. Different shifts were applied to Line 10 and distance values were calculated using Line 10 shot records as matrix ***A*** and Line 9 shot records as matrix ***B*** (Figure 42). Line 9 and 10 shot records were substituted into matrix ***A*** and ***B*** based on the sequence of the input file. For example, the first distance value calculated used the first shot record from the Line 10 file and the first shot record from the Line 9 file. The resulting values do not show the expected trend of the line with the appropriate shift having generally smaller values than the other lines (Figure 39).

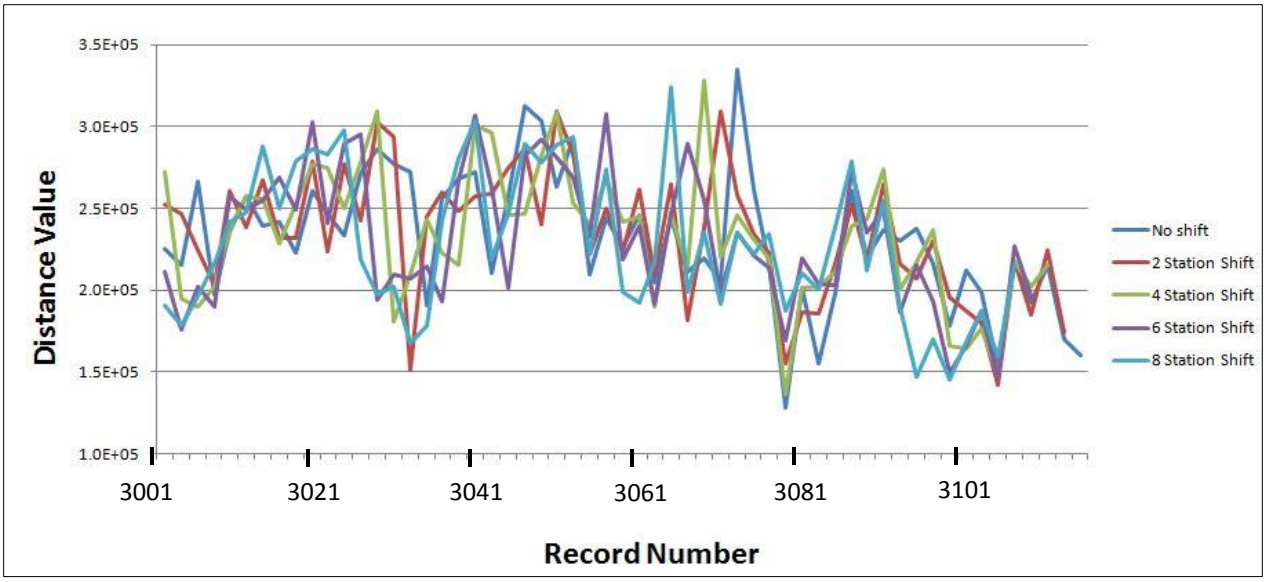

Figure 42: Calculated distance values vs. record number for Line 9 and 10 with different applied offset shifts

These results indicate what others have observed that the real data world case is more complex and methods proven to work with synthetic data may not work with real data sets. As of now image similarity methods using Manhattan Distance values do not appear to be feasible methods for determining the appropriate offset shift for parallel-line beamsteering. There are more robust matrix equations that could be used to calculate matrix similarity, which can be tested. Also, other disciplines have developed more robust methods that can be modified to determine shot record similarities. Image similarity methods such as facial recognition algorithms may be another route to pursue in the future.

Another method for future investigation is a data driven method using 2D crosscorrelation to determine the optimal spatial shift. 2D crosscorrelation is a matrix operation that uses different alignment configuration shifts similar to applying different lag times to a 1D signal. Correlation calculations are applied to each pair of elements in the matrices and the sum of the values is assigned to the alignment center location (Figure 43).

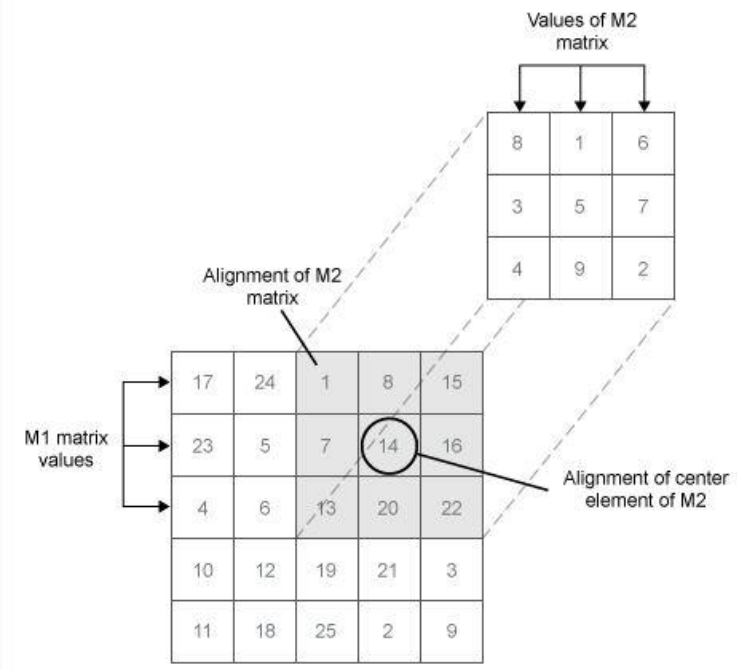

Figure 43: Depiction of 2D correlation applied to two matrices. The center of matrix 2 (M2) is aligned with matrix 1 (M1) at different positions. Aligned elements are correlated and their coefficients are summed and assigned to the alignment of the center of M2. (Image retrieved from http://www.mathworks.com/help/signal/ref/xcorr2.html

2D crosscorrelation could be applied to the final diffraction imaging and BASW results to determine the optimal spatial shift. The first step in a potential algorithm would be to select a subsection of samples (2D image) from the final diffraction image or BASW image containing a tunnel signature candidate for one line (Figure 44). The correlation coefficient calculated between aligned samples in the 2D image and the second line's diffraction image or BASW image would be assigned to the alignment center of the 2D image for every unique shift in space and time (Figure 45). The difference in the receiver location corresponding to the maximum correlation coefficient and the receiver location corresponding to the center of the 2D image should correspond to the optimal spatial shift.

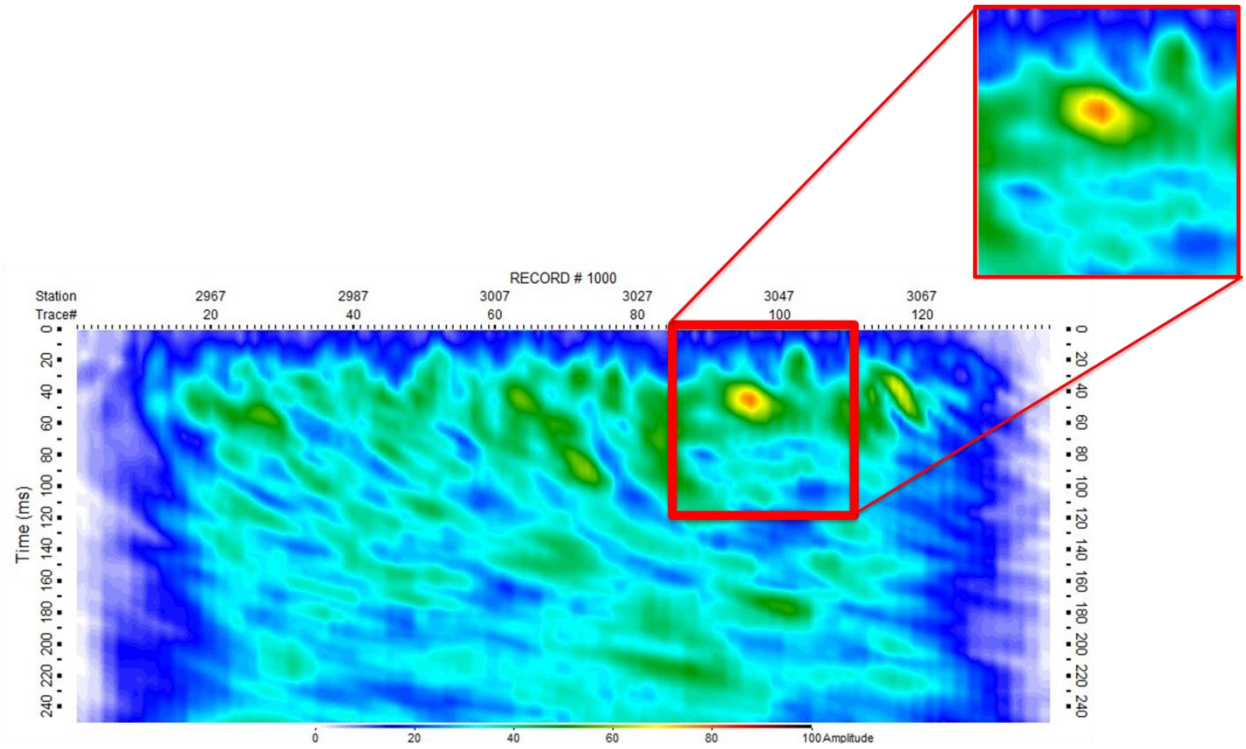

Figure 44: A small subsection of samples that comprise the final diffraction image are extracted as a 2D image to use for correlation.

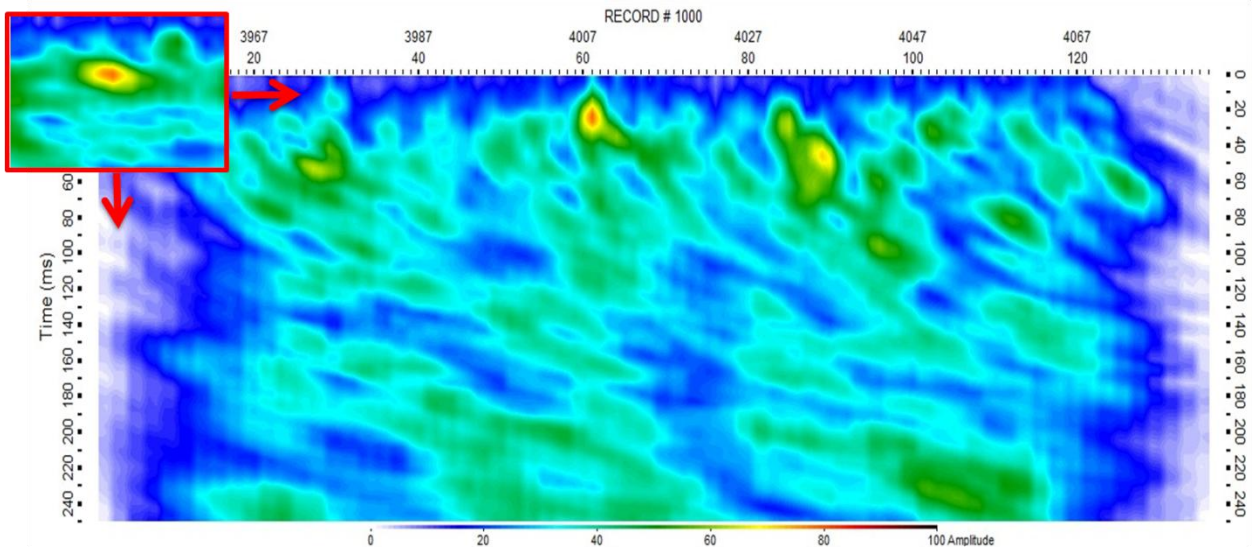

Figure 45: The 2D image is shifted in time and space with respect to a second diffraction image. Aligned samples are correlated and the value of the summed correlation coefficients are assigned to the center location of the 2D image.

5.5 Processing Flow

This section outlines the processing flow empirically developed to be the most feasible to enhance scattered signal from a tunnel and attenuate other scatter events without knowledge of the tunnel location. The processing flow for applying parallel beamsteering to BASW includes the standard BASW processing outlined by Ivanov et al. (2003) (Figure 46). A broad f-k filter is applied to vertically stacked data to attenuate high amplitude surface wave direct arrivals and other forward propagating energy (Zeng et al., 2009). Dynamic linear moveout (DLMO) corrections are applied to each shot record to flatten any remaining forward propagating energy. The *fk*-filtered and DLMO corrected data are resorted into the common receiver domain and different shifts are applied to each line by cutting traces from the resulting common receiver gather (BASW image). BASW images for both lines are vertically stacked after applying each shift. These final beamsteered BASW images are analyzed to determine the optimal spatial shift.

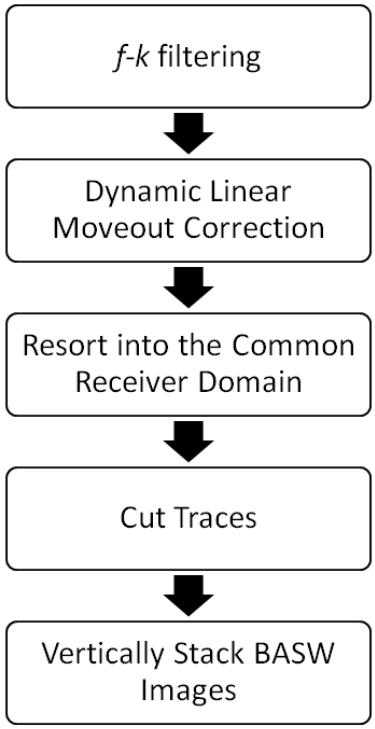

Figure 46: Parallel-line beamsteering BASW processing flow

Currently the only operational method for determining the optimal spatial shift is analyzing the BASW produced after applying a range of shifts. The optimal spatial shift is applied to pre-processed shot records before applying the diffraction imaging algorithm developed by Walters et. al (2007) (Figure 47). The optimal spatial shift is applied by cutting shot records from the appropriate line (Figure 25). If the appropriate optimal spatial shift is not a multiple of the shot spacing, then the two closest spatial shifts that are multiples of the shot spacing are applied and results are later compared during interpretation.

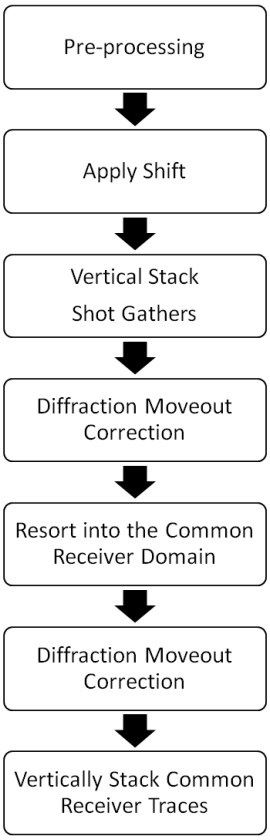

Figure 47: Parallel-line beamsteering diffraction imaging processing flow

6. Feasibility Test Results and Discussion

Parallel-line beamsteering was applied to the JTTR 2011 data set to test the feasibility of the method using the processing flow described in Section 5.1. This chapter includes diffraction imaging and BASW imaging results enhanced by beamsteering. Currently interpretation of possible tunnel signature candidates using diffraction imaging and BASW results from seismic lines collected parallel to each other assumes the tunnel crosses nearly perpendicular to the two lines. Under this assumption the amplitude anomaly or backscatter event associated with the tunnel should be located at approximately the same receiver location and depth on each line. For this feasibility test tunnel signature candidates were identified on the standard diffraction imaging and BASW results for each set of parallel lines using these spatial matching criteria. The relative seismic signal values (Section 5.1) were calculated for these tunnel signature candidates. These values were compared to the relative seismic signal values calculated for the anomaly or backscatter event at the same receiver location and depth on the parallel-line beamsteering results. Theoretically, anomalies and backscatter events that increase in relative seismic signal value are a result of constructive addition and are good tunnel signature candidates.

6.1 Lines 3 and 4

6.1.1 Diffraction Imaging

Standard diffraction imaging processing (Figure 8) was applied to Line 3 and 4 data to produce diffraction images to compare to the beamsteered enhanced diffraction image generated using data from the two lines (Figure 48). High amplitude anomalies in the beamsteered diffraction image (Figure 48C) should correspond to point scatter events constructively added during stacking or alternately events that were too great in amplitude to be successfully attenuated through stacking.

Based on the spatial matching criteria several amplitude anomalies were identified and relative seismic signal values were calculated. The results obtained by using the spatial matching criteria with

standard diffraction imaging interpretation without the use of parallel-line beamsteering resulted in four good tunnel signature candidates.

After applying parallel-line beamsteering two of the four candidates were ruled out because of attenuation suggested by the decrease in their relative seismic signal values and a new candidate became identifiable by its increase relative seismic value. One high amplitude anomaly similar on both lines is a 7.5 dB anomaly located at station 991 on Line 3 and a 6.9 dB anomaly located at station 1990 on Line 4 (Figure 48A and 48B). In the final beamsteered enhanced diffraction image this event is significantly attenuated and its relative seismic signal value is 5.1 dB at receiver location 991 (Figure 48C). This attenuation implies that the heterogeneity associated with this amplitude anomaly does not cross both lines causing attenuation of scattered signal due to differences in arrival time. Another high amplitude event common to both lines was also successfully attenuated after stacking. Before parallel-line stacking this event has a value of 7.0 dB at receiver station 1014 on Line 3 and a value of 6.0 dB at receiver station 2014 on Line 4 (Figure 48A and 45B). This anomaly has a value of 4.4 dB at receiver location 1014 on the beamsteered enhanced diffraction image (Figure 48C).

Using the spatial matching approach lower amplitude anomalies were also evaluated. A low amplitude anomaly with a value of 5.3 dB at 1982 on Line 4 has location and depth similar to an anomaly with a value of 6.9 dB at 982 on Line 3(Figure 48A and 48B). This event was constructively stacked and has a value of 7.2 dB on the beamsteered enhanced diffraction image (Figure 48C). Another low amplitude anomaly with a value of 6.7 db at receiver station 973 on Line 3 and a value of 5.4 dB at receiver station 1973 on Line 4 was constructively stacked (Figure 48A and 48B). Coherent stacking is evident from the increase in the relative seismic signal value of the anomaly to 6.8 dB at receiver location 973 on the beamsteered enhanced diffraction image (Figure 48C).

The actual center of the tunnel with respect to Lines 3 and 4, as measured on site with GPS, is located at station 1019/2019. The amplitude anomaly corresponding to the tunnel is located at receiver

station 1018 on Line 3 and 2018 on Line 4 (Figure 48A and 48B). There is a high amplitude anomaly with a value of 7.0 dB at receiver station 1018 on the beamsteered enhanced diffraction image. This anomaly was not assessed based on the spatial matching criteria because the amplitude of the anomaly at station 1018 on Line 3 is only 3.4 dB and distinguishing it from background signal is difficult. However, it does coherently stack with a high amplitude anomaly with a value of 6.3 dB at receiver station 2018 on Line 4.

This suggests that all high amplitude anomalies on the beamsteered enhanced diffraction image should be investigated in order to properly identify all possible tunnel locations. This result also highlights the fact that using standard interpretation based on spatial matching criteria for diffraction imaging results from parallel lines may not identify anomalies associated with the tunnel. In this case, the amplitude anomaly corresponding to the actual lateral location of the tunnel had an increase in relative seismic signal value of 0.7 dB after parallel-line stacking. This was more than twice the amount by which the other two candidates' relative seismic signal values increased by.

6.1.2 Backscatter Analysis of Surface Waves

Spatial matching criteria were applied to assess backscatter from heterogeneities that were common to both lines. Based on these criteria one high amplitude backscatter event was identified with a value of 14.2 dB at receiver location 1018 on Line 3 and 14.1 dB at receiver location 2018 on Line4 (Figure 49A and 49B). The value of the high amplitude backscatter event is14.2 dB at receiver location 1018 on the beamsteered enhanced BASW image (Figure 49C). There is an increase of less than 0.1 dB which is inconclusive evidence to suggest coherent stacking of this signal (Figure 49C).

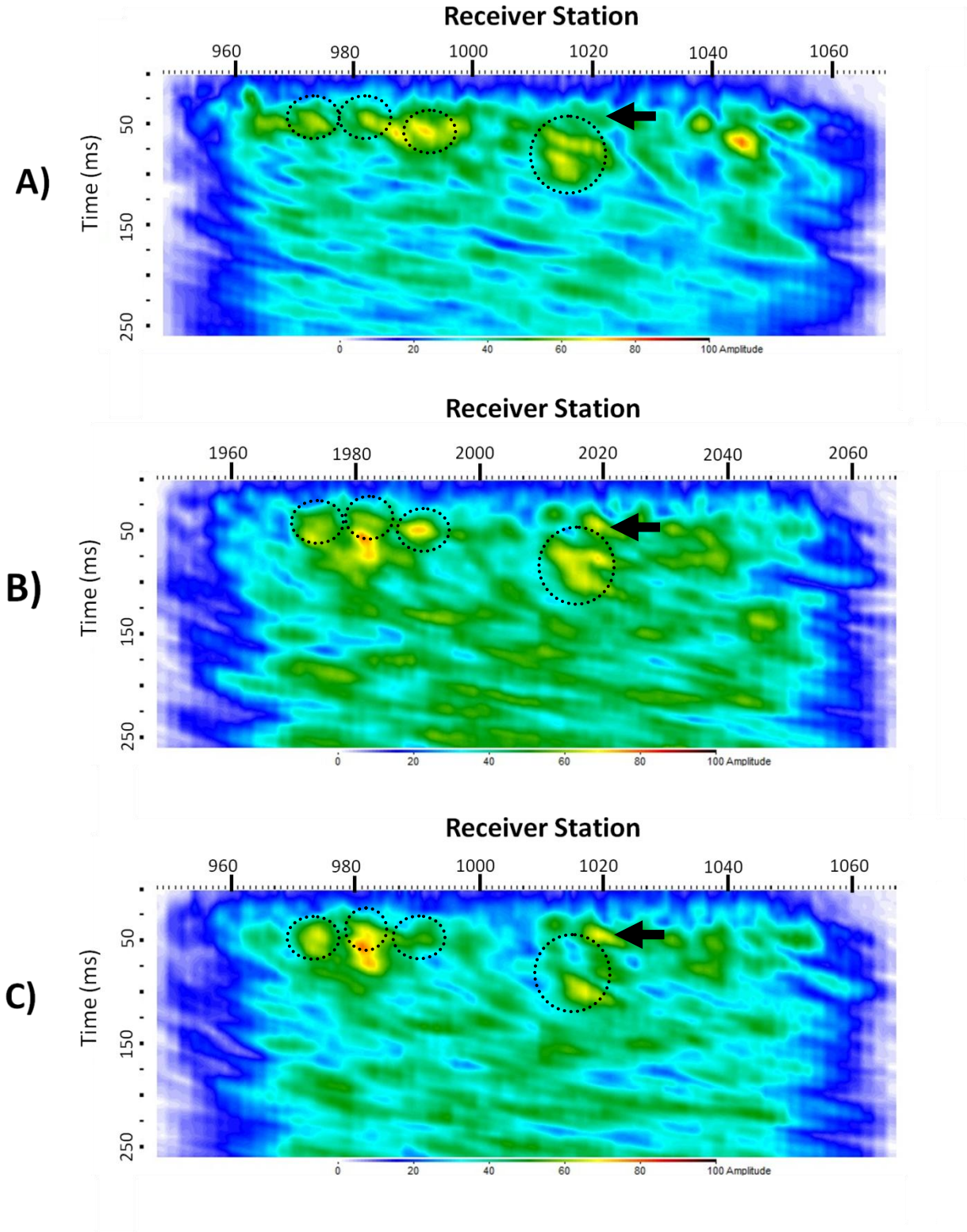

Figure 48: diffraction image **A)** Line 3 **B)** Line 4 **C)** after stacking Line 3 and 4 pre-processed raw data, black arrow indicates signal associated with the tunnel, circles highlight amplitude anomalies common to both lines

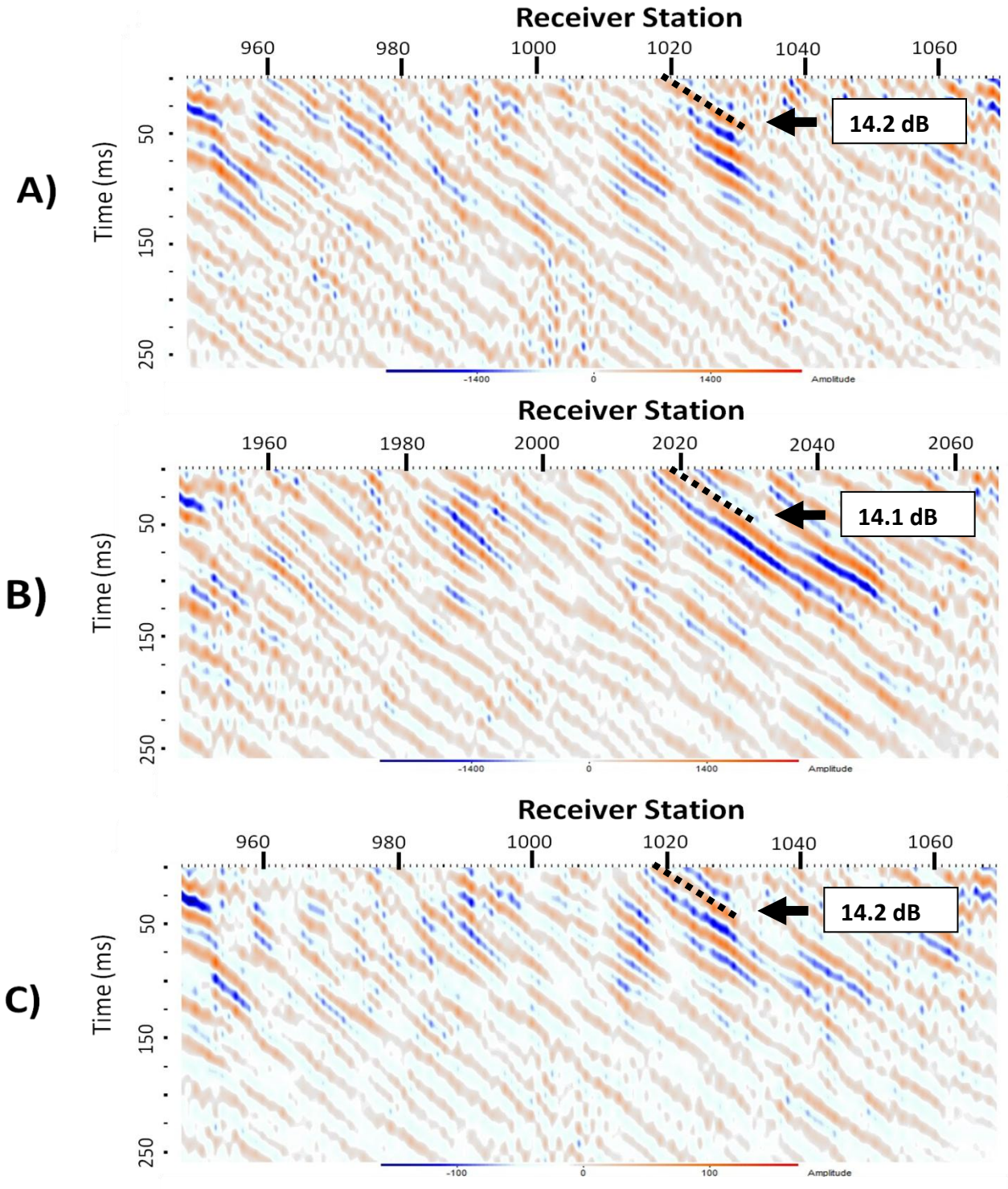

Figure 49: BASW image **A)** Line 3 **B)** Line 4 **C)** after stacking Line 3 and 4 BASW images , black arrow indicates the signal associated with the tunnel and the calculated relative seismic signal value is listed, the dotted black line indicates the first arrival time of backscattered energy

6.2 Lines 5 and 6

6.2.1 Diffraction Imaging

Using spatial matching criteria, amplitude anomalies were analyzed to determine if they were good tunnel signature candidates. The results obtained by using the spatial matching criteria with standard diffraction imaging interpretation, without the use of parallel-line beamsteering, would result in three good tunnel signature candidates. After applying parallel-line beamsteering two of the three candidates were ruled out because of attenuation, suggested by the decrease in their relative seismic signal values, and a new candidate became identifiable by its increase relative seismic value.

Two low amplitude anomalies common to both lines were identified. The first low amplitude anomaly identified has a value of 5.6 dB at receiver station 2980 on Line 5 and a value of 6.4 dB at receiver station 3980 on Line 6 (Figure 50A and 50B). The relative seismic signal value of the anomaly calculated from the beamsteered enhanced diffraction image at receiver station 2980 is 5.7 dB (Figure 50C). This value suggests attenuation of signal associated with this anomaly after applying parallel-line stacking. The second low amplitude anomaly common to both lines has a value of 8.1 dB at receiver station 2971 on Line 5 and a value of 5.0 dB at receiver station 3971 on Line 6 (Figure 50A and 50B). The relative seismic signal value of the anomaly calculated from the beamsteered enhanced diffraction image is 7.1 dB (Figure 50C). This value suggests attenuation of signal associated with this anomaly after applying parallel-line stacking.

One high amplitude anomaly was identified as being common to both at approximately 80 ms with a value of 7.5 dB at receiver location 3026 on Line 5 7.9 dB 4026 on Line 6 (Figure 50A and 50B). This event is coherently stacked and has a value of 9.2 dB at receiver location 3026 on the beamsteered enhanced diffraction image making it a good candidate for a possible tunnel (Figure 50C). Based on this analysis the anomaly at receiver location 3026/4026 is the only good tunnel signature candidate. The

center of the tunnel corresponds to receiver location 3027/4027 according to GPS data. The high amplitude anomaly with a relative seismic signal value of 9.2 dB at receiver location 3026 on the beamsteered enhanced diffraction image 4026 is at the approximate lateral location of the tunnel (Figure 50C). The depth corresponding to this anomaly was calculated using the travel-time equation, Equation 3, derived in Section 3.1. The depth of a tunnel located at 3026/4026 based on the travel-time of the signal associated with this anomaly is 25.4 m. This value is the distance to the vertical shaft relative to Line 5. The 25.4 m anomaly is likely the signature of the vertical shaft and not the horizontal tunnel beneath the lines.

There is an anomaly at location 3026 on the beamsteered enhanced diffraction image at approximately 44 ms (Figure 50C). The depth calculated for this anomaly is 12 m, which is closer to the actual depth of the tunnel at 9.1 m. The low amplitude nature of this anomaly made it hard to distinguish from background signal on Line 5 and 6 diffraction images. The relative seismic signal value of this anomaly is 4.2 dB at receiver station 3025 on Line 5 and 4.5 dB at receiver station 4026 on Line 6 (Figure 50A and 50B). The relative seismic signal value of this anomaly at receiver station 3026 on the beamsteered enhance diffraction image is 7.3 dB (Figure 50). This value implies that signal associated with this anomaly was coherently added.

Standard diffraction imaging interpretation using the spatial matching criteria did not lead to proper identification of the anomaly associated with the actual tunnel signature similar to the analysis of Line 3 and 4 anomalies. This confirms the idea that all high amplitude anomalies on the beamsteered enhanced diffraction image should be investigated in order to properly identify all possible tunnel locations. This also emphasized the need for a signal enhancing method such as parallel-line beamsteering to reduce the dependency on skilled interpretation. Again, the anomaly associated with the actual tunnel lateral location and depth had an increase in relative seismic signal (2.8 dB) that is

more twice as much as the increase in relative seismic value of the other tunnel signature candidate identified (1.3 dB).

6.2.2 Backscatter Analysis of Surface Waves

Spatial matching criteria were applied to assess backscatter from heterogeneities that were common to both lines. Based on these criteria one high amplitude backscatter event was identified with a value of 13.8 dB at receiver location 3026 on Line 5 and 12.3 dB at receiver location 4026 on Line 6 (Figure 51A and 51B). The value of the high amplitude backscatter event of 14.0 dB at receiver location 3026 on the beamsteered enhanced BASW image, which is an increase of 0.2 dB, implies coherent stacking of this signal (Figure 51C). However, there is no way to distinguish what backscattered signal is associated with the vertical shaft and what backscattered signal is associated with the horizontal tunnel.

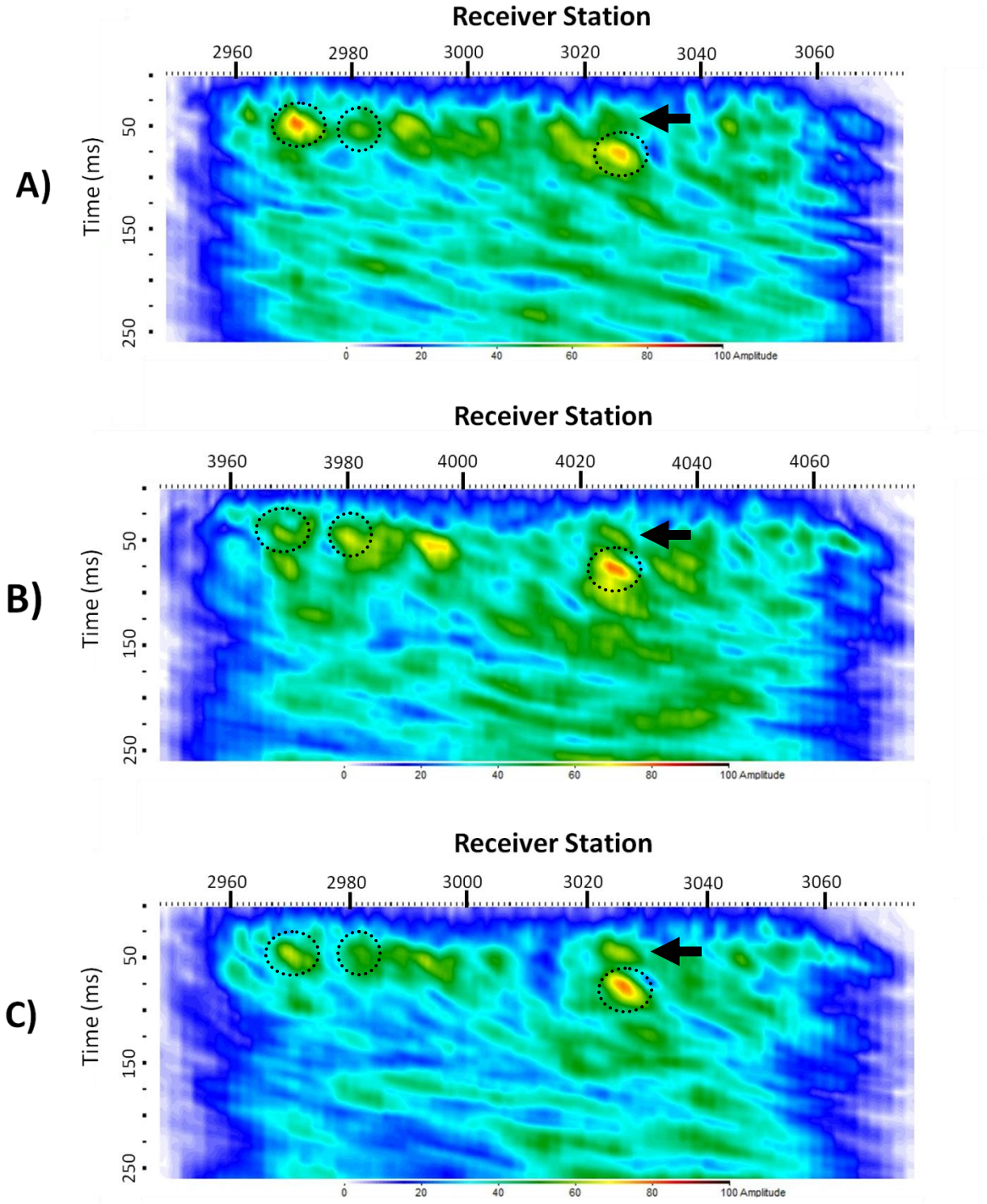

Figure 50: diffraction image **A)** Line 5 **B)** Line 6 **C)** stacking Line 5 and 6 pre-processed raw data, black arrow indicates signal associated with the tunnel, circles highlight amplitude anomalies common to both lines

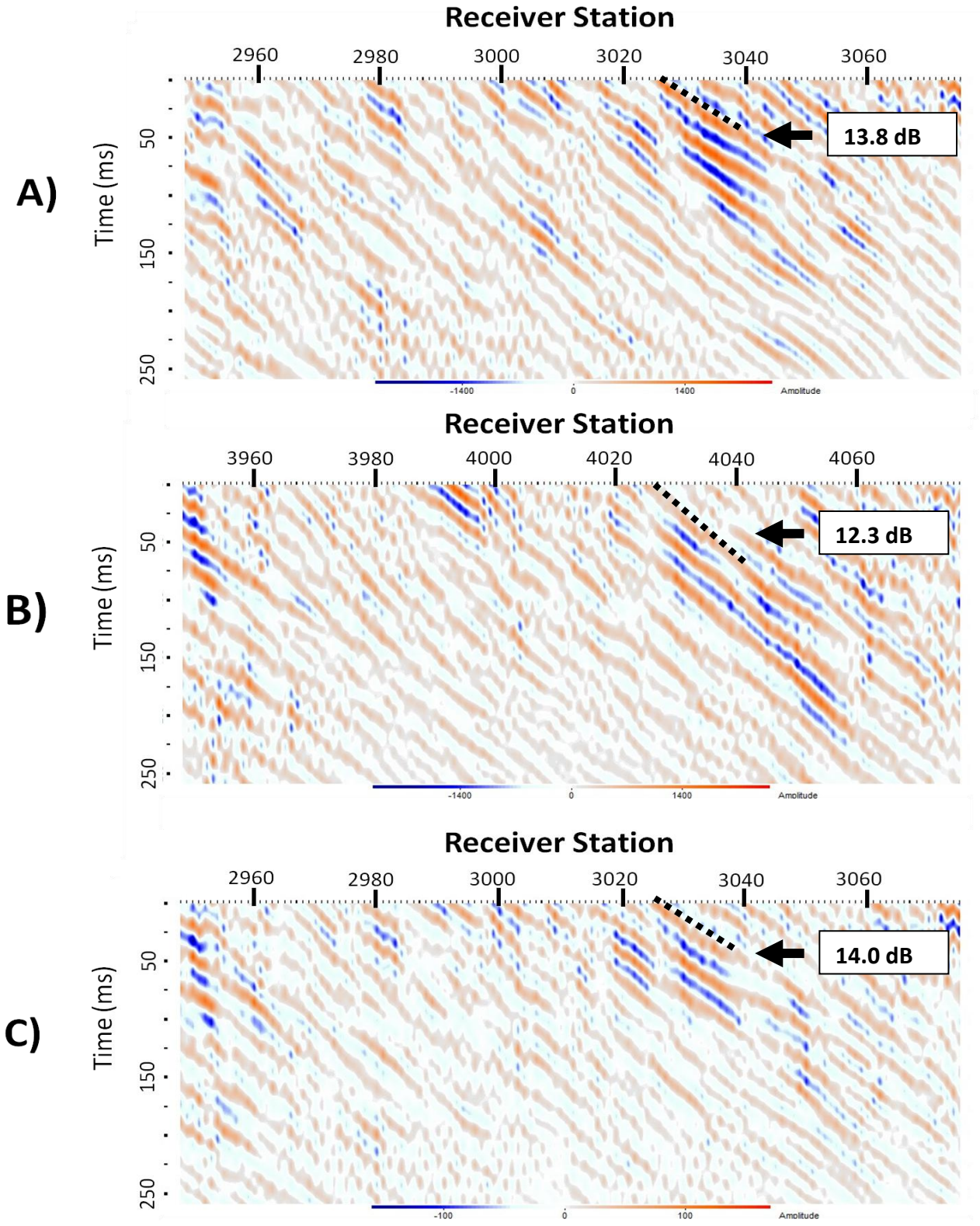

Figure 51: BASW image **A)** Line 5 **B)** Line 6 **C)** after stacking Line 5 and 6 BASW images , black arrow indicates the signal associated with the tunnel and the calculated relative seismic signal value is listed, the dotted black line indicates the first arrival time of backscattered energy

6.3 Lines 7 and 8

6.3.1 Diffraction Imaging

Three amplitude anomalies were identified fulfilling the spatial matching criteria for Line 7 and 8. After applying parallel-line beamsteering one of these three anomalies was ruled out as a good candidate because of signal attenuation. One of these anomalies has a relative seismic signal value of 6.4 dB at receiver location 997 on Line 7 and a value of 10.0 dB at receiver location 1998 on Line 8 (Figure 52A and 52B). The relative seismic signal value of 6.1dB at receiver location 998 on the beamsteered enhanced diffraction image implies attenuation of the signal associated with this anomaly after applying parallel-line stacking (Figure 52C). The second anomaly identified based on the spatial matching criteria is located at approximately 75 ms at receiver station 1026/2026. This anomaly has a relative seismic value of and 6.5 dB at receiver station 1026 on Line 7 and a value of 4.7 dB at receiver station 2026 on Line 8 (Figure 52A and 52B). The relative seismic signal value of 7.7 dB at receiver station 1026 on the beamsteered enhanced diffraction image suggests the signal associated with this anomaly was coherently stacked during parallel-line stacking (Figure 52C). This makes the anomaly at 1026/2026 is a good tunnel signal candidate. Another anomaly nearby at 45 ms has a relative seismic signal value of 5.4 dB at receiver station 1027 on Line 7 and a value of 5.6 dB at receiver station 2027 on Line 8 (Figure 52A and 52B). The relative seismic signal calculated for this anomaly at receiver location 1027 on the beamsteered enhanced diffraction image is 8.0 dB (Figure 52C). This increase in the relative seismic signal suggests the signal associated with this anomaly was coherently stacked making it a good tunnel signature candidate.

The lateral location of the center of the tunnel is corresponds to receiver station 1027/2027 according to GPS coordinates. The two good tunnel signature candidates are located at approximately

the correct lateral location. Similar to Line 5 and 6 the depth corresponding to the shallower anomaly is similar to the depth of the tunnel and the depth of the deeper anomaly is similar to the distance between the vertical shaft and Line 7. The approximate depth associated with the shallower anomaly is 10.8 m. The increase in relative seismic signal value of the shallower anomaly is 2.4 dB, which is almost double what the increase in relative seismic signal value of the deeper anomaly (1.2 dB).

6.3.2 Backscatter Analysis of Surface Waves

Spatial matching criteria were applied to assess backscatter from heterogeneities that were common to both lines. Based on these criteria one backscatter event common to both lines was identified at receiver station 998 on Line 7 and 1997 on Line 8 with relative seismic signal values of 10.8 dB and 14.5 dB respectively (Figure 53A and 53B). After applying parallel-line stacking the relative seismic signal value of this event is 14.0 dB suggesting slight attenuation of the backscattered signal at this location. Another backscatter event common to both lines was identified with a value of 13.9 dB at receiver location 1027 on Line 7 and 13.3 dB at receiver location 2027 on Line8 (Figure 53A and 53B). The value of the high amplitude backscatter event of 15.8 dB at receiver location 3027 on the beamsteered enhanced BASW image this 1.9 dB increase implies coherent stacking of this signal (Figure 53C). There is no way to distinguish what backscattered signal is associated with the vertical shaft and what backscattered signal is associated with the horizontal tunnel.

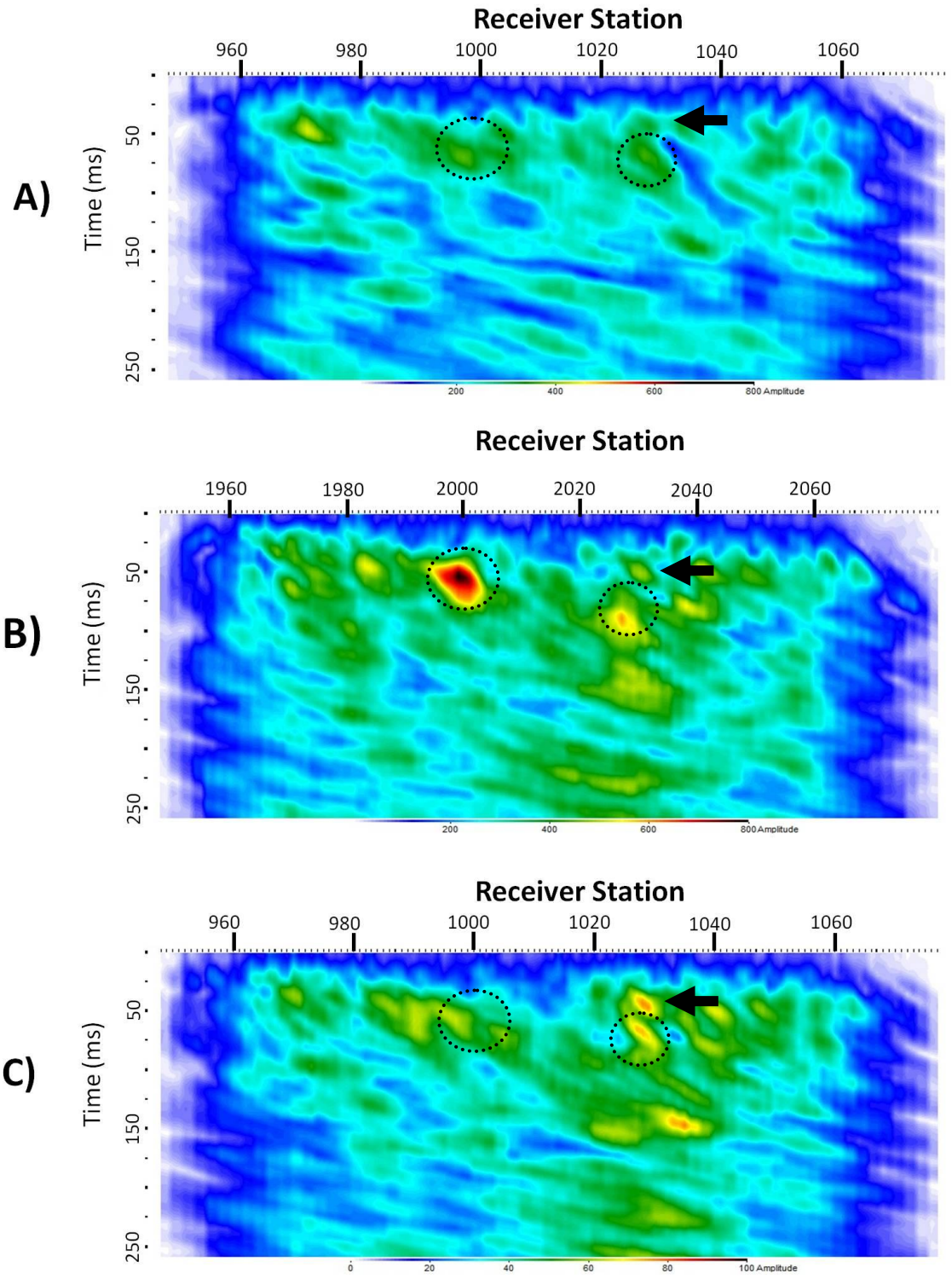

Figure 52: diffraction image **A)** Line 7 **B)** Line8 **C)** after stacking Line 7 and 8 pre-processed raw data, black arrow indicates signal associated with the tunnel, circles highlight amplitude anomalies common to both lines

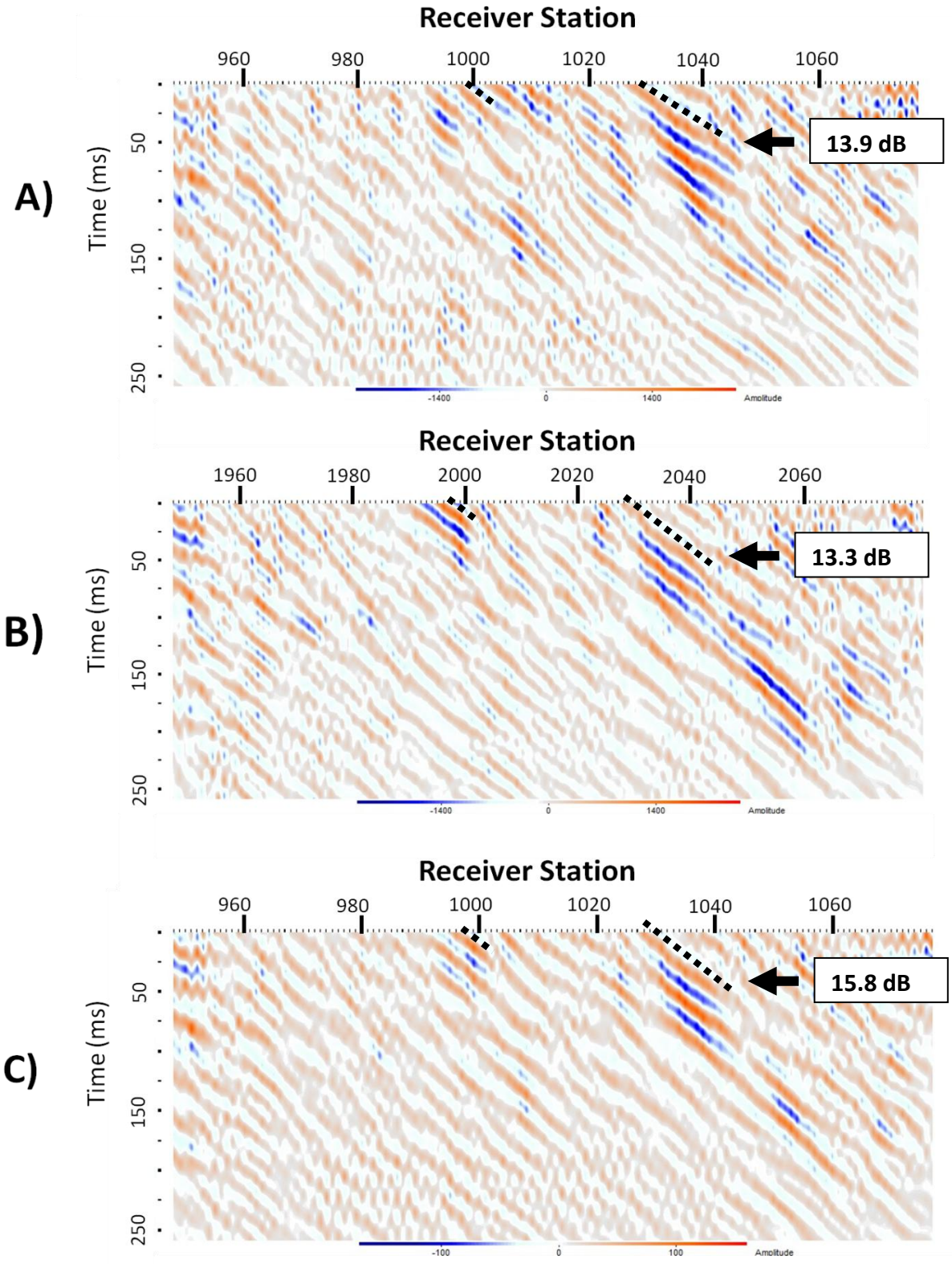

Figure 53: BASW image **A)** Line 7 **B)** Line 8 **C)** after stacking Line 7 and 8 BASW images , black arrow indicates the signal associated with the tunnel and the calculated relative seismic signal value is listed, the dotted black line indicates the first arrival time of backscattered energy

6.4 Lines 9 and 10

6.4.1 Diffraction Imaging

Using spatial matching criteria amplitude anomalies were analyzed to determine if they were good tunnel signature candidates assuming the lines were collected perpendicular to the long axis of the tunnel. Two amplitude anomalies were identified as being common to both lines. After analyzing parallel-line beamsteering results both anomalies were determined to be poor tunnel signature candidates.

One anomaly identified has a relative seismic signal value of 6.1 dB at receiver station 2974 on Line 10 and a value of 7.2 dB at receiver station 3974 on Line 10 (Figure 54A and 54B). After determining the optimal spatial shift and determining these lines are not perpendicular to the tunnel, this signal associated with this anomaly appears to be attenuated during parallel-line stacking based on the decrease in relative seismic signal. The relative seismic signal value for this anomaly is 4.1 dB at receiver location 2972 on the beamsteered enhanced diffraction image (Figure 54C). The second anomaly common to both lines has a relative seismic signal of 4.8 dB at receiver station 3049 on Line 9 and a value of 5.7 dB at receiver station 4049 on Line 10 (Figure 54A and 54B). After applying the optimal spatial shift this anomaly has a relative seismic signal of 4.5 dB at receiver station 3049 on the beamsteered enhanced diffraction image. Applying the optimal spatial shift also attenuates signal associated with this anomaly.

The anomaly associated with the tunnel is located at different receiver stations on each line because of the non-perpendicular orientation of the tunnels with respect to the seismic line. Therefore, applying the spatial matching criteria did not facilitate proper identification of the amplitude anomaly associated with the tunnel. On Line 9 the anomaly associated with tunnel is located at receiver location

3030 and has a relative seismic signal value of 4.9 dB (Figure 54A). On Line 10 the anomaly associated with the tunnel is located at receiver location 4036 and has a relative seismic signal value of 8.3 dB (Figure 54B). A spatial shift of 6 receiver stations (7.2 m) was applied to Line 10 before parallel-line stacking. The resulting relative seismic signal value of the coherently stacked anomaly is 8.3 dB at receiver location 3030 on the beamsteered enhanced diffraction image (Figure 54C). The relative seismic signal value of this anomaly increased by less than 0.1 dB after applying the spatial shift and parallel-line stacking. This value may have been greater if the optimal spatial shift of 6.0 m could have been applied to the data. The approximate depth associated with the anomaly is 11.7 m. The actual center of the tunnel located under receiver station 3031 on Line 9 and receiver station 3037 on Line 10. Using the spatial shift applied to diffraction imaging and the line offset of 12 m in Equation 5, the angle of the tunnel with respect to the seismic lines was calculated as 59^{o}. Estimates based on GPS coordinates of seismic stations relative to the tunnel location on site indicate it is at a 60^{o} angle to Lines 9 and 10.

6.4.2 Backscatter Analysis of Surface Waves

Spatial matching criteria were applied to assess backscatter from heterogeneities that were common to both lines. Based on these criteria two backscatter events were identified. One backscatter event is located at receiver location 3007 on Line 9 and 4006 on Line 10 and has relative seismic signal values of 13.5 dB and 12.5 dB respectively (Figure 55A and 55B). The optimal spatial shift determined during method development (Section 5.2.1) of 5 receiver stations (6.0 m) was applied to Line 10 before stacking. The relative seismic signal value associated with this backscatter event after shifting and applying parallel-line stacking is 11.4 dB suggesting attenuation of this signal during stacking (Figure 55C). The other backscatter event common to both lines has a relative seismic signal value of 14.8 dB at receiver location 3032 on Line 9 and 13.6 dB at receiver location 4034 on Line10 (Figure 55A and 55B). The value of the high amplitude backscatter event of 15.0 dB at receiver location 3033 on the

beamsteered enhanced BASW image implies coherent stacking of this signal (Figure 55C).This coherently stacked backscatter event is a good tunnel signature candidate.

The actual center of the tunnel located under receiver station 3031 on Line 9 and receiver station 3037 on Line 10. Using the optimal spatial shift applied to BASW, the angle of the tunnel with respect to the seismic lines was calculated to be 63.4^{o}. Estimates based on GPS coordinates of seismic stations relative to the tunnel location on site indicate it is at a 60^{o} angle to Lines 9 and 10.

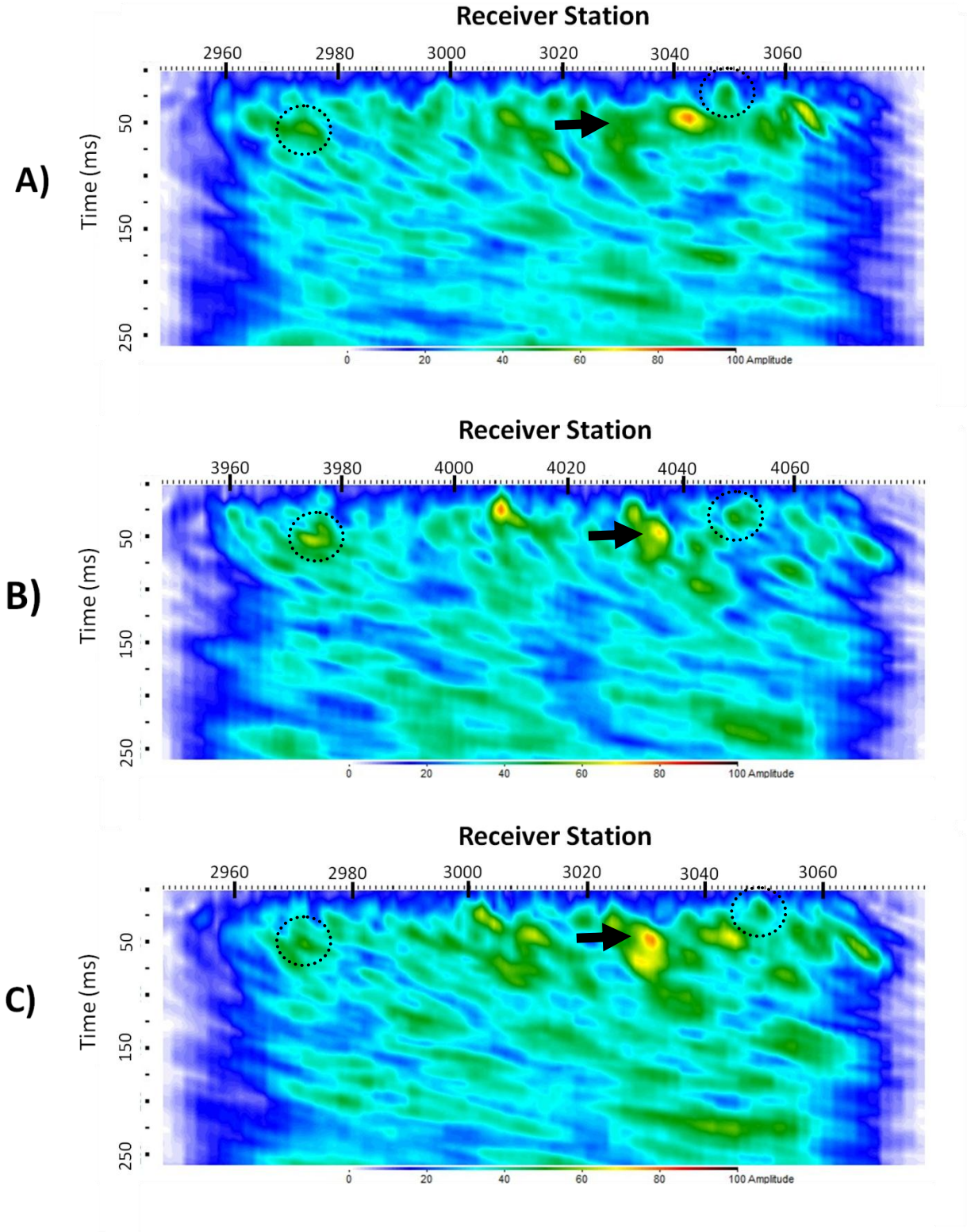

Figure 54: diffraction image **A)** Line 9 **B)** Line 10 **C)** after shifting Line 10 by six stations (7.2 m) and stacking Line 9 and 10 pre-processed raw data, black arrow indicates signal associated with the tunnel, circles highlight amplitude anomalies common to both lines

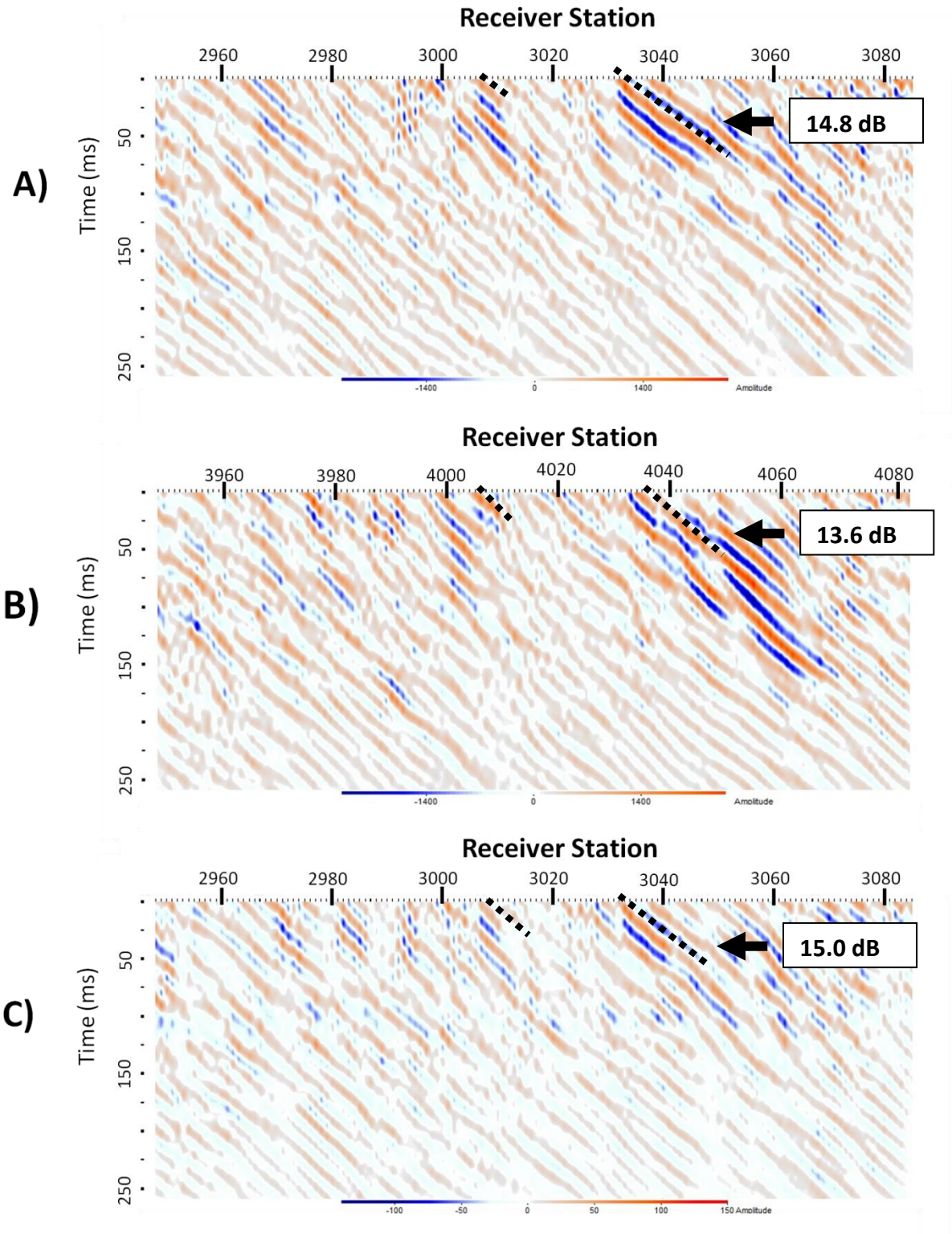

Figure 55: BASW image **A)** Line 9 **B)** Line 10 **C)** after shifting Line 10 BASW image by 6.0 m (5 stations) and stacking Line 9 and 10 BASW images , black arrow indicates the signal associated with the tunnel and the calculated relative seismic signal value is listed, the dotted black line indicates the first arrival time of backscattered energy

7. Conclusion

Parallel-line beamsteering is a new seismic processing method that utilizes consistency in recorded data from parallel seismic line to enhance signal from laterally continuous heterogeneities like tunnels that cross beneath these parallel lines and attenuate scatter from localized heterogeneities unique to each line. This method was taken from a concept and developed into a readily usable processing method. Different work flows utilizing the stack and shift aspect of established beamsteering methods applied to BASW and diffraction imaging processing steps were tested. The processing flows that best enhanced signal from a crossline tunnel through increasing the signal-to-noise ration of BASW and diffraction images were determined. These processing flows were applied to synthetic data and field data collected over a known tunnel at the JTTR. Vertically stacking pre-processed shot gathers before diffraction imaging processing and vertically stacking final BASW images produced the greatest enhancement to the tunnel signal for this field data set. Determining the correct spatial shift through analysis of BASW images for a range of horizontal shifts still requires skilled interpretation. Future work to automate the shifting process using quantitative shifting methods such as 2D correlation will decrease the need for skilled interpretation.

Applying this newly developed beamsteering analysis to diffraction imaging and BASW demonstrated the potential of this method to enhance signal from the tunnel and attenuate energy scatter associated with other near surface heterogeneities. The standard and routine processing flows were used to establish a degree of improvement using beamsteering for the data set collected at the JTTR. For three of the four field data sets the relative seismic signal value of the anomaly associated with the tunnel increased by nearly twice as much as any other event coherently stacked event. A tunnel signature candidate corresponding to the actual lateral location of the tunnel was identified on only one set of diffraction images (Lines 7 and 8) before parallel-line beamsteering was applied. Beamsteering analysis also reduced the number of possible tunnel locations interpreted from diffraction imaging

results using standard interpretation based on spatial matching criteria by up to 66% and from the BASW imaging results by up to 50%. In the case of the oblique tunnel, the optimal spatial shift between the two lines with a known offset was used to accurately determine the orientation of the tunnel.

Parallel-line beamsteering processing enhanced the signal associated with the tunnel on diffraction imaging and BASW imaging results for all four sets of parallel lines. Signal from the tunnel was coherently stacked with respect to other scattering events in the final beamsteered enhanced BASW and diffraction images allowing for distinction between scatter from the tunnel and scatter from localized heterogeneities. Results show that parallel-line beamsteering decreases the amplitude of anomalies and backscatter events not related to crossline heterogeneities through destructive stacking of signal from heterogeneities that are not common to both receiver lines. This increased signal-to-noise of the final BASW and diffraction images. Interpreting results of parallel-line beamsteering requires a less skilled interpretation.

8. References

(ONDCP), O. o. N. D. C. P., 2009, National Southwest Border Counternarcotics Strategy: Executive Office of the President of the United States.

(ONDCP), O. o. N. D. C. P., 2013, National Southwest Border Counternarcotics Strategy: Executive Office of the President of the United States.

Bjurström, H., N. Rydén, and B. Birgisson, 2014, Non-contact surface wave testing of pavements: comparing a rolling microphone array with accelerometer measurements: Smart Structures and Systems.

Boettcher, S. S., and S. Mosher, 1998, Mid-to Late Cretaceous ductile deformation and thermal evolution of the crust in the northern Dome Rock Mountains, Arizona: Journal of structural geology, **20**, 745-764.

Boettcher, S. S., S. Mosher, and R. M. Tosdal, 2002, Structural and tectonic evolution of Mesozoic basement-involved fold nappes and thrust faults in the Dome Rock Mountains, Arizona: SPECIAL PAPERS-GEOLOGICAL SOCIETY OF AMERICA, 73-98.

Bormann, P., 2013, Seismic Signals and Noise.

Dobecki, T. L., and S. B. Upchurch, 2006, Geophysical applications to detect sinkholes and ground subsidence: The Leading Edge, **25**, 336-341.

Evernden, J. F., 1969, Beam-steering of large randomly-spaced long-period arrays: Bulletin of the Seismological Society of America, **59**, 1559-1567.

Gelis, C., D. Leparoux, J. Virieux, A. Bitri, S. Operto, and G. Grandjean, 2005, Numerical Modeling of Surface Waves Over Shallow Cavities: Journal of Environmental and Engineering Geophysics, **10**, 111-121.

Gibbons, S. J., F. Ringdal, and T. Kværna, 2008, Detection and characterization of seismic phases using continuous spectral estimation on incoherent and partially coherent arrays: Geophysical Journal International, **172**, 405-421.

Grandjean, G., and D. Leparoux, 2004, The potential of seismic methods for detecting cavities and buried objects: experimentation at a test site: Journal of Applied Geophysics, **56**, 93-106.

Haupt, R. W., and K. D. Rolt, 2005, Standoff acoustic laser technique to locate buried land mines: Lincoln Laboratory Journal, **15**, 3-22.

Herman, G. C., P. A. Milligan, R. Huggins, and I. James W. Rector, Imaging shallow objects with scattered guided waves, SEG Technical Program Expanded Abstracts 1998, 825-828.

Inazaki, T., S. Kawamura, O. Tazawa, Y. Yamanaka, and N. Kano, 2005, Near-Surface Cavity Detection by High-Resolution Seismic Reflection Methods Using Short-Spacing Type Land Streamer, Symposium on the Application of Geophysics to Engineering and Environmental Problems 2005, 959-970.

Ivanov, J., R. Miller, C. Park, and N. Ryden, 2003, Seismic search for underground anomalies: Presented at the Society of Exploration Geophysicists.

Ivanov, J., C. B. Park, R. D. Miller, and J. Xia, 2005, Analyzing and Filtering Surface-Wave Energy By Muting Shot Gathers: Journal of Environmental and Engineering Geophysics, **10**, 307-322.

Keydar, S., B. Medvedev, M. Ezersky, and L. Sobolevsky, 2012, Imaging Shallow Subsurface of Dead Sea Area by Common Shot Point Stacking and Diffraction Method Using Weighted Multipath Summation (Case Study): Journal of Civil Engineering and Science, **1**, 75-79.

Knight, R. D., 2013, Physics for Scientists and Engineers: A Strategic Approach Pearson.

Korneev, V., 2009, Resonant seismic emission of subsurface objects: GEOPHYSICS, **74**, T47-T53.

Landa, E., and S. Keydar, 1998, Seismic monitoring of diffraction images for detection of local heterogeneities: GEOPHYSICS, **63**, 1093-1100.

Landa, E., V. Shtivelman, and B. Gelchinsky, 1987, A METHOD FOR DETECTION OF DIFFRACTED WAVES ON COMMON-OFFSET SECTIONS*: Geophysical Prospecting, **35**, 359-373.

McCann, D., P. Jackson, and M. Culshaw, 1987, The use of geophysical surveying methods in the detection of natural cavities and mineshafts: Quarterly Journal of Engineering Geology and Hydrogeology, **20**, 59-73.

McCowan, I., 2001, Microphone arrays: A tutorial: Queensland University, Australia, 1-38.

McDonald, E. V., G. K. Dalldorf, and S. N. Bacon, 2009, Landforms and Surface Cover of US Army Yuma Proving Ground: DTIC Document.

Meschino, S., L. Pajewski, and G. Schettini, Year, Sub-Array Processing for parameters estimate of embedded conducting cylinders: Radar Conference, 2009. EuRAD 2009. European, IEEE, 417-420.

Miller, R. D., J. M. Ivanov, T. S. Anderson, C. B. Park, M. L. Moran, and R. Ballard, 2004, Deployment and testing of wavefield imaging systems to detect underground facilities: Presented at Military Sensing Symposium Specialty Group on Battlefield Acoustic and Seismic Sensing.

Miller, R. D., O. M. Metheny, J. M. Anderson, and A. R. Wedel, 2010, Study of Unconsolidated Sediments at Joint Tunnel Test Range (JTTR) on Yuma Proving Grounds, Arizona: The University of Kansas.

Moran, M. L., and R. J. Greenfield, 1993, Radar signature of a 2.5-D tunnel: GEOPHYSICS, **58**, 1573-1587.

Moser, T. J., and C. B. Howard, 2008, Diffraction imaging in depth: Geophysical Prospecting, **56**, 627-641.

Ogah, A. J., and A. D. Chinedu, 2012, The Beam-Forming Technique for Enhancement of Noisy Seismic Refraction Data: International Journal of Geosciences, **3**.

Park, C. B., R. D. Miller, and J. Xia, 1999a, Detection of Near-Surface Voids Using Surface Wave, Symposium on the Application of Geophysics to Engineering and Environmental Problems 1999, 281-286.

Park, C. B., R. D. Miller, and J. Xia, 1999b, Multichannel analysis of surface waves: GEOPHYSICS, **64**, 800-808.

Peter, E., 1968, Diversity seismic record stacking method and system: Google Patents.

Peterie, S. L., and R. D. Miller, 2015, Near-surface scattering phenomena and implications for tunnel detection: Interpretation, **3**, SF43-SF54.

Piper, J. E., 2011, Beamforming narrowband and broadband signals.

Rex, R. L., and G. T. Roberts, 1969, Correlation, Signal Averaging, and Probability Analysis: Hewlett-Packard Journal, **21**, 2-8.

Rickards, B. T., 2011, Near-surface shear-wave velocity measurements in unlithified sediment, University of Kansas.

Riyanti, C. D., X. Campman, and G. Herman, 2005, Inversion of scattered surface waves for characterizing shallow heterogeneities, SEG Technical Program Expanded Abstracts 2005, 1053-1056.

Rost, S., and C. Thomas, 2002, Array seismology: Methods and applications: Reviews of geophysics, **40**, 1008.

Sammut, C., and G. I. Webb, 2011, Encyclopedia of Machine Learning: Springer Publishing Company, Incorporated.

Schwenk, J. T., 2013, Constrained Parameterization of the Multichannel Analysis of Surface Waves Approach with Application at Yuma Proving Ground, Arizona, University of Kansas.

Schwenk, J. T., S. D. Sloan, R. D. Miller, and J. Ivanov, 2014, Correlation of the backscatter analysis of surface waves method (BASW) for anomaly detection, SEG Technical Program Expanded Abstracts 2014, 2029-2035.

Sheriff, R. E., 2002, Encyclopedic dictionary of applied geophysics: Society of exploration geophysicists Tulsa, OK.

Sherman, C., J. Rector, D. Dreger, and S. Glaser, 2014, Seismic tunnel detection at Black Diamond Mines Regional Preserve, SEG Technical Program Expanded Abstracts 2014, 2078-2082.

Sherrod, D. R., and R. M. Tosdal, 1991, Geologic setting and Tertiary structural evolution of southwestern Arizona and southeastern California: Journal of Geophysical Research: Solid Earth (1978–2012), **96**, 12407-12423.

Shustak, M., N. Wechsler, A. Yurman, and M. Reshef, 2015, Comparison of surface vs. cross-hole seismic methods for void detection in the shallow sub-surface, SEG Technical Program Expanded Abstracts 2015, 2286-2291.

Sloan, S., 2015, A current look at geophysical detection of illicit tunnels: The Leading Edge, **34**, 154-158.

Sloan, S., J. R. McKenna, S. W. Broadfoot, O. M. Metheny, R. D. Miller, S. Peterie, J. Ivanov, and L. D. Wakeley, 2011, Active seismic imaging at San Luis, Arizona, in support of tunnel detection: Army Corps of Engineers Engineer Research and Development Center Report.

Sloan, S. D., J. J. Nolan, S. W. Broadfoot, J. R. McKenna, and O. M. Metheny, 2013a, Using near-surface seismic refraction tomography and multichannel analysis of surface waves to detect shallow tunnels: A feasibility study: Journal of Applied Geophysics, **99**, 60-65.

Sloan, S. D., S. L. Peterie, J. Ivanov, R. D. Miller, and J. R. McKenna, 2010, 12. Void Detection Using Near-Surface Seismic Methods, Advances in Near-surface Seismology and Ground-penetrating Radar, 201-218.

Sloan, S. D., S. L. Peterie, R. D. Miller, J. Ivanov, J. R. McKenna, S. W. Broadfoot, and O. M. Metheny, 2012, Tunnel detection using near-surface seismic methods, SEG Technical Program Expanded Abstracts 2012, 1-5.

Sloan, S. D., S. L. Peterie, R. D. Miller, J. Ivanov, J. T. Schwenk, and J. R. McKenna, 2015, Detecting clandestine tunnels using near-surface seismic techniques: GEOPHYSICS, **80**, EN127-EN135.

Sloan, S. D., S. L. Peterie, R. D. Miller, T. L. Snow, O. M. Metheny, and J. R. McKenna, 2013b, In-theater seismic acquisition: Operational examples from a tunnel detection team, SEG Technical Program Expanded Abstracts 2013, 1801-1805.

Steeples, D.W., and R.D. Miller, 1984, High frequency shear waves for tunnel detection; *in* Proceedings of Second Technical Symposium on Tunnel Detection: Colorado School of Mines, Oct.

Steeples, D., and R. Miller, 1988, Tunnel Detection by High-relolution Seismic Methods.

Steeples, D. W., 2001, Engineering and environmental geophysics at the millennium: GEOPHYSICS, **66**, 31-35.

Stewart, J. H., 1980, Regional tilt patterns of late Cenozoic basin-range fault blocks, western United States: Geological Society of America Bulletin, **91**, 460-464.

Tanimoto, T., and K. Prindle, 2007, Surface wave analysis with beamforming: Earth, Planets, and Space, **59**, 453-458.

Tosdal, R., and D. Sherrod, 1985, Geometry of miocene extensional deformation, lower Colorado River Region, Southeastern California and Southwestern Arizona: Evidence for the presence of a regional low-angle normal fault: LPI Contributions, **575**, 147.

Walters, S. L., R. D. Miller, D. W. Steeples, J. Xia, and C. Zeng, 2009, Detecting Tunnels and Underground Facilities Using Diffracted P-Waves, Symposium on the Application of Geophysics to Engineering and Environmental Problems 2009, 937-942.

Walters, S. L., R. D. Miller, and J. Xia, 2007, Near-surface tunnel detection using diffracted P-waves: A feasibility study, SEG Technical Program Expanded Abstracts 2007, 1128-1132.

Wernicke, B., 1992, Cenozoic extensional tectonics of the US Cordillera: The Geology of North America, **3**, 553-581.

Wright, C., E. J. Walls, and D. de J. Carneiro, 2000, The seismic velocity distribution in the vicinity of a mine tunnel at Thabazimbi, South Africa: Journal of Applied Geophysics, **44**, 369-382.

Xia, J., J. E. Nyquist, Y. Xu, M. J. S. Roth, and R. D. Miller, 2007, Feasibility of detecting near-surface feature with Rayleigh-wave diffraction: Journal of Applied Geophysics, **62**, 244-253.

Xia, J., Y. Xu, R. D. Miller, and J. E. Nyquist, 2006, Rayleigh-wave diffractions due to a void in the layered half space, SEG Technical Program Expanded Abstracts 2006, 1406-1410.

Yilmaz, Ö., 2001, Seismic data analysis: Society of exploration geophysicists Tulsa.

Yu, H., B. Guo, S. Hanafy, G. T. Schuster, and F.-C. Lin, 2014, Direct detection of near-surface faults by migration of back-scattered surface waves, SEG Technical Program Expanded Abstracts 2014, 2135-2139.

Zeng, C., 2011, Wavefield Analysis of Rayleigh Waves for Near-Surface Shear-Wave Velocity.

Zeng, C., J. Xia, R. D. Miller, and G. P. Tsoflias, 2009, Modeling results on detectability of shallow tunnels using Rayleigh-wave diffraction, SEG Technical Program Expanded Abstracts 2009, 1425-1429.

Zoback, M. L., R. E. Anderson, and G. A. Thompson, 1981, Cainozoic Evolution of the State of Stress and Style of Tectonism of the Basin and Range Province of the Western United States: Philosophical Transactions of the Royal Society of London. Series A, Mathematical and Physical Sciences, **300**, 407-434.